UNIVERSITY OF CALIFORNIA, SAN DIEGO

Measuring and Mapping Biophysical Properties and Their Influence on Mesenchymal Stem Cell Fate

A dissertation submitted in partial satisfaction of the
requirements for the degree
Doctor of Philosophy

in

Bioengineering

by

Somyot Chirasatitsin

Committee in charge:

Professor Adam J. Engler, Chair
Professor Sungho Jin
Professor Ratneshwar Lal
Professor Geert W. Schmid-Schoenbein
Professor Shyni Varghese

2012

The dissertation of Somyot Chirasatitsin is approved, and it is acceptable in quality and form for publication on microfilm and electronically:

_____

_____

_____

_____

_____

Chair

University of California, San Diego
2012

DEDICATION

To my country.

EPIGRAPH

"You can differentiate to whatever you desire"

"You are what you adhere to"

"…..…
Just papers tell a few successes and a little of imagination.
Yet they never spell a lot of imperative failures and distraction.
Likewise an iceberg surrounded with the sea and the sky,
the true volume is unseen through the eyes.
…..…"

TABLE OF CONTENTS

LIST OF FIGURES

LIST OF TABLES

ACKNOWLEDGEMENTS

I gratefully thank first and foremost my doctoral adviser, Prof. Adam Engler, for giving me a chance to adhere and differentiate from a mechanical engineer to a bioengineer. His stimuli regulate some potential genes of mine to express the capabilities necessary to grow up in stem cell biology laboratory. Even though I have not been a mature bioengineer yet, many multipotent markers have been already fluoresced less or more.

I would also like to acknowledge Prof. Greet W. Schmid-Schoenbein who has revealed the mechanical points of view in tissue and cell biology, not only as one of the committee, but also as the mentor of graduate teaching assistant. A great thank to Prof. Shyni Varghese and Prof. Sungho Jin gave good advices involving polymer sciences and biomaterials. I also like to acknowledge Prof. Ratneshwar Lal who pointed out issues of the characterization using the atomic force microscopy. The great experiences from these persons will be in my deep heart and will be stated to my students about generosity and mercy of great teachers.

I wish to acknowledge Prof. Vitoon Leelamanit, Prof Andrew D. McCulloch, and Prof. Marcos Intaglietta who gave me the important opportunity to participate in the bioengineering department, UCSD. I greatly thank the full funding from the Thai Ministry of Science and Technology and the Royal Thai Government Scholarships. Also a great thank to Dr.Surapong Chatpun for managing the application to UCSD and taking care of me at the first 2 years in UCSD. Thank every officers at OEA, Royal Thai Embassy in DC for guardianship during my studying in USA.

I would like to thank my Thai friends (everyone listed in Facebook) at UCSD who always offer feeling like brothers and sisters. A special thank to my lab mates for the laughing sounds and wonderful ambient in the lab; Andrew Holle and Jennifer Young my first American friends, Justin Tse, Dayu Cheng, Gaurav Kaushik, Ludovic Vincent, Hermes Taylor, Jerry Tuler, Dr.Yu Suk Choi, Dr.Alexander Fuhrmann, Jannifer Kiang, Jessica Wen, James Kahng, Andrew lee, Kyle Kretchmer, Jacquelyn Schaefer, Gretchen Meyer, and Matt Ondeck.

Chapter 2 is published, in full, in *Soft Matter*, volume 6, issue 18, January 2010. The dissertation author is the co-primary author with Miriam V. Flores-Merino and thanks co-authors Dr. Caterina LoPresti, Dr. Giuseppe Battaglia, and Dr. Gwendolen C. Reilly. The author also would like to thank the AFM technical support from Dr. Nicholas Geisse and Jason Li (Asylum Research; Santa Barbara, CA). The authors gratefully acknowledges the financial support provided by CONACyT (to MVF-M), The University of Sheffield Excellence Exchange scheme (to MVF-M), the UK-US Foreign and Commonwealth office Stem Cell Collaboration Development Award (to GCR), the American Heart Association (#0865150F to AJE), and the Royal Thai Government Fellowship (to SC).

Chapter 3 is published, in full, is a reprint of the published article in *Journal of Physics: Condensed Matter*, volume 22, number 19, May 2010. The dissertation author is the primary author of this paper. We would like to thank Dr. Nicholas Geisse (Asylum Research; Santa Barbara, CA) for technical assistance as well as Dr. Dayu Teng for microcontact printing. The author acknowledges funding from funding from EPSRC

(EP/E03103X/1) and the Royal Thai Government Fellowship (to SC) and a grant from NIH #1DP02OD10322765 (to AJE).

In chapter 4 and 5, the manuscript has been submitted. The dissertation author is the co-primary author with Priyalakshmi Viswanathan and thanks co-authers Kamolchanok Ngamkham and Dr. Giuseppe Battaglia. The authors also thank Dr. Gwendolen Reilly (University of Sheffield) for fruitful discussions, Dr. Nicholas Geisse (Asylum Research; Santa Barbara, CA) for technical support, and Dr. Adrian Boatwright (University of Nottingham) for XPS assistance. This work was supported by grants from the National Institutes of Health (1DP02OD006460 to Dr. Adam J. Engler), Human Frontiers Science Program (RGY0064/2010 to Dr. Adam J. Engler and Dr. Guiseppe Battaglia), and the Engineering and Physical Sciences Research Council (EP/F019750/1). Pre-doctoral fellowship support was also provided by the Royal Thai Government Science and Technology (to SC).

VITA

1999	Bachelor of Engineering (Mechanical Engineering), King Mongkut's University of Technology Thonburi, Bankok, Thailand
2005	Master of Engineering (Mechanical Engineering), Prince of Songkla University, Songkhla, Thailand
2005-2008	Instructor, Prince of Songkla University, Songkhla, Thailand
2009-2010	Graduate Teaching Assistant, Department of Bioengineering, University of California, San Diego
2012	Doctor of Philosophy in Bioengineering, University of California, San Diego

PUBLICATIONS

Chirasatitsin S, Engler AJ. (2010) "Detecting cell-adhesive sites in extracellular matrix using force spectroscopy mapping" J Phys Condens Matter. May 19;22(19):194102. doi:10.1088/0953-8984/22/19/194102

Flores-Merino MV, Chirasatitsin S, Lopresti C, Reilly GC, Battaglia G, Engler AJ. (2010) "Nanoscopic mechanical anisotropy in hydrogel surfaces" Soft Matter. 1;6(18):4466-4470. DOI: 10.1039/C0SM00339E. Epub 09 Aug 2010.

LoPresti C, Massignani M, Fernyhough C, Blanazs A, Ryan AJ, Madsen J, Warren NJ, Armes SP, Lewis AL, Chirasatitsin S, Engler AJ, Battaglia G. (2011) "Controlling Polymersome Surface Topology at the Nanoscale by Membrane Confined

Polymer/Polymer Phase Separation" ACS Nano, 5 (3), pp 1775–1784 doi:10.1021/nn102455z. Epub 2011 Feb 23.

Battaglia G, LoPresti C, Massignani M, Warren NJ, Madsen J, Forster S, Vasilev C, Hobbs JK, Armes SP, Chirasatitsin S, Engler AJ. (2011) "Wet nanoscale imaging and testing of polymersomes" Small. 18;7(14):2010-5. doi: 10.1002/smll.201100511. Epub 2011 Jun 22.

Viswanathan P,Chirasatitsin S, Ngamkham K, Engler AJ, Battaglia G. "Cell instructive scaffolds through interface engineering". (*Submitted*)

ABSTRACT OF DISSERTATION

Measuring and Mapping Biophysical Properties and Their Influence on Mesenchymal Stem Cell Fate

by

Somyot Chirasatitsin

Doctor of Philosophy in Bioengineering

University of California, San Diego, 2012

Professor Adam J. Engler, Chair

Mesenchymal stem cells (MSCs) as adherent stem cells are being increasingly used as a therapeutic cell source, thus developing a better understanding of how to control MSC fate choice is an increasingly important task. Unlike the well known chemical cues, the biophysical properties of the surrounding extracellular environment, such as the appropriate spatial display of adhesion sites and environment stiffness should be clarified. The atomic force microscopy (AFM)-based technique called force spectroscopy mapping (FSM) was applied for examination biophysical properties such as elasticity and adhesion site size and spacing. Using the indentation, the spatial changes in the mechanics of poly(vinyl pyrrolidone) (PVP) and poly(acrylamide) (PAam) hydrogels were detected. PVP hydrogels had very heterogeneous elastic moduli as a function of

hydrogel position as well as the amount of crosslinker. PAam hydrogels were a much more homogeneous substrate, showing little spatial variation in moduli. Coupled with chemical-functionalized probe, the technique of chemical FSM (CFSM) was shown the capability of recognizing sub-micron adhesive sites from probe retraction studies.

By functionalizing the probe to recognize the charged surface of copolymers, the spatial display of adhesion sites in diblock copolymer foams was investiaged. Prepared by high internal phase emulsion templating using amphiphilic copolymers of polystyrene-block-polyacrylic acid and polystyrene-block-polyethylene oxide, the porous foams have been synthesized and characterized. With nanoscopic domains of cell inert and active chemistries mimicking native matrix, the nanodomains of adhesive sites were detected by CFSM. Protein adsorption on surfaces was examined in spatially macro-, micro-, and nanoscopic level. MSCs from different cell sources of human-embryonic stem-mesoderm progenitors (hES-MPs) and human bone marrow derived-mesenchymal stem cells (hBMSCs) were examined by quantitative PCR to assess their expression of myogenic, adipogenic, and osteogenic genotypes as a result of their interaction with the foams of varying composition. Interestingly, without the induction media, hBMSCs expressed adipogenic genes and proteins on ‘patchy’ matrices where adhesive nano-domains were present. More interestingly, and their expression depends on stem cell origin: marrow-derived and mesenchymal progenitor cells exhibit fundamentally different differentiation patterns, adipo- and osteogenic, respectively. Together these data for the first time implicate adhesion as a complex regulator of cell fate.

Chapter 1

Introduction

A new paradigm in therapy – Regenerative Medicine – may provide a means to treat disease by replacing damaged or injured tissues that have lost their function rather than removing them and irreparably altering or impairing function. Stem cells are a significant source for a variety of regenerative approaches to repair tissues and organs. Using naïve, immature stem cells without regard for how they may respond to the damaged niche into which they are injected can result in negative outcome as the cells adapt or "differentiate" as a result of the cues they receive from their environment. If these cues are incorrect or display abnormal properties, e.g. fibrosis stiffening the tissue, this can lead to aberrant cell differentiation, e.g. ectopic calcification in the heart [1]. From these observations, we are beginning to appreciate that the cell niche or microenvironment is very important. In past decades, information and cues involving in the microenvironment have been considered and reported such as chemical and physical cues. This chapter will review typical aspects in these stimuli.

1.1 Chemical and physical cues for stem cell differentiation

In vitro, cultured cells have been stimulated by several methods over the past several decades (Figure 1.1) but they broadly fall into soluble signaling via chemistry and physical changes in the environment. Some of these manipulations include changing nutrient content or component and adding organic or inorganic chemicals for chemical perturbations (which are most popular) and stirring or flowing media to shear cells and varying culturing materials to affect a cell's interaction with the substrate. Chemical cues can elicit and/or be the result of either intra- or extracellular signaling or both. Stem cells will sense and translate this chemical information so that genetic and phenotype changes occur. In the laboratory, researchers use differentiation cocktails to stimulate and inducing stem cells in order to differentiate them into the lineages they desire. A thorough review for mesenchymal stem cells differentiation and protocol can also be found in ref [2].

Physical cues, on the other hand, are interactions between cells and their microenvironement and can include "outside-in" signal such fluid flow and topography and "inside-out" cues including cell-cell and cell-matrix force transmission [3]. For instance, cell shape and the expression of integrin adhesion molecules on a three-dimensional cell-derived fibrillar network can be fundamentally different from typical two dimensional tissue culture plates in terms of adhesion composition, assembly, and force transmission capabilities [4]. Shear flow is a component of mesenchymal stem cell extravasation as it encourages the interaction of P-selectin-ligand with endothelial cells [5]. Both examples use physical cues in a positive manner, but these can also be used to

negatively regulate MSCs. For example, blebbistatin can pharmacologically inhibit myosin-II, which is responsible for generating forces in the cell, and inhibition can decrease the forces which are transmitted to the extracellular environment via integrin-matrix interactions. The next result is that MSCs down regulate expression of CBFα-1, an early bone differentiation marker [6].

Taken together, stem cells can sense and transduce intra- and extra cellular signals via chemical and physical mechanisms. While chemical stimuli have been well known for decades and employed routinely with stem cells, physical stimuli presented by extracellular matrix are now coming to the forefront and gaining a wider appreciation within the community of stem cell biologists. While the interplay of these cue in space and time are also influential [7-9], it is beyond the scope of this dissertation.

1.2 Extracellular matrix as an insoluble factor for stem cells

Almost all stem cells are adherent, requiring anchoring molecules bind to adhesion motifs, e.g. the Arginine-Glycine-Asparatic acid sequence (or RGD) on fibronectin. The extracellular matrix (ECM) serves as an insoluble network that provides stem cells with both chemical and physical cues for stem cell adhesion and differentiation, unlike soluble growth factors that provide paracrine and autocrine signaling to cells. ECM is able to bind to cell membrane receptors, i.e. integrins, to other ECM proteins, to growth factors – acting as a sink for them, or even to itself to form a fibrillar network. Each of these activities is indispensible for proper stem cell function. For example, ECM Young's modulus, *E*, commonly referred to in biological literature as "stiffness," is

capable of regulate stem cell fate as shown by culturing MSCs on ECM of varying elasticity, resulting in various phenotypes [6]. Without induction media, collagen-functionalized on hydrogels with elastic moduli of 1, 11, and 34 kiloPascal (kPa) offer the neurogenic, myogenic, and osteogenic expression, respectively. ECM adhesion strength has also been shown by hydrophobicity-driven conformational changes leading to differential binding of ECM proteins [10]. Coupled with osteogenic induction media, different hydrophobic hydrogels provide distinct osteogenic gene expressions. These data highlight the fact that multiple cues act in concert with each other to properly regulate stem cell fate, and often these cues may combine in ways not previously anticipated or involve completely different signaling mechanisms. For example, the release of active transforming growth factor-β from stiff ECM activates a signaling pathway for myofibroblast differentiation [11] and highlights the interplay of chemistry and elasticity in regulating cellular mechanotransduction and ultimately cell fate.

Taken together, ECM as an insoluble factor plays an important role in adherent stem cell differentiation in both aspects of chemical and physical cues (Figure 1.1). Adhesion and elasticity of ECM represent the cues and have potential to regulate stem cell fate. Studying stem cell fate controlled by ECM could reasonably employ MSC as the model for adherent stem cell differentiation.

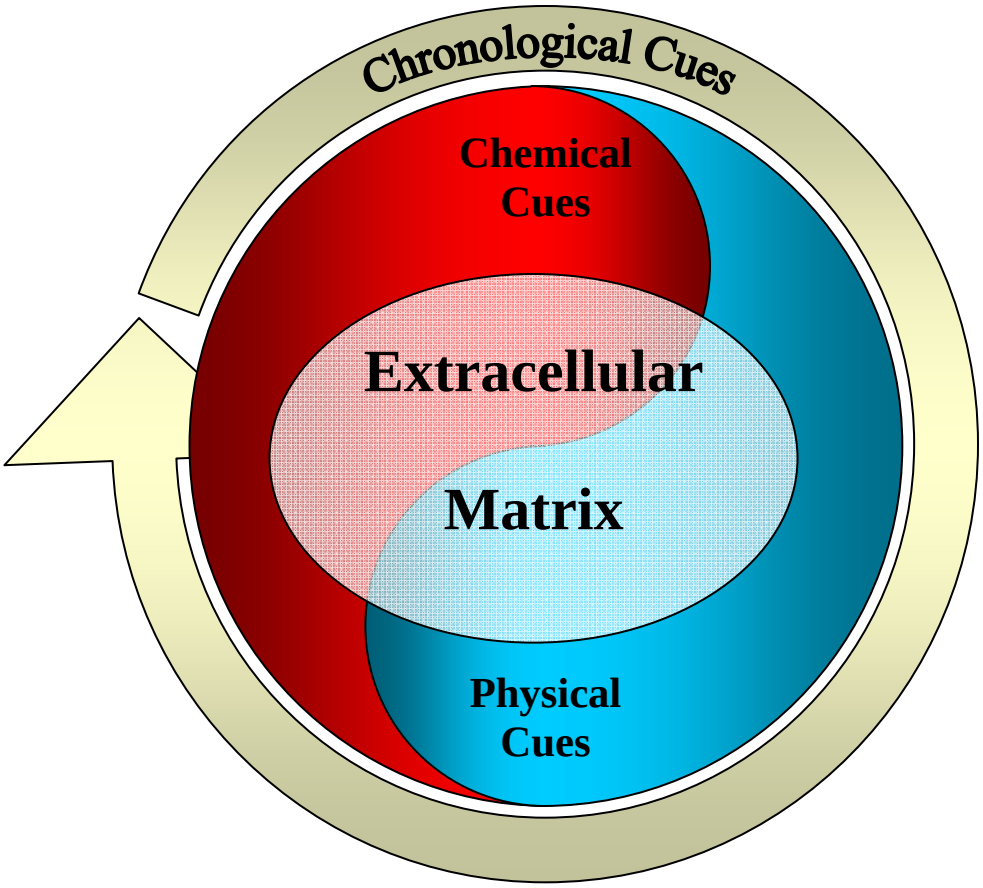

Figure 1.1: Cues for regulating stem cell fate.

1.3 Spatial Heterogeneity of Biophysical Properties

In the laboratory, a typical tissue culture substrate for adherent cells is a plasma-treated tissue culture polystyrene (TCP) plate, which provides a homogeneous set of chemical and physical properties to cells. Other biomaterials, including hydrogels such as polyacrylamide, are typically given uniform coatings of ligands or have homogenous

physical properties such as topography or stiffness to ensure, at least from a reductionist perspective, that the uniform properties of the environment will provide similar stimulation to cells. Thus any global change in cell differentiation will have resulted from a uniform extracellular property. Unlike TCP and other uniform substrates, cell-derived extracellular matrix provides discontinuous biophysical properties especially at the cellular length scale. For example, fibronectin ECM derived from fibroblasts supplies cells plated on top of the matrix with a substrate that has a fibrillar structure, discontinuous adhesion sites of RGD motifs [12], and tremendous spatial heterogeneity in biophysical properties such as adhesion and elasticity. Here I have confirmed this observation using micron-sized beads binding to cell adhesive site on fibronectin (shown in Figure 1.2) revealing discontinuous adhesive sites with the average minimum distance of 3±1 μm.

While most methods to create cell substrates make homogenous materials, there are many other methods to fabricate discontinuous biophysical properties on substrates for adherent cells [13]. For example, photolithography (PL), scanning probe lithography (SPL), and soft lithography or microcontact printing (μCP) can all create spatially patterned materials, which could present discontinuous patterns to cells. PL can be applied to microfabricated structures and substrates for biology by employing a spin-coated polymer layer that can be selectively activated and removed to create a pattern. Reverse molding from this substrate then creates flexible materials, often made out of poly(dimethylsiloxane) (PDMS), that are suitable for cell culture, protein stamping such as μCP, or other applications [14,15]. Moreover, PL can create precise features down to the nanoscale level that can be repeated for high throughput use, integrate with

electronics, and now fabricate structures in three-dimensions; however, very expensive equipment and high-quality-ambient-controlled fabrication site are needed, making it less practical. μCP can be used to mass-produce PL-created structure and is cheap and fast, but the patterns are often not a precise as the original PL master mold. SPL, which is based on the scanning tunneling microscopy (STM) and atomic force microscopy (AFM), can etch micro- and nanoscale features onto a substrate with precision and multiple surface chemistries. Features are applied only on two-dimensional substrata and fabrication is time-consuming, making this method impractical for mass production While each of these methods have clearly defined advantages from a fabrication perspective, their use as cell culture substrates ultimately must reflect in vivo behaviors in order for them to represent an improvement versus widely used alternatives including TCP.

Considered as cell responses of these heterogeneous biophysical properties, cell shape or morphology, cell adhesion and cell migration have been reported (Figure 1.3). Often for μCP, adhesion ligand area, interspacing distance, and the ligand used in stamping have altered cell morphology [16] and can affect cell spread area as well as influence cell behaviors including apoptosis [17]. Moreover enhanced cell adhesion via integrin clustering can be found for RGD nanopatterns with disordered spacing above 70 nm [18], which recapitulates in situ matrix spacing (Figure 1.2).

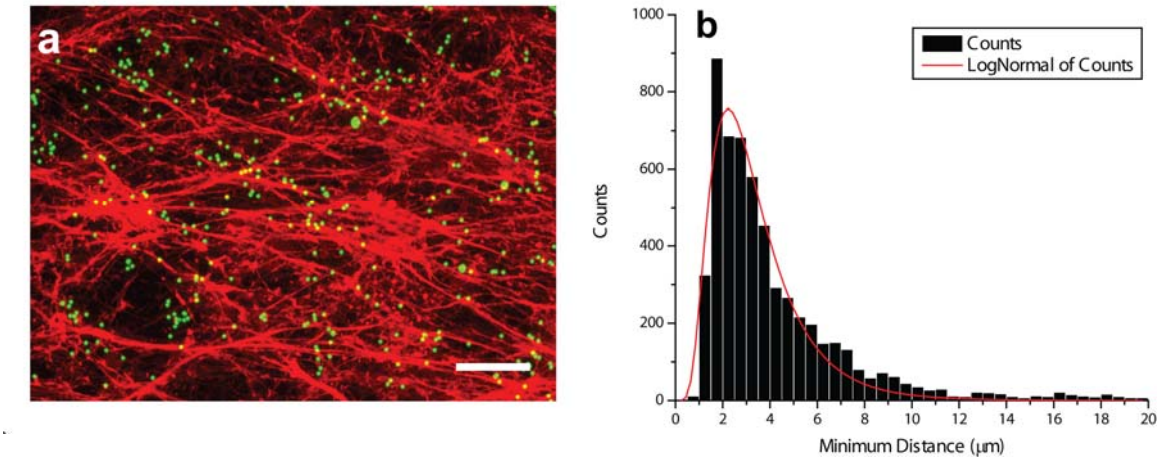

Figure 1.2: Heterogeneous adhesive sites on a three dimensional cell-derived fibrillar network. (a) Fluorescent staining on cell adhesive sites (green dot) and fibronectin fibrillar network (red), scale bar is 20μm. (b) Minimum distances of nearest neighbors of cell adhesive sites.

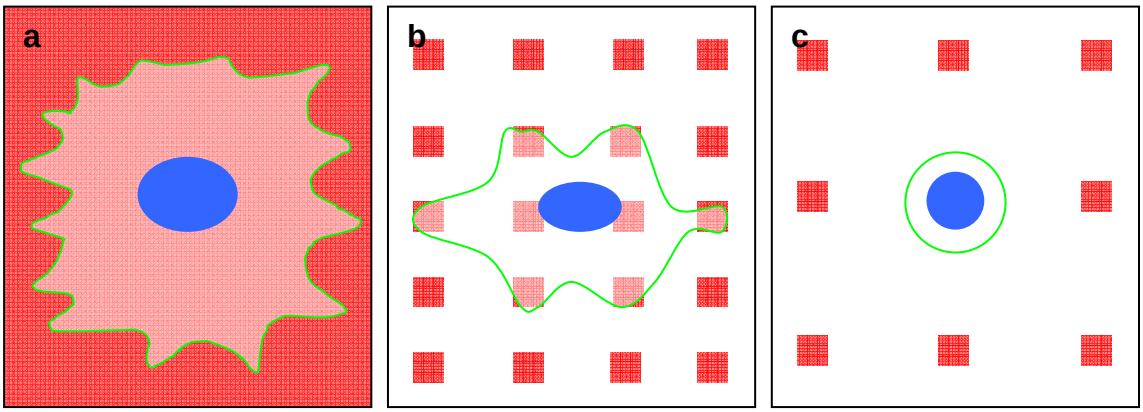

Figure 1.3: Cell spreading corresponding to adhesive site geometry of (a) Homogeneous (b) medium cellular discontinuous and (c) highly discontinuous substrate. ECM pattern in red, cell borders in green, and cell nuclei in blue.

Taken together, the spatial heterogeneity of biophysical properties such as adhesion and elasticity influence on cell responses, but none of these methods produces discontinuous properties quite like those which have been reported [12] and which I describe in Figure 1.2. Thus other fabrication methods, which are the subject of chapters 4 and 5 are needed to better mimic these parameters. Moreover, the discontinuities observed may even exceed the length scale detection limits of conventional microscopy, which I expand upon in the following section and motivate chapters 2 and 3.

1.4 The Atomic Force Microscopy-Based Technique for Spatial Biophysical property Examination

To investigate the existence of spatial heterogeneities within biomaterials, researchers often utilize convention light microscopy as electron microscopy has significant disadvantages for hydrogel cell substrates. In case of adhesion molecules printed on a substrate by μCP, protein is stained and then observed through a fluorescent microscope. While μCP may have limited resolution, SPL and other methods have limitations orders of magnitude lower and may no longer be observable by light microscopy, which is limited by wave length of the light source of ~ 100 nanometers for a typical microscope. Moreover, information from light microscopy is limited only position corresponding to the exist feature on substrate, as well as samples or substrata must be transparent. Besides positional or spatial information, mechanical information, such as elasticity, is also important. To overcome the limitation of spatial resolution as well as mechanical information, another technique should be employed.

The atomic force microscopy (AFM) is a scanning probe microscopy technique in that it uses a probe in contact with the substrate to create an image. The radius of curvature of the tip of the AFM probe is in range of nanometers to tens of nanometers, so is the resolution is sufficiently higher than light microscopes. For AFM, the probe is attached to a cantilever, enabling it to also collect information about the mechanical properties of the substrate from the interaction forces between the probe and substrate, which is calculated from probe deflection, spring constant of the cantilever, and Hooke's law. Functionalizing the probe with a chemical of interest such as an antibody enables the probe to measure the binding force between the antibody and proteins immobilized on the substrate [19,20]. To measure forces interacting with substrate, the AFM will indent the probe on the surface. Repulsive forces provide the approach force curves during indentation; meanwhile probe retraction obtains attractive forces establishing the retrace force curves. The approach force curves results in elastic moduli of substrate, whereas the retrace ones lead to the adhesive forces such as binding forces between the anti-body and protein ligands. Thus the AFM is a tool that can investigate material properties, the chemical composition of the substrate, topography from the height of probe-substrate contact, and many other parameters. Each of these properties can also be mapped across a substrate surface providing spatial information of biophysical properties of material. Taken together, AFM-based technique can improve the resolution as well as provide both chemical and physical information better than a conventional light microscope. However the potential to investigate the spatial heterogeneity of biophysical properties should be proved.

1.5 Stem Cells Response to Heterogeneous Biophysical Properties

Homogeneous biomaterials with or without chemical factors certainly stimulate stem cell differentiation [2,6,10,21], but the influence of more physiologically relevant heterogeneous substrates, especially at cellular and subcellular length scales, is unclear. While the literature in this area is relatively nascent, here I review what is known to date about how non-homogeneous substrate properties influence cell fate. A common example of an elastic but heterogeneous and continuous substrate is a hydrogel with stiffness gradients, which can regulate MSC fate by directing migration and differentiation [22]. A hydrogel gradient of 1.0±0.1 kPa/mm can stimulate MSC migration from softer to stiffer region, which can then cause cells to proliferate and differentiate to myogenic phenotype. Surfaces of self-assembled maleimide-functionalized polystyrene-block-poly(ethylene oxide) copolymers, on the other hand, are most closely able to regulate cell behavior by changing adhesion spacing [23]. However the surface chemistry was not characterized intensively, with only surface roughness being examined, and these topographic patterns were regular, resulting only in osteogenesis *in vitro* [24,25]. The spatial display of nanoscale RGD ligands affects intergrin clustering [26,27] resulting in the maturity of focal adhesion, cell spreading, and actin stress fiber formation [28]; yet the most robust differentiation again occurred on RGD nanopatterns with disordered spacing above 70 nm [18], which recapitulates in situ matrix spacing (Figure 1.2).

Taken together there are reports related to the heterogeneity of the substrate properties, they reported only in the scale higher than cellular scale, i.e. >100μm. Even

the material property can be fabricated down to cellular and nano scale, it is not for sure if that is the confounding of surface roughness or chemistry heterogeneity. Therefore the issue might be reasons of material characterization and fabrication.

1.6 Summary

The aims of this dissertation are (1) to develop the technique for detecting biophysical properties like elasticity and surface chemistry corresponding to positions in subcellular scale and (2) to investigate how the spatial heterogeneity of biophysical properties within a scaffold can influence mesenchymal stem cell fate. Chapter 2 describes the application of AFM on investigating the heterogeneity of elastic modulus on hydrogel surfaces comparing bulk and subcellular elastic moduli. Chapter 3 of this dissertation describes the development of AFM-based technique for surface chemistry. In chapter 4, surface chemistry of block copolymer materials is investigated. Chapter 5 examines mesenchymal stem cell fate on the block copolymer materials.

1.7 References

1 Breitbach, M. et al. (2007) Potential risks of bone marrow cell transplantation into infarcted hearts. *Blood* 110 (4), 1362-1369

2 Vemuri, M.C. et al. (2011) Mesenchymal stem cell assays and applications. *Methods Mol Biol* 698, 3-8

3 Holle, A.W. and Engler, A.J. (2011) More than a feeling: discovering, understanding, and influencing mechanosensing pathways. *Current Opinion in Biotechnology* 22 (5), 648-654

4 Cukierman, E. et al. (2001) Taking cell-matrix adhesions to the third dimension. *Science* 294 (5547), 1708-1712

5 Rüster, B. et al. (2006) Mesenchymal stem cells display coordinated rolling and adhesion behavior on endothelial cells. *Blood* 108 (12), 3938-3944

6 Engler, A.J. et al. (2006) Matrix elasticity directs stem cell lineage specification. *Cell* 126 (4), 677-689

7 Hole, N. et al. (1996) A limited temporal window for the derivation of multilineage repopulating hematopoietic progenitors during embryonal stem cell differentiation in vitro. *Blood* 88 (4), 1266-1276

8 Leahy, A. et al. (1999) Use of developmental marker genes to define temporal and spatial patterns of differentiation during embryoid body formation. *Journal of Experimental Zoology* 284 (1), 67-81

9 Kawai, M. et al. (2010) A circadian-regulated gene, Nocturnin, promotes adipogenesis by stimulating PPAR-Î³ nuclear translocation. *Proceedings of the National Academy of Sciences* 107 (23), 10508-10513

10 Ayala, R. et al. (2011) Engineering the cell-material interface for controlling stem cell adhesion, migration, and differentiation. *Biomaterials* 32 (15), 3700-3711

11 Wells, R.G. and Discher, D.E. (2008) Matrix elasticity, cytoskeletal tension, and TGF-beta: the insoluble and soluble meet. *Sci Signal* 1 (10), pe13

12 Reilly, G.C. and Engler, A.J. (2010) Intrinsic extracellular matrix properties regulate stem cell differentiation. *J Biomech* 43 (1), 55-62

13 Zhou, X. et al. (2011) Chemically Functionalized Surface Patterning. *Small*

14 Voldman, J. et al. (1999) Microfabrication in Biology and Medicine. *Annual Review of Biomedical Engineering* 1 (1), 401-425

15 Hahn, M.S. et al. (2006) Photolithographic patterning of polyethylene glycol hydrogels. *Biomaterials* 27 (12), 2519-2524

16 Lehnert, D. et al. (2004) Cell behaviour on micropatterned substrata: limits of extracellular matrix geometry for spreading and adhesion. *Journal of cell science* 117 (Pt 1), 41-93

17 Chen, C.S. et al. (1997) Geometric Control of Cell Life and Death. *Science* 276 (5317), 1425-1428

18 Huang, J. et al. (2009) Impact of order and disorder in RGD nanopatterns on cell adhesion. *Nano Lett* 9 (3), 1111-1116

19 Hinterdorfer, P. et al. (1996) Detection and localization of individual antibody-antigen recognition events by atomic force microscopy. *Proceedings of the National Academy of Sciences* 93 (8), 3477-3481

20 Hinterdorfer, P. and Dufrene, Y.F. (2006) Detection and localization of single molecular recognition events using atomic force microscopy. *Nat Meth* 3 (5), 347-355

21 Pittenger, M.F. et al. (1999) Multilineage potential of adult human mesenchymal stem cells. *Science* 284 (5411), 143-147

22 Tse, J.R. and Engler, A.J. (2011) Stiffness Gradients Mimicking *In Vivo* Tissue Variation Regulate Mesenchymal Stem Cell Fate. *PLoS ONE* 6 (1), e15978

23 Frith, J.E. et al. (2012) Lateral spacing of adhesion peptides influences human mesenchymal stem cell behaviour. *Journal of cell science* 125 (2), 317-327

24 Dalby, M.J. et al. (2007) The control of human mesenchymal cell differentiation using nanoscale symmetry and disorder. *Nat Mater* 6 (12), 997-1003

25 Biggs, M.J.P. et al. (2009) Interactions with nanoscale topography: Adhesion quantification and signal transduction in cells of osteogenic and multipotent lineage. *Journal of Biomedical Materials Research Part A* 91A (1), 195-208

26 Cavalcanti-Adam, E.A. et al. (2007) Cell spreading and focal adhesion dynamics are regulated by spacing of integrin ligands. *Biophys J* 92 (8), 2964-2974

27 Selhuber-Unkel, C. et al. (2010) Cell adhesion strength is controlled by intermolecular spacing of adhesion receptors. *Biophys J* 98 (4), 543-551

28 Arnold, M. et al. (2004) Activation of integrin function by nanopatterned adhesive interfaces. *Chemphyschem* 5 (3), 383-388

Chapter 2

Mechanical Force Spectroscopy Mapping:

A Technique for Detecting Elastic Domain

Abstract

The bulk mechanical properties of soft materials have been studied widely, but it is unclear to what extent macroscopic behavior is reflected in nano-mechanics. Using an atomic force microscopy (AFM) imaging method called force spectroscopy mapping (FSM), it is possible to map the nano-scopic spatial distribution of Young's modulus, i.e. "stiffness," and determine if soft or stiff polymer domains exist to correlate nano- and macro-mechanics. Two model hydrogel systems typically used in cell culture and polymerized by a free radical polymerization process, i.e. poly (vinyl pyrrolidone) (PVP) and poly (acryl amide) (PAam) hydrogels, were found to have significantly different nanomechanical behavior despite relatively similar bulk stiffness and roughness. PVP

gels contained a large number of soft and stiff nano-domains, and their size was inversely related to crosslinking density and changes in crosslinking efficiency within the hydrogel. In contrast, PAam gels displayed small nano-domains occurring at low frequency, indicating relatively uniform polymerization. Given the responsiveness of cells to changes in gel stiffness, inhomogeneities found in the PVP network indicate that careful nano-mechanical characterization of polymer substrates is necessary to appreciate complex cell behavior.

2.1 Introduction

Hydrogels are commonly defined as three-dimensional networks of hydrophilic polymers that are able to absorb and retain large amounts of water.[1-3] The mechanical behavior of hydrogels lies between viscoelastic polymer solutions and rubbers due to the presence of polymer chain entanglements and/or chemical crosslinks between the polymer chains.[4] A variety of classical methods including static elongation/ compression tests have been used to characterize the mechanical properties of hydrogels, e.g. the elastic or "Young's" modulus (E) measured in Pascal (Pa), which is the amount of deformation possible for a given force. However, such techniques only provide macroscopic information,[1] despite the fact that hydrogels can be intrinsically inhomogeneous materials with crosslinks occurring at random active sites along the polymer chains.[4-6] One such indication of inhomogeneities is that poly (acrylamide) (PAam) gels have been reported to have minor spatial fluctuations in their refractive index based on light scattering.[7] However, it is not clear if refractive index changes are

reflected in the formation of actual domains with greater or fewer crosslinks than average and what the spatial distribution of such domains would be.

To determine to what degree, if any, mechanical properties change spatially in gels, we chose to test two hydrogels commonly used in cell culture, Poly(vinyl pyrrolidone) (PVP) [8-10] and PAam [11,12] for the presence of nano-scopic spatial variations as a function of their crosslinkers, di-ethylene glycol bis-allyl carbonate (DEGBAC) and N, N´-methylene-bis-acrylamide, respectively. Since both PVP and PAam gels are commonly used in biological applications, any spatial variation in hydrogel properties could influence cell behavior.[12,13] Therefore, determining if crosslinking inhomogeneties exist is critically important in understanding complex cell behaviors.

The force-based imaging mode of Atomic Force Microscopy (AFM) called force spectroscopy mapping (FSM) has been used as a tool to study the spatial variations of mechanics for a variety of substrates.[14] Recent advances in with piezo-driven scanning stages now enable FSM at resolutions up to 2500 indentations/μm^2, which approaches the detection limit of the AFM tip, i.e. 20 nm lateral spacing from tip geometry. The improved resolution has made it possible to measure nano-scopic spatial variations within a material,[15] which bulk measurement techniques cannot detect. Despite this, here we show that bulk measurements correlate with average FSM-determined elasticity for both PVP and PAam gels, though FSM also has detected the first nano-scopic elastic inhomogeneties in PVP hydrogels.

2.2 Experimental

2.2.1 Preparation of PVP and PAam hydrogels

PVP hydrogels were obtained by solubilizing 10 g of 1-vinyl-2-pyrrolidone, di-ethylene glycol bis-allyl carbonate (DEGBAC) (Greyhound Chromatography; UK) at different concentrations (0.25, 0.5, 1.0, 1.5 and 1.75% w/v) and 2,2-azobis (2-methylpropionitrile) (Molekula; UK) in a molar ratio 1:1 with respect to DEGBAC under nitrogen. Polymerization was carried out for 24h at 50°C and the obtained hydrogels were immersed in an ethanol/water solution (70/30% v/v) in order to remove any unreacted reagents. Hydrogels were then swelled until equilibrium was reached in a 0.1 M phosphate buffer solution (PBS) (pH 7.4) and then stored at 4°C before characterization.

Preparation of PAam hydrogels was carried out as described before.[16] Briefly, Acrylamide (Aam) (3, 4 and 5% wt) and N-N´ methyl- Bis-acrylamide (1, 0.06 and 0.3% wt respectively) were mixed in PBS and degassed under vacuum for 15 minutes. 10 μL of ammonium persulfate (APS) and 1 μL of N,N,N´,N´-tetramethylethylenediamine (TEMED) for each 1mL of solution were added. Polymerization was carried out at room temperature for 5-30 minutes between aminosilane- and chlorosilane-terminated coverslips, with the hydrogel bonding to the aminosilane coverslip. PAam gel thickness was approximately 70 μm for all experiments as determined by light microscopy. All reagents purchased from Sigma-Aldrich (St. Louis, MO) unless otherwise noted.

2.2.2 Compression Test

Cylindrical samples of PVP hydrogels (10 mm diameter, 8 mm height) at equilibrium conditions 24 hrs post-polymerization were tested in an Electro Force 3200 Test Instrument (Bose, Eden Prairie; MN) equipped with parallel plates. The tests were performed using a displacement ramp at a rate of 0.1 mm/s with a load of 225 N. Young's modulus was calculated as the slope of the linear region in the stress/strain curve. All data is shown as the average of triplicate tests with the standard deviation.

2.2.3 Rheological measurements

The viscoelastic properties of PAam gels were quantified by using a RFS II fluids rheometer (Rheometrics Inc.; Piscataway, NJ). Measurements were conducted using cone and plate geometry with a sample thickness of 200 μm, which was previsouly shown to be optimal.[12] Young's modulus was calculated according to the equation $E=(1+2\nu)\,G^*$, where $\nu=0.45$ is the Poisson's ratio commonly used for hydrogels[17] and $G^*=(G' + G'')/2$. Note that G' and G" are the shear and viscous loss moduli, respectively. All data is shown at the average of triplicate tests with the standard deviation.

2.2.4 AFM, Force Spectroscopy Mapping, and Analysis

PAam hydrogels were bonded to coverslips via aminosilane chemistry and cast as 70 μm thick gels, which is sufficiently thick for small indentation analyses.[18] Large 1 mm thick PVP hydrogels were immobilized onto a glass slide using water-insoluble adhesive. Triplicate samples were placed on an Asylum MFP-3D-BIO atomic force

microscope (Asylum Research; Santa Barbara, CA) 24 hrs post-polymerization to ensure measurement of equilibrium properties (see swelling behavior of PVP hydrogels in Supplementary Figure A.1). To obtain topographic images (Supplementary Figure A.2), samples were tested in AC mode in fluid using a SiN cantilever with a spring constant of 90 pN/nm. To determine surface roughness, Igor-pro software (Wavemetrics; Portland, OR) was used for the following calculation, where y_i is the height value for each pixel and n is the total pixel count:

$$RMS = \sqrt{\left({}^{1}\!/_{v\_npo\,\mathrm{int}\,s} \sum yi^2 \right)} \qquad \text{Equation (2.1)}$$

In the identical area after topographical imaging, an array of force-indentation spectrographs with known xy-coordinates was obtained by indenting the material and observing the resulting deflection. Knowing the spring constant and assuming Hookean behavior for the SiN cantilever, data was converted to plots of force vs. indentation depth (Supplemental Figure A.3). Fitting the data with the Hertz cone model determines the Young's modulus of elasticity[19,20] for that material, where stiffer materials register higher forces for a given indentation depth. With known xy-coordinated, elasticity values could be assembled onto an FSM image. Resolution was determined by the number of points in the array, e.g. for 100 nm resolution (Figure 2.3), a 100 x 100 array over 100 μm^2 was performed. For interpoint spacing to reach 20 nm, 2500 points from a 50 x 50 array were analyzed over a scan area of 1 μm^2. Since the AFM tip has a radius of 20 nm, scans with a resolution of 20 nm represent a lower resolution limit. At 100 nm indentation spacing, tip indentations up to 250 nm into the hydrogels should produce sufficient deformation so that each indentation measures the properties of the entire 100 x

100 nm area.[19,20] The spatial information from each force-indentation curve was then used to create a map of Young's modulus, where the image colormap was scaled such that ±100% of the average modulus corresponded to maximum and minimum values. Images were thresholded using Image J software to show data 50% above (stiff) and below (soft) the sample's modulus. A domain was considered any collection of at least 4 adjacent data points with modulii that vary no more than 20%.

AFM data was further analyzed and compared with the initial polymer chemistry of each material to determine crosslinking efficiency. Rubber elasticity theory relates Young's modulus to the absolute temperature and crosslinking density via:

$$N = E / \mathrm{R}\,\mathrm{T} \qquad \text{Equation (2.2)}$$

where E is the Young's modulus, R is the gas constant, T is absolute temperature, and N is the crosslink chain density in the material (in mol/m^3).[4,5] When N is divided by the total crosslinker density present in solution pre-polymerization, it is possible to calculate crosslinking efficiency, ε_{XL}.[21]

2.3 Results and Discussion

The elastic modulus of PVP and PAam hydrogels at varying crosslinker concentration were first measured by compression or rheological tests, respectively (Figure 2.1A). Note that to obtain elastic moduli from rheological measurements as shown in Figure 2.1A, data was first converted from shear moduli.[17] These conventional measurements that observe bulk properties can easily be compared to force-

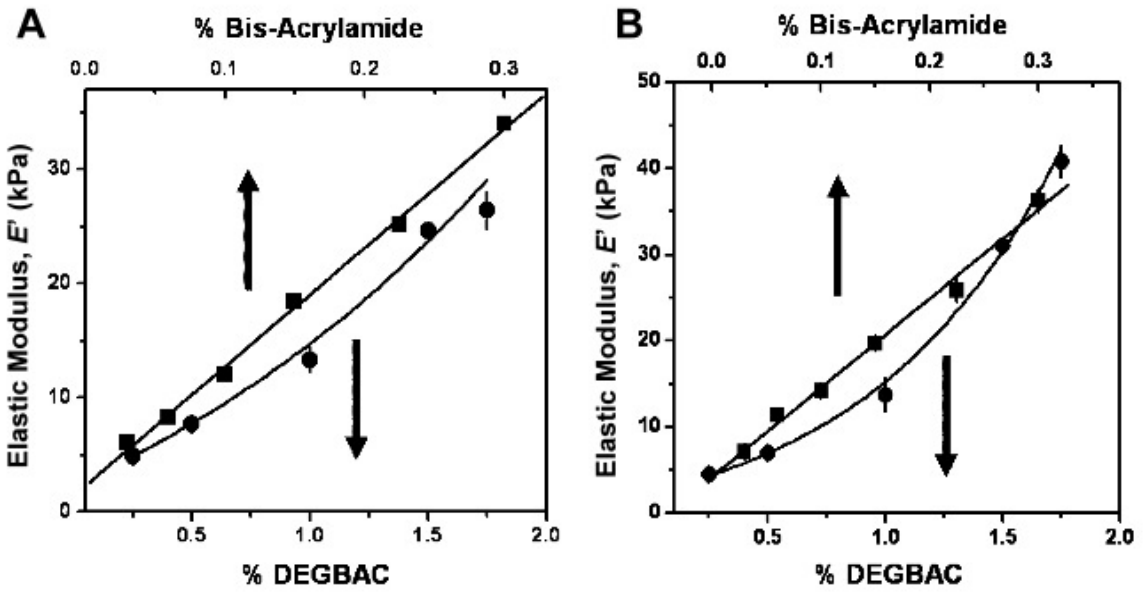

Figure 2.1: Elastic Modulus of A) PVP hydrogels by compression test (dots) PA hydrogels by rheology (squares) and B) PVP hydrogels (dots) by AFM and PA hydrogels (squares) by AFM as a function of the crosslinker percentage.

indentation spectrograms obtained from hundreds of localized AFM indentation experiments,, which are fit using a Hertz model to obtain elastic moduli (Figure 2.1B).[13,16,20] In particular, elastic moduli for PVP hydrogels measured by AFM range from 4.5 ± 0.5 kPa, corresponding to the lowest crosslinking density (0.25% DEGBAC), to 40.8 ± 1.9 kPa for the highest crosslinking density (1.75% DEGBAC; Figure 2.1B) and are comparable to with the results obtained by compression tests (Figure 2.1A; correlation coefficient = 0.986). Similar results are shown with PAam hydrogels whose elastic moduli range from approximately 2.8 ± 0.3 kPa to 34.8 ± 1.5 kPa, as determined by AFM (Figure 2.1B), which are comparable to rheological values (Figure 2.1A) as has been previously noted (correlation coefficient = 0.996).[13]

Unlike traditional methods, AFM can indent materials with nanometer precision, and by coupling a piezo-driven XY stage with AFM, hydrogels can be translated in X and Y such that force-indentation spectrograms can be determined at regular intervals. Our current version of FSM can collect data at high spatial resolution not previously possible, i.e. 2500 indentations/μm^2 or 20 nm lateral spacing. Given that AFM tip approaches 20 nm, this is the resolution limit.[15] Figure 2.2 show the results of the force-indentation scans of PVP hydrogel surfaces at this resolution limit to detect nano-scopic domains. Figure 2.2A shows scans of PVP hydrogels with initial crosslink densities close to the minimum and maximum tested. Note the gray scale scheme (far right) indicates differences in the elastic modulus in relation to the mean value of each image. Despite the fact that the average elastic modulus of the two materials is very similar to their bulk measurements, PVP hydrogels show the presence of soft and stiff domains. Figure 2.2B illustrates how soft and stiff domains of different elastic moduli were selected. Though there was no change in the prevalence of nano-domains between any of the PVP hydrogel samples (~4 nano-domains/μm^2), there was a 10-fold difference in nano-domain size with a substantial size increase below 1% crosslinker (Figure 2.2C). It is important to note that domain size differences did not depend on whether the domain was soft or stiff. However, the presence of nano-domains did not dramatically influence hydrogel surface roughness (Equation 2.1 and Figure 2.2C; gray data), which was not significantly different across hydrogel samples, despite differences in swelling (Supplemental Figure A.2).

Given that there is a swelling change but lack of topographical change associated with the presence of nano-domains, we attempted to clarify the differences encountered

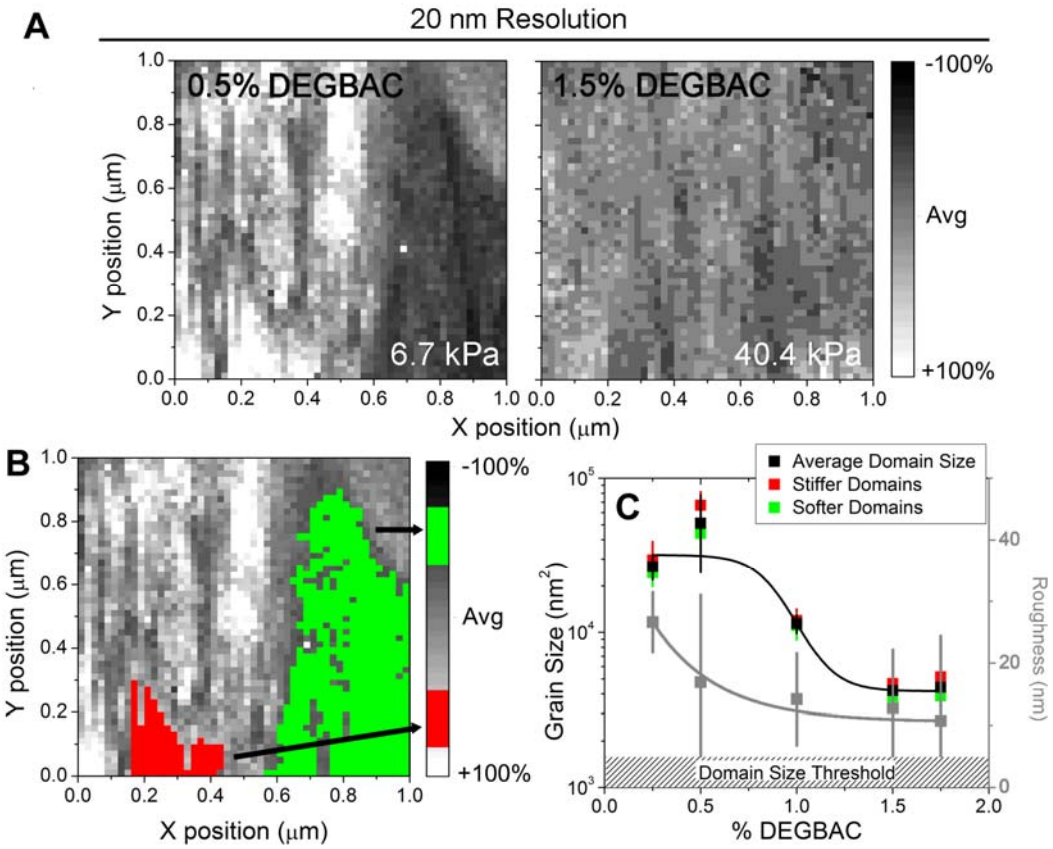

Figure 2.2: Force Spectroscopy Mapping of hydrogel surfaces of PVP at 20 nm lateral resolution. Color map ranges from low (black) to average (gray) to high (white) modulus and is shown as a percentage change from the average. B) Illustration of the domain size measurement where stiff (red) and soft (green) domains are highlighted. C) Average nano-domain size of PVP hydrogels as a function of DEGBAC crosslinking is shown in black. Data was divided into stiffer and softer domains and replotted in red and green, respectively. The hatched region indicates the domain size threshold, where a minimum of 4 adjacent points of the same value were required to be called a domain. *p <0.05

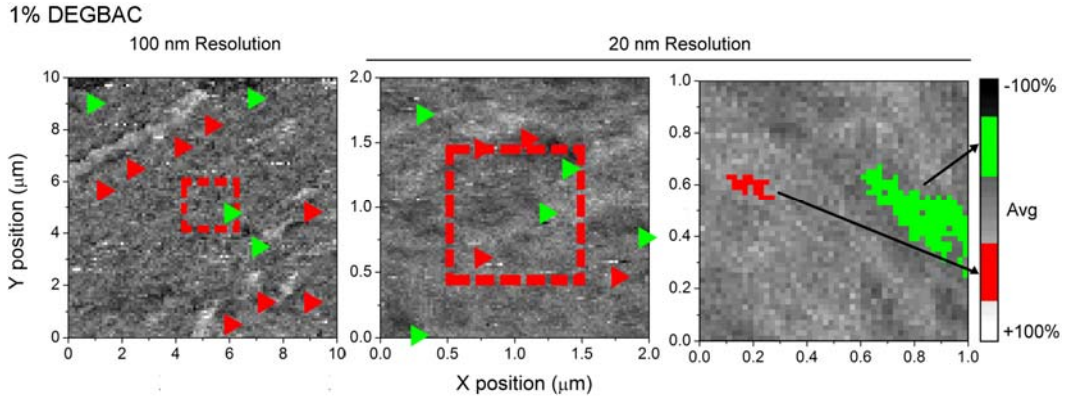

Figure 2.3: Force Spectroscopy Mapping of a 1% DEGBAC/PVP gel where successive scans zoomed in from 100 nm resolution over a 10 x 10 μm^2 scan (left) to 2 x 2 (center) and 1 x 1 μm^2 scans (right) at 20 nm resolution. Red dashed boxes indicate where from the previous scan the subsequent scanned area is. Red and green arrowheads indicate stiff and soft domains, respectively; in the 10 x 10 and 2 x 2 μm^2 scans. For 1 x 1 μm^2 scan, representative soft and stiff nano-domains are indicated. Note that nano-domains present in the 2 x 2 μm^2 scan cannot be easily resolved in the micro-domains in the 10 x 10 μm^2 scan at 5-fold lower resolution (15-fold versus Figure 2.2).

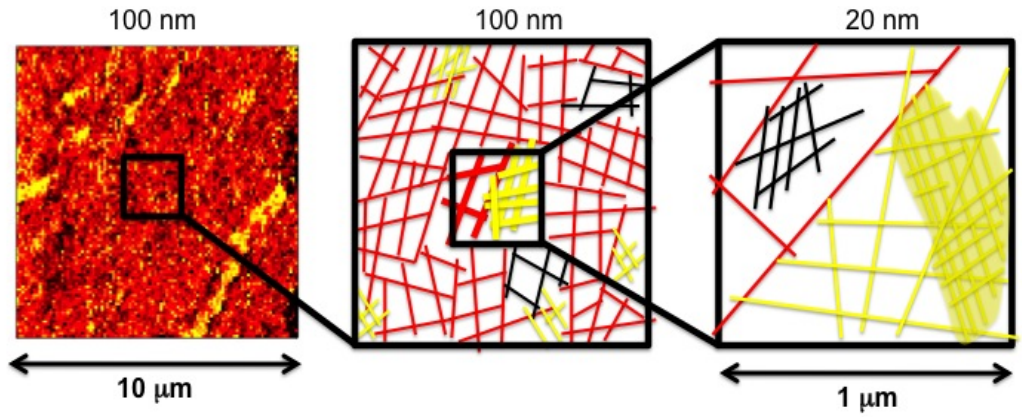

Figure 2.4: Schematic of the mechanism of domains in PVP hydrogels. In left a scan of 10x10 of 1% DEGBAC / PVP, in center the polymer network, with domains of different density which are represented by color, and left schematic of 1% PVP at a higher resolution where sub-domains are easily resolved.

in domain sizes via additional scans at two resolutions of same surface area. Using a 1% crosslinked PVP hydrogel, which is the transition point for domain size and swelling, sequential FSMs of the PVP hydrogel where made (Figure 2.3), continuously zooming in from 100 nm resolution over 100 μm^2 scan (left) to 20 nm scans over 4 μm^2 (center) and 1 μm^2 scans (right). While possible to observe at 100 nm resolution, nano-domains were more difficult to detect and did not occur at the same frequency as with higher resolution scans (1-2 domains/μm^2). Thus spatial changes in the pre-polymerized solution likely exist below the 100 nm length scale and can possibly be explained by differential chemistry at these length scales: below 1% crosslinker, crosslinker efficiency, ε_{XL}, is much more variable than it is above 1% DEGBAC (Supplemental Figure A.4a); a greater difference in efficiency may be the result of poor nano-scopic mixing at lower DEGBAC concentrations that is not present at higher concentrations and hence nano-domain formation (Figure 2.4).

On the other hand, the spatial distribution of modulus in the PAam hydrogel surface was found to be homogeneous compared with low crosslinker PVP hydrogels surfaces. Specifically, PAam hydrogels had a much lower incidence of domain formation (1-2 nano-domains/μm^2), and regardless of composition and modulus, domain size was small and did not change (Figure 2.5) as with PVP hydrogels (Figure 2.2C). No change was also found among the size of the stiff and soft domains in all the PAam hydrogels (not shown). With the absence of nano-domains (Figure 2.5C) within the PAam hydrogels, one may argue that differences in crosslinking time and additional mixing of different phases could induce such a difference.[22] In fact, PAam polymerization here occurred within 30 minutes at room temperature while PVP hydrogels required 24 hours

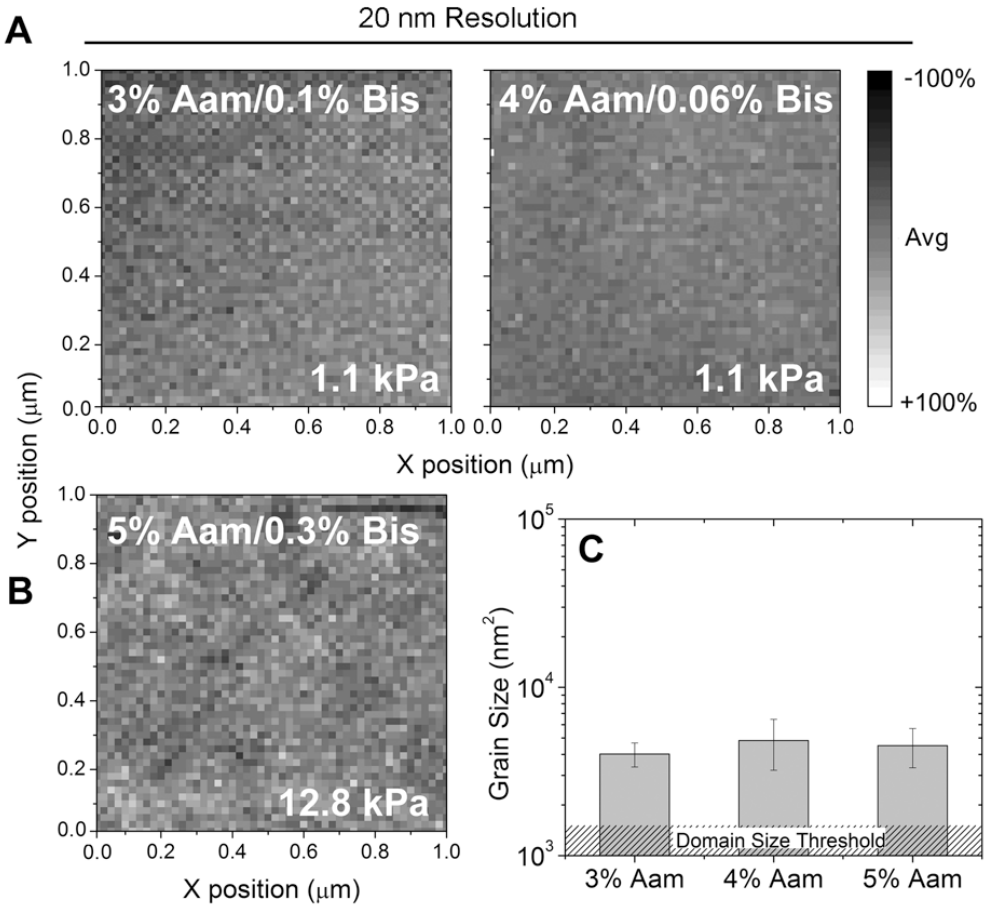

Figure 2.5: Force Spectroscopy Mapping of hydrogel surfaces of PAam at 20 nm lateral resolution. A) Indicated Aam/Bis ratios were used to achieve the same average modulus despite different bulk polymer concentrations without the formation of significantly sized nano-domains. B) Force spectroscopy map of stiffer PAam gel also does not show large nano-domains. C) Average nano-domain size of PAam hydrogels. The hatched region indicates the domain size threshold, where a minimum of 4 adjacent points of the same value were required to be called a domain.

and 50^{o}C to solidify. PAam elasticity is known to be temperature-dependent,[7,23] suggesting temperature-dependent domain formation could be possible but not observed in PA hydrogels given the polymerization temperature used here. On the other hand, PVP hydrogels could contain nano-domains due to a low initiation rate,[24] where nucleating clusters are not evenly distributed due to the energy required. Since this is known to scale with crosslinker concentration, the sharp transition observed around 1% DEGBAC may be explained by an activation energy change within the PVP hydrogel. PAam hydrogels, which have a different activation,[25] are not likely to be subject to such a trend as they do not form nano-domains in the first place.

A more likely explanation for the difference between PVP and PAam systems is in the existence of separate "nucleation and growth steps" or phase separation[26] previously observed for hydrogels after the introduction of an interpenetrating polymer.[27] These processes would result in hydrogels that swell differently but which have a relatively smooth surface given the overall domain size. Formation of network chain by free radical polimerization, such as in the case of PVP, have been reported to take place in short periods of time compared to the long relaxion time of network chains, for this reason free radical polimerization reactions results in domain formation and inhomogeneities during the long relaxion times. Such a process is not likely in PAam hydrogels as their crosslinking efficieny, ε_{XL}, is known to scale with crosslink density [21] and in this study ranged from being as efficient to being 3-fold more efficient than PVP hydrogels (Supplemental Figure A.4b). Though the exact mechanism(s) of inhomogeneities in PVP hydrogels is unclear and warrants further study, nanoscale

domains pose an interesting system to explore biological questions involving nanoscale changes in stiffness.

2.5 Conclusion

Hydrogels are intrinsically heterogeneous, and depending on the crosslinking method, control over regions with higher or lower crosslinking density can be achieved.[28-30] However, the presence of these stiffer or softer regions has largely been inferred from indirect measurements, e.g. the diffusion of water, different molecular weight molecules, or light scattering through the hydrogel.[6,7] Since the crosslinking density is directly related to hydrogel mechanical properties, the FSM method here permits direct characterization of the crosslinking density distribution in hydrogels, and our results from these direct measurements do not necessarily align with the previous indirect measurements. Nonetheless, the heterogenous nature of hydrogels has important consequences for the optimization of materials, especially for applications where uniform surface properties are desired, e.g. cell culture [11]. FSM could also permit detailed chemical analysis of the surface if the AFM probe is chemically functionalized, e.g. mapping of the interaction between positively charged polymer such as poly-l-lysine interacting with negatively charged DNA[31] or mapping out adhesive sites within a matrix.

The combination of mechanical and chemical characterization make FSM an ideal imaging mode to measure abrupt changes in the nano-scale spatial distribution of elasticity,[19] which presently can only be reflected in the variability of bulk mechanical

properties, e.g. the error in Figure 2.1, or inferred by indirect measurements. Moreover, these techniques are not likely to be sensitive enough to detect such small crosslink changes occurring with limited spatial variation. Whilst the presence of these inhomogeneities can be an obstacle for the design of controlled release devices, if patterned correctly, it can be a great advantage for emerging applications in tissue engineering, where nano-patterned changes in microenvironmental properties, such as stiffness, could be advantageous for the differentiation of stem cells.[11]

2.6 Acknowledgements

This chapter is published, in full, in *Soft Matter*, volume 6, issue 18, January 2010. The dissertation author is the co-primary author with Miriam V. Flores-Merino and thanks co-authors Dr. Caterina LoPresti, Dr. Giuseppe Battaglia, and Dr. Gwendolen C. Reilly. The author also would like to thank the AFM technical support from Dr. Nicholas Geisse and Jason Li (Asylum Research; Santa Barbara, CA). The author gratefully acknowledges the financial support provided by CONACyT (to MVF-M), The University of Sheffield Excellence Exchange scheme (to MVF-M), the UK-US Foreign and Commonwealth office Stem Cell Collaboration Development Award (to GCR), the American Heart Association (#0865150F to AJE), and the Royal Thai Government Fellowship (to SC).

2.7 References

1 Anseth, K.S. et al. (1996) Mechanical properties of hydrogels and their experimental determination. *Biomaterials,* 17 (17), 1647-1657

2 Zimberlin, J.A. et al. (2007) *Soft Matter* 3, 763-767

3 Hoffman, A.S. (2002) Hydrogels for biomedical applications. *Advanced Drug Delivery Reviews* 54 (1), 3-12

4 Landu, L.D. and Liftshiz, E.M. (1986) *Theory of Elasticity*, Butterworth-Heinemann

5 Flory, P.J. (1953) *Principles of Polymer Chemistry*, Cornell University Press.

6 Zhang, X. et al. (1999) In Situ Monitoring of Hydrogel Polymerization Using Speckle Interferometry. *Journal of Physical Chemistry B* 103, 2888-2891

7 Liu, R. and Oppermann, W. (2006) Spatial Inhomogeneities of Polystrene Gels Prepared from Semidilute Solutions. *Macromolecules.* 12, 4159-4167

8 Smith, L.E. et al. (2008) *A.C.S. Symposium Series* 977, 196-203

9 Vijayasekaran, S. et al. (1996) *Journal of Biomaterials Science, Polymer Ed.* 8, 685-696

10 Liu, Z. and Rimmer, S. (2002) *Journal of Controlloed Release* 81, 91-99

11 Engler, A.J. et al. (2006) *Cell* 126, 677-689

12 Yeung, T. et al. (2005) Effects of substrate stiffness on cell morphology, cytoskeletal structure, and adhesion. *Cell Motility and the Cytoskeleton* 60, 24-34

13 Engler, A.J. et al. (2004) *Biophys. J.* 86, 617 - 628

14 Frisbie, C.D. et al. (1994) Functional Group Imaging by Chemical Force Microscopy. *Science* 265 (5181), 2071-2074

15 Chirasatitsin, S. and Engler, A.J. (2009) *J. Phys.: Condens. Matter.* 21

16 Engler, A.J. et al. (2007) In *Methods in Cell Biology: Cell Mechanics* (Vol. 83), pp. 521-545, Academic Press

17 Li, Y. et al. (1993) *J. Appl. Polym. Sci.* 50, 1107-1111

18 Engler, A.J. et al. (2004) Surface probe measurements of the elasticity of sectioned tissue, thin gels and polyelectrolyte multilayer films: Correlations between substrate stiffness and cell adhesion. *Surface Science* 570 (1-2), 142-154

19 Radmacher, M. et al. (1995) Imaging soft samples with the atomic force microscope: gelatin in water and propanol. *Biophys. J.* 69 (1), 264-270

20 Dimitriadis, E.K. et al. (2002) *Biophys. J.* 82, 2798 - 2810

21 Orakdogen, N. and Okay, O. (2006) Correlation between crosslinking efficiency and spatial inhomogeneity in poly(acrylamide) hydrogels. *Polymer Bulletin* 57 (5), 631-641

22 Tse, J.R. and Engler, A.J. Preparation of Hydrogel Substrates with Tunable Mechanical Properties. *Current Protocol Cell Biology* in Press

23 Calvet, D. et al. (2004) *Macromolecules* 37, 7762–7771

24 Matsumoto, A. (1995) *Adv. Polym. Sci.,* 41

25 Muniz, E.C. and Geuskens, G. (2000) *J. Membr. Sci.* 172, 287-293

26 Boots, H.M.J. et al. (1996) *Macromolecules* 29, 7683–7689

27 Kwoka, A.Y. et al. (2003) *Polymer* 44, 7335-7344

28 Tae, G. et al. (2005) *Biomaterials* 26, 5259-5266

29 Séréro, Y. et al. (1998) *Phys. Rev. Lett.* 81, 5584-5587

30 Ryan, A.J. et al. (2005) *Faraday Discuss.* 128, 55-74

31 Liu, G. et al. (2001) *J. Biol. Chem.* 276, 34379-34387

Chapter 3

Detecting Cell-Adhesive Sites in Extracellular Matrix using Force Spectroscopy Mapping

Abstract

The cell microenvironment is composed of extracellular matrix (ECM), which contains specific binding sites that allow the cell to adhere to its surroundings. Cells employ focal adhesion proteins, which must be able to resist a variety of forces to bind to ECM. Current techniques to detect the spatial arrangement of these adhesions, however, have limited resolution and those that detect adhesive forces lack sufficient spatial characterization or resolution. Using a unique application of force spectroscopy, we demonstrate here the ability to determine local changes in the adhesive property of a fibronectin substrate down to the resolution of the fibronectin antibody-functionalized tip

diameter, ~ 20 nm. To verify the detection capabilities of force spectroscopy mapping (FSM), changes in loading rate and temperature were used to alter bond dynamics and change adhesion force. Microcontact printing was also used to pattern FITC-conjugated fibronectin in order to mimic the discontinuous adhesion domains of native ECM. Fluorescent detection was used to identify the pattern while FSM was used to map cell adhesion sites in register with the initial fluorescent image. The results show that FSM can detect the adhesion domains at high resolution and may subsequently be applied to native ECM with randomly distributed cell adhesion sites.

3.1 Introduction

Adhesion to the surrounding environment is an important cell behavior that regulates a variety of processes, e.g. motility [1,2], matrix remodeling [3,4], cancer metastasis [5,6] and even signaling and gene expression [7,8]. As the cell starts to attach to its environment, which is composed of a large fibrillar network of proteins known as the extracellular matrix (ECM), it does so by forming clusters of proteins that bind to ECM known as focal adhesions; these adhesions connect the cell's cytoskeleton to ECM and enable the cell to contract against it. Yet given its fibrillar nature and localization in tissues, the distribution of ECM in vivo is not uniform [9]. Moreover, ECM proteins contain only a few small adhesive sites and cell binding can occur only at these sites, e.g. the R-G-D peptide sequence on the 10^{th} type 3 domain of fibronectin binds to $\alpha_5\beta_1$ integrins in focal adhesions [10]. With such specificity and a limited number of adhesion sites with an ECM, characterization of receptor-ligand interactions and their distribution

in a natural or synthetic material must be equally specific so that accurate control of cell behavior is possible. Moreover, these interactions are mechanical in nature as they link force-generating proteins, e.g. myosin, to ECM. Adhesion mechanics are especially important given that force-dependent integrin behavior regulates the activity of many proteins, e.g. Rho GTPases, resulting in changes in cell behavior and phenotype [11]; thus measurement methods that determine the force that cell adhesions can withstand would provide an additional mode to evaluate cell adhesion.

Many techniques have been used to investigate the mechanical properties of receptor-ligand interactions, both population- [12] and single cell-based [13], and have been performed using native [12] and synthetic environments [14]. Spinning disc assays, as population-based measures, apply a uniform or radially-dependent shear profile that can examine the detachment force of a group of cells, and they has been used to demonstrate the importance of matrix dimensionality [12], focal adhesion clustering [15], and adhesive domain conformation [16]. On the other hand, single-cell techniques such as micropipette aspiration [13,14], force spectroscopy [17,18], and optical tweezers [19] are very sensitive and can measure the tens of pico-Newtons required to rupture single integrin-ECM bonds [19,20]. For force spectroscopy, a probe is functionalized with receptors or oppositely charged macromolecules [21], making it stick to ligands immobilized on a substrate. As the probe translates up from the substrate, the bond tenses until it ruptures, and this force is then determined from plots of probe force versus position relative to the substrate's surface [22]. While accurately measuring forces, none of these techniques provide information on adhesion distribution on the cell or within the ECM. Fluorescent microscopy, on the other hand, can be used to better appreciate

adhesion distribution, yet this technique can neither provide similar mechanical information nor can it easily resolve structures smaller than hundreds of nm without complex image filtering, such as point-spread functions. As has been previously well-documented, the distribution and size of these adhesive sites is much smaller than this resolution limit [9,23], so their detection will require a combination of these techniques.

To detect and determine the localization of potential submicron-sized adhesive regions, here we propose exploiting the high lateral resolution of a piezo-controlled microscope stage with force spectroscopy for a technique we have termed force spectroscopy mapping (FSM). This technique combines both force sensitivity and high lateral resolution to create "maps" of surfaces that indicate how adhesion forces change as a function of position. Using an atomic force microscope (AFM) tip, our technique is only limited in lateral resolution by the diameter of our tip, which is typically 20 nm, and in force resolution by thermal oscillations of the tip. Moreover, coupling this technique with an AFM-mounted fluorescent microscope enables dual fluorescence and FSM imaging, which makes it possible to align features that are large enough to be detectable using both imaging techniques, e.g. micron-sized features made via microcontact printing.

3.2 Methods

All materials were obtained from Sigma (St. Louis, MO), unless otherwise noted. All values are shown as average ± standard deviation unless otherwise noted.

3.2.1 Preparation of Polyacrylamide Gels

Polyacrylamide (PA) solution was prepared using the mixture of 0.1% w/v bis-acrylamide crosslinker and 10% w/v of acrylamide monomer (C_3H_5NO) providing the elasticity of ~11kPa [24]. To initiate the polymerization, 1/100 volume of 10% ammonium persulfate and 1/1000 volume of N,N,N',N'-tetramethylethylenediamine were added to the PA solution. 25μL of the solution was dropped on a chlorosilanized coverslip to ensure easy detachment and a flat and uniform gel surface once polymerized. A glutaraldehyde-treated aminosilanized coverslip 25mm in diameter was placed on the top. When polymerized, PA hydrogel covalently bound to the top circular coverslip. The hydrogel-coated coverslips were placed in a 6-well plate filled with dH_2O and kept in 4^oC until immobilizing protein of interest.

3.2.2 Microcontact Printing (μCP)

To immobilize protein on the PA gel, a microcontact printing technique was applied as modified from Tien and Chen [25]. Briefly, a polydimethylsiloxane (PDMS) stamp was created from silicon wafer master containing 500 nm silicon dioxide features, i.e. 5 x 5 μm rectangles, which was fabricated using standard photolithographic techniques (Innovative Solutions; Sofia, Bulgaria). To make the master less adhesive, it was treated with a vapor of (tridecafluoro-1,1,2,2-tetrahydrooctyl)-1-trichlorosilane (United Chemical Technologies, Bristol, PA) for 60 min. Stamps of PDMS were then made by curing Sylgard 184 (Dow-Corning) for ~1 h against the silanized silicon master. 100 μL of a 9:1 mixture of 100μg/mL rat plasma fibronectin and 100μg/mL FITC-

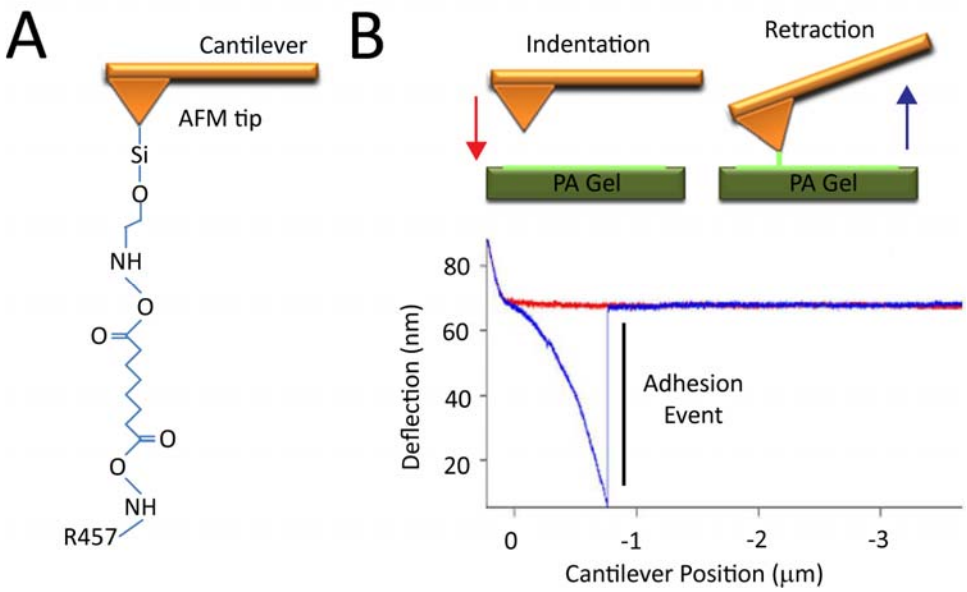

Figure 3.1: (A) Tip functionalization schematic depicting the attachment of the R457 antibody using the BS3 crosslinker. (B) Spectrograph (bottom) of a typical adhesion force curve containing a binding event between the antibody and fibronectin, which has been labeled as an "Adhesion Event." This is the result from tip indentation into the material (top; red arrow), bond formation between the functionalized tip and substrate (green tether), and bond rupture upon tip retraction (top; blue arrow).

conjugated fibronectin was incubated for 30 minutes at room temperature on the PDMS stamp surface.

Before μCP, the PA gel was treated with sulfosuccinimidyl-6-(40-azido-20-nitrophenylamino) hexanoate (sulfo-SANPAH; Pierce, Rockford, IL) to act as a crosslinker between the gel and fibronectin. The phenylazide group of sulfo-SANPAH covalently binds to polyacrylamide on photoactivation at 365 nm, leaving the sulfosuccinimidyl group to react with primary amines of fibronectin. Sulfo-SANPAH-treated PA gel was dehydrated at 60^{o}C for 30 minutes, while the stamp was incubated by

the fibronectin solution. Excess fibronectin solution was removed from the stamp, which was then inverted and placed onto the dehydrated gel. Pressure was kept on the stamp for 90 seconds using tweezers before being gently peeled off. The patterned gel was then rehydrated overnight. Pattern features are shown in Figure 3.5B with a grid of 5 × 5 μm rectangles spaced 5 μm apart. The dimension and the orientation of the pattern were examined by the fluorescent microscope before force mapping.

3.2.3 AFM Cantilever Functionalization

Gold-coated, pyramid-shape tips SiN cantilevers (TR400PB; Olympus; Center Valley, PA) were functionalized (Figure 3.1A) with the antibody R457, rabbit polyclonal anti-rat antiserum against the amino-terminal 70-kDa fragment of fibronectin [26], using a previously establish method [27]. Briefly, the cantilevers were cleaned by chloroform and incubated with ethanolamine-HCL in dimethylsulfoxide overnight, resulting in amine group functionalization on the cantilever tips. After rinsing with Phosphate-buffered saline (PBS), tips were incubated in 25 mM BS3 (bis[sulfosuccinimidyl] suberate; Pierce) for 30 min. After rinsing again, tips were then incubated in 100μg/mL R457 for 30 min to crosslink the antibody and tip. Functionalized cantilevers were kept in the 4^{o}C until use.

3.2.4 Force Spectroscopy Mapping

PA gel samples were placed on an MFP-3D-BIO atomic force microscope (AFM; Asylum Research; Santa Barbara, CA) with a BioHeater Closed Fluid Cell. Using custom software written in Igor Pro (Wavemetrics; Portland, OR), samples were placed in PBS and indented in a regular array of points with a resolution of 400 data points per μm^2

using a SiN cantilever with a spring constant k_{sp} = 20 pN/nm, a scan area of 100 - 400 μm^2 as indicated, and an indentation velocity of 5 μm/s unless otherwise noted (~ 100 nN/s). Indentation into the gel was set not to exceed 10 nm in all cases. To promote binding of the antibody-coated cantilever and the fibronectin-coated substrate, a dwell time of 3 seconds was added between tip indentation (Figure 3.1B; red) and retraction cycles (Figure 3.1B; blue). By knowing the resulting deflection and cantilever spring constant and assuming Hookean behavior for the cantilever, deflection versus cantilever position data could be converted into force-indentation spectrographs [28]. Data was then analyzed to determine the maximum adhesive force, i.e. the greatest difference between the retraction curve and baseline. Using each force measurement's x- and y-position, data was then plotted on a map of the surface and interpolated to generate a force spectroscopy map. The maps shown in Figure 3.2, 3.4, and 3.6 are the average of at least 5 maps of the identical surface.

3.3 Results

3.3.1 Mapping Adhesion Forces using Force Spectroscopy

An atomic force microscope (AFM) tip, functionalized as indicated in Figure 3.1A, was indented into a compliant polyacrylamide (PA) hydrogel to allow the amino-terminal 70-kDa fragment of fibronectin to bind to the R457 antibody [26]. As shown in the force spectrogram in Figure 3.1B, upon retraction of the tip from the hydrogel surface, a large adhesive force was observed, which was created by the deflection of the

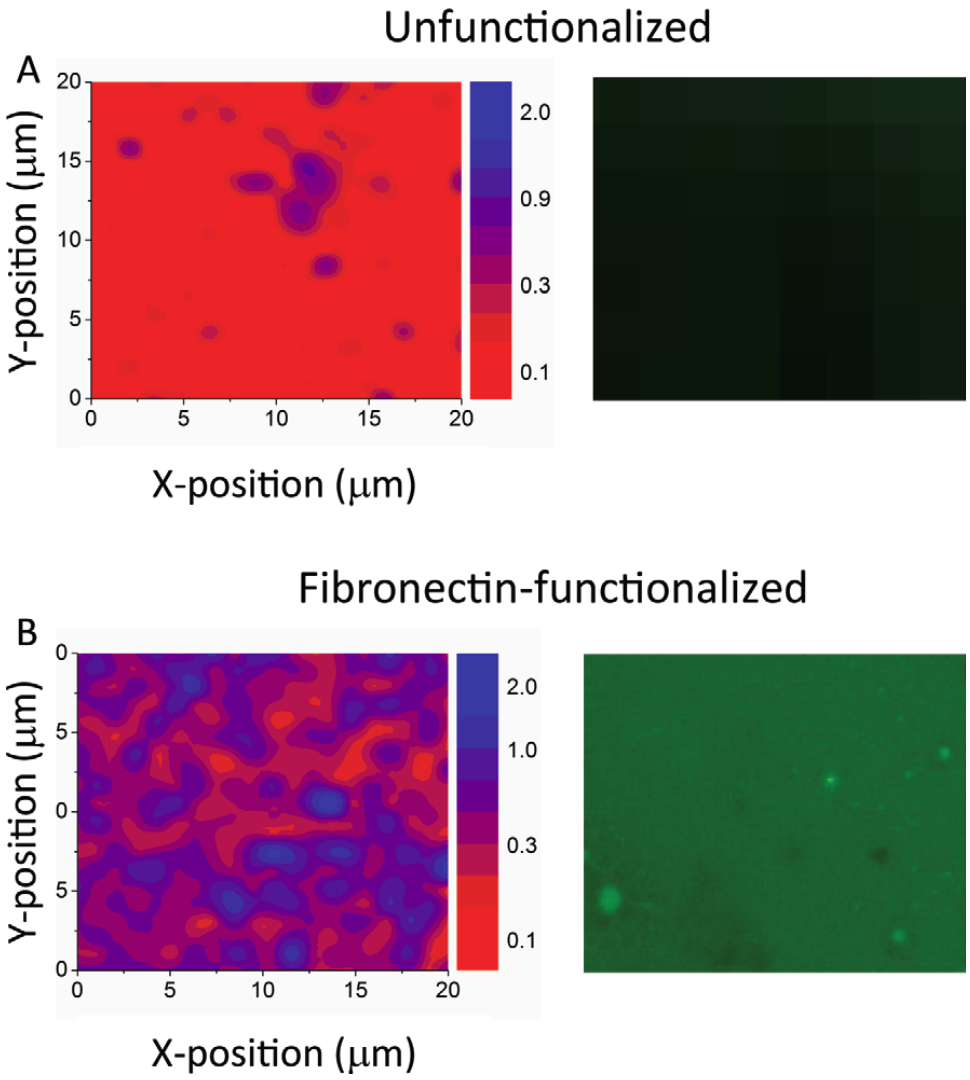

Figure 3.2: The average force maps (left) and fluorescent images (right) of the unfunctionalized and fibronectin-functionalized PA gel for a 20 μm × 20 μm region, respectively. The color scale is shown in nN.

AFM tip as it was retracted from the surface. Low force, charge-based interactions between the tip and unfunctionalized gel do not significant bend the tip but rather resulted in forces driven by thermal fluctuations in the tip (not shown). Force spectrograms from functionalized surfaces contain up to 3 adhesive events (labeled in Figure 3.1B), though the final, largest event corresponds to the force to break the bond between the R457 antibody and fibronectin. This positive quantity is that we call the "adhesion force" between the tip and the substrate.

To confirm the presence of fibronectin prior to indentation, FITC-labeled fibronectin was crosslinked to the substrate (Figure 3.2, right). Force spectroscopy maps averaged from 5 spectrographs of the same 20 × 20 μm region (Figure 3.2, left) show the distribution of the adhesion forces in the area of scan. Average adhesion force for unfunctionalized samples was 60.25 ± 27.18 pN, and was chosen over bovine serum albumin (BSA)-coating (data not shown) to minimize charge-based interactions, which induced only ± 3 nm tip deflection. It is important to note that a few adhesive interactions for the unfunctionalized substrate result in forces larger than 2.0 nN, e.g. the dark blue spot on *Figure 2.2A*, left, due to our effort to minimize non-specific binding via averaging of multiple spectrography and probed regions. On the other hand, the specific interaction between the tip and surface when functionalized with fibronectin was 360.75 ± 163.30 pN (Figure 3.3A), almost 6-fold larger than the unfunctionalized substrate. Though there is a relatively uniform distribution of the fluorescent signal, the percent deviation for the functionalized sample, i.e. the "roughness" of the surface, is ~ 45%. This may be reflective of the small contact area, as determined by the Hertz model to be

< 1 nm^2 [28], which ensured that a minimal number of bonds formed during an adhesion event.

3.3.2 Loading rate and temperature effects

Bond(s) strength between the cells and their substrate likely behave in a similar manner to the bonds form between receptor-coated AFM tips and their immobilized ligand as has been previously shown [29,30]. For such systems, the bonds that form have "catch" characteristics as bond strength can be influenced by the rate of force application, i.e. how quickly the receptor-ligand bond is stressed. To ensure that this mapping technique is probing the adhesive domains of this bond type and not a non-specific interaction between fibronectin and the antibody, the loading rate dependence of the bonds formed during force spectroscopy mapping were tested using rates that varied from 2 – 200 nN/s (Figure 3.3B). For the unfunctionalized gel, the average adhesion forces did not vary dramatically as expected for low force, charge-based interactions. However for the fibronectin-functionalized gel, average adhesion force increased from 4-fold, with a dramatic increase above 20 nN/s indicative of "catch bond" characteristics [29].

Cell-substrate adhesion is typically maintained at physiological temperature, and as such, the lifetime and strength of these bonds would appear to be optimized for this purpose. Regardless of temperature, unfunctionalized gels did not support measurable adhesion (data not shown) while adhesion maps of fibronectin-functionalized gels showed that these gels supported sufficient adhesion both at room and physiological temperature, i.e. 25°C and 37°C respectively (Figure 3.4). At supraphysiological temperature (60°C), adhesion force was statistically similar to unfunctionalized gels.

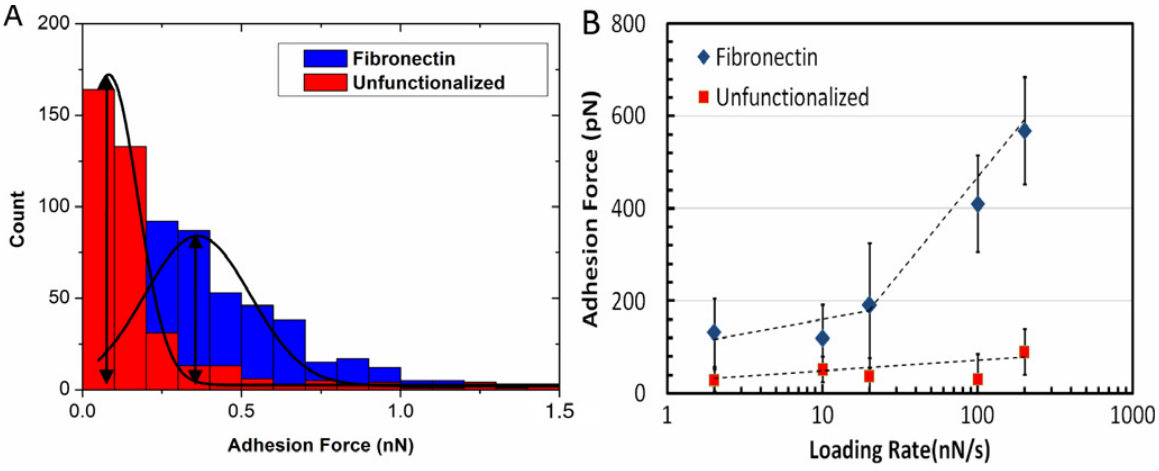

Figure 3.3: (A) Histogram of unfunctionalized (red) and fibronectin-functionalized (blue) PA gel fitted with a Gaussian distribution (n = 400). (B) Average adhesion force plotted against loading rates for the unfunctionalized (red square symbol) and fibronectin-functionalized (blue diamond symbol) PA gel. Error bars indicate the standard deviation. n = 400 forcespectrograms/rate. Data fits were performed with straight lines, though for the functionalized substrate, two separate lines were used to indicate different loading rate dependences.

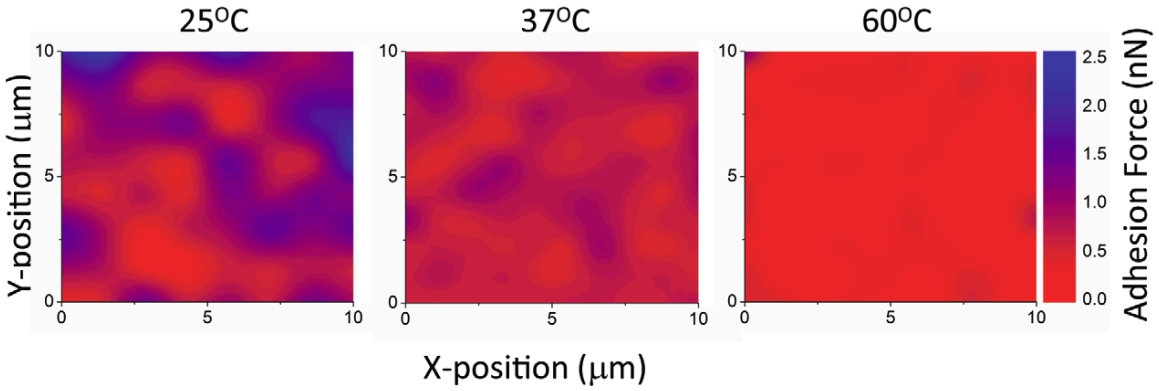

Figure 3.4: The average adhesion force maps from 10 force maps of the fibronectin-functionalized PA gel on a 10 μm × 10 μm region at the temperatures of 25, 37, and 60 °C, left to right respectively.

3.3.3 The Adhesion Map of a Microcontact Printed (μCP) Fibronectin Patterm

A distinct advantage of FSM over fluorescent microscopy techniques or convention force spectroscopy is that it can provide both spatial information about the distribution of adhesive ligand on a substrate and mechanical information about its capacity to bond to ligand. As is often the case, ligand is not uniformly coated on a material or distributed in a 3-dimensional matrix [23]. To demonstrate the ability of FSM to detect these spatial differences in adhesive ligand distribution, a μCP technique [25] was employed to pattern FITC-conjugated fibronectin on a gel (Figure 3.5A), resulting 5 μm × 5 μm fibronectin features (fluorescently shown in Figure 3.5B). The AFM tip was aligned with these surface features and systematically probed (Figure 3.6A; dash red trapezoid) to generate a corresponding adhesion force map (Figure 3.6B) where the dash green squares highlight the adhesive, FITC-conjugated fibronectin pattern. Note that no significant detachment of fibronectin was observed during FSM probing (Supplemental Figure B.1); thus any change in the average force map was not a result of ligand loss. Adhesion forces of the fibronectin features was similar to that found for uniformly functionalized substrates (Figure 3.2B), though the unfunctionalized regions had forces that were 2-fold higher than the uniformly unfunctionalized substrate (Figure 3.2A) and perhaps indicate regions where low levels of fibronectin exist but which are not detectible by light microscopy. Despite the smaller difference in force magnitude, it does appear that FSM could detect features resembling squares as student t-tests of forces from patterned and unpatterned regions were significantly different ($p < 10^{-4}$).

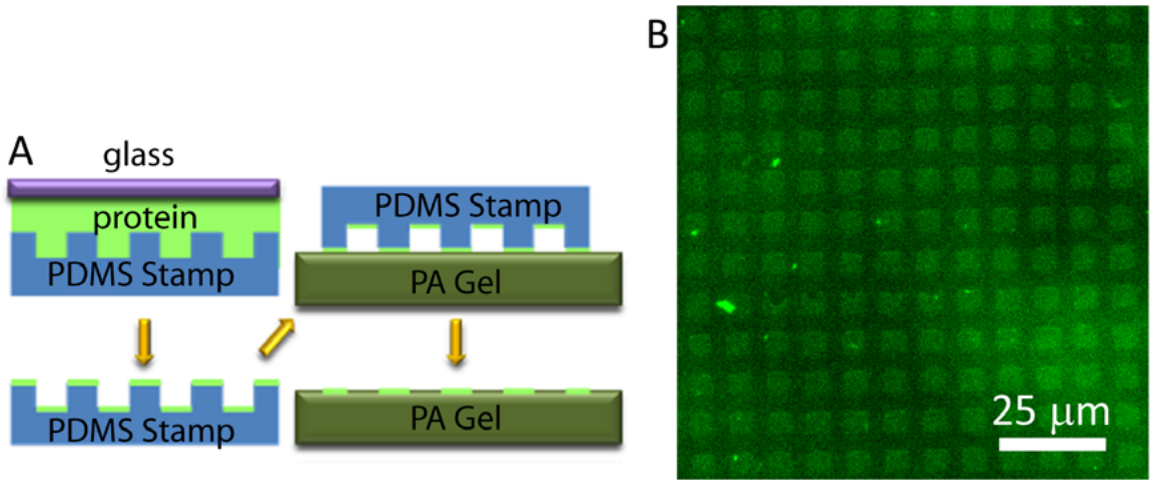

Figure 3.5: (A) Schematic of the technique of microcontact printing (µCP) on the sulfo-SANPAN initiated PA gel. (B) A fluorescent image of the 5 µm × 5 µm fibronectin–FITC patterned PA gel. The scale bar is 25 µm.

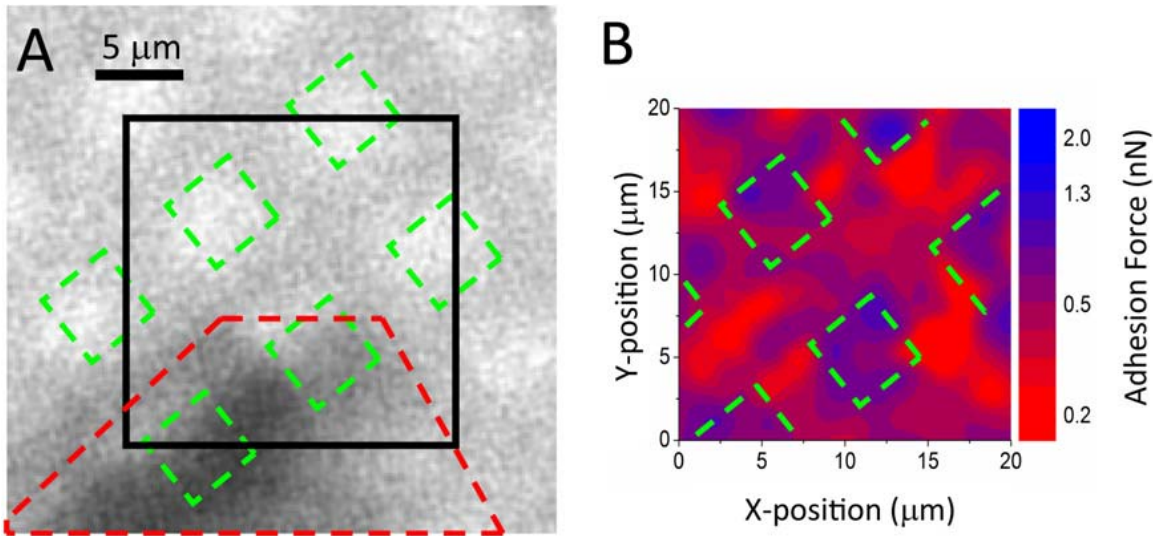

Figure 3.6: (A) Schematic of the pattern beneath the AFM cantilever tip (red dashed trapezoid) indicating the AFM scanning area (black solid rectangle) and fibronectin-functionalized squares (green dashed rectangles). Note that the dark regions in the fluorescent image are due to the cantilever positioned above the substrate. (B) Force spectroscopy map of the substrate using the region shown in part (A) outlined by the solid rectangle line. The average of eight force maps (with a resolution of 1 scan μm^{-2}) was overlaid with the 5 µm × 5 µm fibronectin-functionalized pattern (green dashed lines) from part (A).

3.4 Discussion

3.4.1 Materials with a Distribution of "Sticky" Patches

Our comparison here between a patterned, protein-functionalized material and the material's non-adhesive, unfunctionalized surface emphasizes our ability to recognize patterns at sufficient resolution that has not previously seen [31-34]; it should be noted, however, that our antibody-fibronectin interaction could withstand upwards of 500 pN of force versus low forces from the unfunctionalized surface (Figure 3.3A). Compared to the interaction between previously mapped between bacteria haemagglutinin and heparin [31] and those measured for strepavidin-biotin [35], mycobacterial proteins-fibronectin [32], and normal integrin-ECM bonds [19,20,36], the forces observed here are at least an order of magnitude higher, which may account for improved pattern recognition [22]. Though the higher magnitude, and the presence of single unbinding peaks does not rule out the formation of parallel bonds to achieve higher rupture forces, it further enhances our detection capabilities and emphasizes the differences in forces seen in the patterned substrate, e.g. statistically different force distributions in the functionalized and unfunctionalized regions ($p < 10^{-4}$) typical of the 6-fold force difference between two substrates (Figure 3.2). That said, spectrograms did not indicate tandem events [37], and given typical antibody affinities for R457 [26], this may well represent single antibody-fibronectin bonds.

Unlike the regular array of adhesive islands presented by μCP, most native and synthetic materials do not have a repeating pattern of adhesive regions but instead have a random distribution of ligand. For example, the R-G-D domain of fibronectin is only seen

by cells when fibronectin is unwound and assembled into a fiber in which the 10^{th} type 3 domain is accessible [10,38]. Moreover after cells adhere to ECM, they often actively remodel their matrix, and this further complicates the characterization of cell adhesion site distribution, especially those sub-micron sites which escape detection by conventional microscopy. Yet for matrix with unknown distribution of "sticky" patches or to investigate cells [33], our specific method of FSM can provide improved characterization, determining the distribution of adhesion sites with high lateral resolution of 20 nm (Figure 3.6) as well as being sensitive to small changes in the strength of adhesion by using flexible cantilevers, $k_{sp} \sim 20$ pN/nm (Figure 3.3 and 3.4). However, there may be significant complications provided by the fibrillar structure of these matrices [9,38] and the presence of cells versus a smooth functionalized hydrogel surface. Non-cell adhesive regions of fibronectin may have higher non-specific adhesion forces compared with the unfunctionalized substrate here, making the detection of adhesive features within the matrix less accurate, as with BSA-coating. Using species-specific antibodies could overcome such a limitation; force spectrograms using a human-specific fibrinogen antibody could detect 5-fold force differences between human fibrinogen and BSA [39] compared to our pan-fibronectin antibody recognizing the 70kD amino terminal end of most fibronectin species [26].

3.4.2 Exploiting Dynamic Responses and Specificity of the Antibody-Fibronectin Bond for FSM:

As with other biological receptor-ligand interactions, e.g streptavidin-biotin [29], fibronectin does not have the ideal, single energy barrier, and thus as loading rate of the tip increases, the rupture force increase is non-linear [40]. Thus this transition in rupture force, which was observed at 20 nN/s here (Figure 3.3B), is the result of a change in the inner activation barrier of the complex [36], which also occurs in other complex bonds such as mycobacterial proteins-fibronectin bonds [32] and integrin-fibronectin bonds [36]. In other words when the fibronectin-antibody bond forms, it induces a conformational change in the proteins which stabilizes their ability to resist increasing force when applied faster. Formally, this behavior is predicted by the Bell model of adhesion [41,42], where the antibody-fibronectin bond illustrates a catch bond. The strong non-covalent interaction between the antibody and its 70 kD target [26] likely confers a similar conformational change as with fibronectin-integrin binding [36]. Thus we are able to produce up to a 6-fold difference in adhesion force to aid in our ability to recognize surfaces features. It is important to note that this transition state is intrinsic to the specific interaction; while we previously noted the fibronectin interaction transitions at 20 nN/s [36], the streptavidin-biotin transition occurs at 1 nN/s [35]. Thus feature detection with other molecules may be easier as is the case with lower transition bonds such as streptavidin-biotin or more difficult with bonds whose transition state is higher. Fortunately for the detection of cell adhesion molecules on a material, many cell-ECM [22,36] and specific cell-cell bonds, e.g. E-cadherin [43] but not N-cadherin [30], have

bond transition states so that sufficient loading rates can produce maximal differences in bond forces between functionalized and unfunctionalized regions of the substrate. Continually increasing the loading rate to further exploit this difference appears plausible, however the Bell model [41,42] indicates that there is a limit to the loading rate due to the surrounding solution's viscous damping [44]. The transition state for fibronectin amplifies our ability to recognize patterns at high resolution and with high fidelity unlike previous spectroscopy or pattern mapping studies as summarized in Table 3.1. On the other hand, many simple chemical bonds between functional groups [40] or with alkanethiol bonds [34] lack this transition and would not be as easily mapped.

Bonds have specific lifetimes and affinities, and to increase detectability, the antibody-fibronectin bond was chosen. Contact duration between the tip and sample surface has also been used to increase adhesive interactions [48]. Here contact duration was fixed at 3 seconds, resulting in 74% of the binding events producing forces 2-fold higher than the average non-specific binding force. However, Lü and coworkers found that contact time greater than 500 ms does not shift peak force [48], and while force saturation is likely dependent on the particular bond, it nonetheless indicates that contact time is not as critical a factor with high affinity bonds as are other parameters, e.g. loading rate. Minimizing contact time should decrease scan time while not sacrificing mapping resolution.

Table 3.1: Evolution of the Force Spectroscopy Mapping Technique
A subset of the relevant results for adhesion-based spectroscopy mapping summarized in Table 3.1 show our ability to measure a transition state in full length fibronectin binding, which previously has not been observed. Using higher loading rates, we can then detect micro-sized feature patterns with the high resolution of other studies but using fibronectin and imaging with much higher fidelity.

Measurement	Adhesion	Rupture Force	Lateral Map Resolution	Patterned Feature Recognition	Citation
Force Spectroscopy	Avidin-Biotin	Multiples of 160 ± 20 pN	-	-	[21]
	Streptavidin-Biotin	Force transition state at 1 nN/s	-	-	[35]
	Fibronectin- *S. epidermidis*	No force transition state, 100's of pN rupture force	-	-	[45]
	Fibronectin–α5β1 integrin	Force transition state at 10 nN/s	-	-	[36]
	Fibronectin–heparin	No force transition state, 100's of pN rupture force	-	-	[46]
Force Spectroscopy Mapping	Patterned carboxyl and methyl groups	8.7 ± 3.2 nN for carboxyl groups	25/μm^2	Yes, tens of micron-sized features	[40]
	Streptavidin-Biotin	~ 1 nN	~10/μm^2	Yes, micron-sized features	[47]
	Haemagglutinin-heparin on mycobateria	50 ± 23 pN and 117 ± 18 pN for single and double rupture	400/μm^2	Not able to determine	[31]
	Hydrophobic tip interaction with *Aspergillus fumigatus*	3.0 ± 0.4 nN	400/μm^2	Yes, micron-sized features	[34]
	Agglutinin-Epidermal Growth Factor Receptor in Caco-2 cells	Modal value of 125 pN	<1/μm^2	Yes, tens of micron-sized features	[33]
	Mycobacteria-fibronectin associated proteins	52 ± 19 pN	400/μm^2	Not able to determine	[32]
	Fibronectin-R457 antibody	Force transition state at 20 nN/s and maximum rupture force of 2.44 nN	400/μm^2	Yes, micron-sized features where $p < 10^{-4}$	Current study

3.5 Conclusion

High resolution FSM using loading rates above the receptor-ligand transition point as presented here is a useful technique to accurately determine the spatial variation of material components within a substrate where such variation is not known. Moreover coupling FSM with conventional fluorescence microscopy can further enhance our understanding of complex materials and how cellular responses are dictated by the arrangement of adhesive ligand.

3.6 Acknowledgements

This chapter is published, in full, is a reprint of the published article in *Journal of Physics: Condensed Matter*, volume 22, number 19, May 2010, The dissertation author is the primary author of this paper. We would like to thank Dr. Nicholas Geisse (Asylum Research; Santa Barbara, CA) for technical assistance as well as Dr. Dayu Teng for microcontact printing. The author acknowledges funding from funding from EPSRC (EP/E03103X/1) and the Royal Thai Government Fellowship (to SC) and a grant from NIH #1DP02OD10322765 (to AJE).

3.7 References:

1 Li, S. et al. (2005) Biochemistry and Biomechanics of Cell Motility. *Annual Review of Biomedical Engineering* 7 (1), 105-150

2 Chien, S. et al. (2005) Molecular basis of mechanical modulation of endothelial cell migration. *Front Biosci* 10, 1985-2000

3 Hinz, B. and Gabbiani, G. (2003) Cell-matrix and cell-cell contacts of myofibroblasts: role in connective tissue remodeling. *Thromb Haemost* 90 (6), 993-1002

4 Sharma, R.I. et al. (2008) Nanoscale variation of bioadhesive substrates as a tool for engineering of cell matrix assembly. *Tissue Eng Part A* 14 (7), 1237-1250

5 Ingber, D.E. (2008) Can cancer be reversed by engineering the tumor microenvironment? *Seminars in Cancer Biology* 18 (5), 356-364

6 Kumar, S. and Weaver, V.M. (2009) Mechanics, malignancy, and metastasis: the force journey of a tumor cell. *Cancer Metastasis Rev* 28 (1-2), 113-127

7 Engler, A.J. et al. (2009) Multiscale Modeling of Form and Function. *Science* 324 (5924), 208-212

8 Chiquet, M. et al. (2009) From mechanotransduction to extracellular matrix gene expression in fibroblasts. *Biochimica et Biophysica Acta (BBA) - Molecular Cell Research* 1793 (5), 911-920

9 Hay, E.D. (1991) *Cell biology of extracellular matrix*, Plenum Press

10 Ruoslahti, E. and Pierschbacher, M.D. (1987) New perspectives in cell adhesion: RGD and integrins. *Science* 238 (4826), 491-497

11 Puklin-Faucher, E. and Sheetz, M.P. (2009) The mechanical integrin cycle. *J Cell Sci* 122 (Pt 2), 179-186

12 Engler, A.J. et al. (2009) A novel mode of cell detachment from fibrillar fibronectin matrix under shear. *J Cell Sci* 122 (Pt 10), 1647-1653

13 Shao, J.Y. et al. (2004) Quantifying cell-adhesion strength with micropipette manipulation: principle and application. *Front Biosci* 9, 2183-2191

14 Griffin, M.A. et al. (2004) Patterning, prestress, and peeling dynamics of myocytes. *Biophys J* 86 (2), 1209-1222

15 Gallant, N.D. et al. (2005) Cell adhesion strengthening: contributions of adhesive area, integrin binding, and focal adhesion assembly. *Mol Biol Cell* 16 (9), 4329-4340

16 Friedland, J.C. et al. (2009) Mechanically activated integrin switch controls alpha5beta1 function. *Science* 323 (5914), 642-644

17 Dufrene, Y.F. and Hinterdorfer, P. (2008) Recent progress in AFM molecular recognition studies. *Pflugers Arch* 456 (1), 237-245

18 Ludwig, T. et al. (2008) Probing cellular microenvironments and tissue remodeling by atomic force microscopy. *Pflügers Archiv European Journal of Physiology* 456 (1), 29-49

19 Jiang, G. et al. (2003) Two-piconewton slip bond between fibronectin and the cytoskeleton depends on talin. *Nature* 424 (6946), 334-337

20 Sun, Z. et al. (2005) Mechanical properties of the interaction between fibronectin and alpha5beta1-integrin on vascular smooth muscle cells studied using atomic force microscopy. *Am J Physiol Heart Circ Physiol* 289 (6), H2526-2535

21 Florin, E.L. et al. (1994) Adhesion forces between individual ligand-receptor pairs. *Science* 264 (5157), 415-417

22 Muller, D.J. et al. (2009) Force probing surfaces of living cells to molecular resolution. *Nat Chem Biol* 5 (6), 383-390

23 Reilly, G.C. and Engler, A.J. (in press) Intrinsic Extracellular Matrix Properties Regulate Stem Cell Differentiation. *J Biomechanics*

24 Engler, A.J. et al. (2007) Microtissue Elasticity: Measurements by Atomic Force Microscopy and Its Influence on Cell Differentiation. In *Methods in Cell Biology* (Vol. Volume 83), pp. 521-545, Academic Press

25 Tien, J. and Chen, C.S. (2002) Culture Environments: Microarrays. In *Methods of tissue engineering*, pp. 113-120, Academic Press

26 Aguirre, K.M. et al. (1994) Fibronectin self-association is mediated by complementary sites within the amino-terminal one-third of the molecule. *Journal of Biological Chemistry* 269 (45), 27863-27868

27 Bonanni, B. et al. (2005) Single Molecule Recognition between Cytochrome C 551 and Gold-Immobilized Azurin by Force Spectroscopy. *Biophysical Journal* 89 (4), 2783-2791

28 Rotsch, C. et al. (1999) Dimensional and mechanical dynamics of active and stable edges in motile fibroblasts investigated by using atomic force microscopy. *Proc Natl Acad Sci U S A* 96 (3), 921-926

29 Merkel, R. et al. (1999) Energy landscapes of receptor-ligand bonds explored with dynamic force spectroscopy. *Nature* 397 (6714), 50-53

30 Shi, Q. and Boettiger, D. (2003) A Novel Mode for Integrin-mediated Signaling: Tethering Is Required for Phosphorylation of FAK Y397. *Mol. Biol. Cell* 14 (10), 4306-4315

31 Dupres, V. et al. (2007) Probing molecular recognition sites on biosurfaces using AFM. *Biomaterials* 28 (15), 2393-2402

32 Verbelen, C. and Dufrene, Y.F. (2009) Direct measurement of Mycobacterium-fibronectin interactions. *Integrative Biology* 1 (4), 296-300

33 Gunning, A.P. et al. (2008) Mapping specific adhesive interactions on living human intestinal epithelial cells with atomic force microscopy. *FASEB J.* 22 (7), 2331-2339

34 Dague, E. et al. (2007) Chemical force microscopy of single live cells. *Nano Lett* 7 (10), 3026-3030

35 Yuan, C. et al. (2000) Energy Landscape of Streptavidin-Biotin Complexes Measured by Atomic Force Microscopy *Biochemistry* 39 (33), 10219-10223

36 Li, F. et al. (2003) Force Measurements of the α5β1 Integrin Fibronectin Interaction. *Biophysical Journal* 84 (2), 1252-1262

37 Law, R. et al. (2003) Cooperativity in forced unfolding of tandem spectrin repeats. *Biophys J* 84 (1), 533-544

38 Mao, Y. and Schwarzbauer, J.E. (2005) Fibronectin fibrillogenesis, a cell-mediated matrix assembly process. *Matrix Biol* 24 (6), 389-399

39 Agnihotri, A. and Siedlecki, C.A. (2005) Adhesion mode atomic force microscopy study of dual component protein films. *Ultramicroscopy* 102 (4), 257-268

40 Frisbie, C.D. et al. (1994) Functional Group Imaging by Chemical Force Microscopy. *Science* 265 (5181), 2071-2074

41 Bell, G.I. (1978) Models for the specific adhesion of cells to cells. *Science* 200 (4342), 618-627

42 Evans, E. and Ritchie, K. (1997) Dynamic strength of molecular adhesion bonds. *Biophysical Journal* 72 (4), 1541-1555

43 Panorchan, P. et al. (2006) Probing Intercellular Interactions between Vascular Endothelial Cadherin Pairs at Single-molecule Resolution and in Living Cells. *Journal of Molecular Biology* 358 (3), 665-674

44 Siria, A. et al. (2009) Viscous Cavity Damping of a Microlever in a Simple Fluid. *Physical Review Letters* 102 (25), 254503-254504

45 Bustanji, Y. et al. (2003) Dynamics of the interaction between a fibronectin molecule and a living bacterium under mechanical force. *Proc Natl Acad Sci U S A* 100 (23), 13292-13297

46 Mitchell, G. et al. (2007) Single-molecule dynamic force spectroscopy of the fibronectin-heparin interaction. *Biochem Biophys Res Commun* 364 (3), 595-600

47 Ludwig, M. et al. (1997) Atomic force microscope imaging contrast based on molecular recognition. *Biophys J* 72 (1), 445-448

48 Lü, S. et al. (2006) Quantifying the effects of contact duration, loading rate, and approach velocity on P-selectin-PSGL-1 interactions using AFM. *Polymer* 47 (7), 2539-2547

Chapter 4

Adhesive Nanodomain on Block Copolymer-Based Materials Detected by Chemical Force Spectroscopy Mapping

4.1 Introduction

As known, they are many factors or cues influence cell response, namely, chemical, physical, and chronological cues. The chemical cue is one of the most well known to stimulate cell behaviors, like chemical concentration of growth factors [1], adhesive strength [2], and extracellular protein composition [3]. Most reports assume that substrate properties are homogeneous, i.e. the properties are the same entire system of interest such as pressure and chemical concentration in a bioreactor or tissue culture plate, substrate hydrophobicity, and protein distribution on hydrogels. As recent

establishments of techniques such as microcontact printing [4,5], self-assembly diblock copolymer immobilization [6], and photolithography [7,8], cell engineers can employ the heterogeneous biophysical properties down to cellular scale to regulate cell behaviors. However, the existence of chemical heterogeneity is assumed from the topographical images like scanning electron micrographs (SEM) or atomic force micrographs (AFM).

Another technique applied for forming patterns on surface is diblock copolymer-based polymersome synthesis [9,10] – the fabrication of vesicles or micelles formed from diblock copolymers in liquid. Based on hydrophobic and hydrophilic conformity, block copolymer chains will turn the hydrophobic part against water, meanwhile the hydrophilic one towards water. This will form micelles made from block copolymer. If there are 2 block copolymers in aqueous solution, micelles will be hybrid with 2 surfactants in one micelle [11]. Simplified that there are block copolymer AB and CB which A and C are hydrophilic, while B is hydrophobic. So after forming micelles, A and C will be distributed and form patchy-like structure on the outer surface of polymersome. If in oil solution, in vice versa, the patchy A-C will form on the inner surface. Analogically if consider at the interface between water and oil layer, the film of the block copolymers would be formed. This could also form the heterogeneity of surface chemistry. The polymersome investigated by fluorescent microscopy has shown the pattern with the area of square micron [12], meanwhile using transmission electron microscope (TEM) shows in nanoscale pattern [13]. To detect this chemical topology, high resolution detection like AFM-based would be an optional. AFM-based technique, not only the topography but also the chemical information could be drawn. With a chemical-coated probe, AFM-based technique, called chemical force spectroscopy, can

Table 4.1: Diblock copolymer foam compositions.

Name	PS-PEO molar fraction	PS-PAA molar fraction
PEO100	100	0
PEO75	75	25
PEO50	50	50
PEO25	25	75
PAA100	0	100

measure the interaction between probe and substrate chemicals such as hydrophobic [14] or protein-ligand interaction [15]. AFM therefore would be an option to investigate the chemical existence corresponding to positions.

Herein macromolecular surfactants consisting of amphiphilic block copolymers polystyrene-b-poly(ethylene oxide) (PS-PEO) and/or polystyrene-b-poly(acrylic acid) (PS-PAA), which we have previously demonstrated in vesicles undergo interface confined phase separation [13,16] will be established. The chemical force spectroscopy mapping (CFSM) developed elsewhere [17] will be employed on the films of PS-PEO and PS-PAA.

4.2 Materials and Methods

4.2.1 Preparation of BCP 2D films

The two dimensional (2D) films of PS-PEO and PS-PAA copolymer preparation employs the molar ratios indicated in Table 4.1. Briefly, the aqueous phase, consisting of 0.1 wt/wt % potassium persulfate initiator, was added to a glass vial using a syringe. The oil phase (monomer of PS + block copolymer surfactants of PS-PEO/PAA) was then carefully layered on top of the aqueous phase to maintain phase separation. The copolymer mixtures were then allowed to adsorb at the oil-water interface for 24 hours without agitation and then polymerized at 60 °C for 24 hours. The resulting films were washed extensively with deionized water, left in ethanol for 1 week to remove unreacted monomers, and dried before analysis.

4.2.2 Chemical force spectroscopy mapping (CFSM)

CFSM provides adhesive force maps generated by measuring the rupture force between bonds that form between a functionalized tip and the surface. As shown in Supplemental Figure C.2a, tips were functionalized by poly-L-lysine (PLL, M_w 1000-5000, Sigma-Aldrich) based on a technique described elsewhere [17]. Briefly, AFM tips were cleaned by chloroform and immersed in 5 M ethanolamine-hydrocholide in dimethyl sulfoxide (Sigma Aldrich) overnight. After washing with phosphate-buffered saline (PBS), cantilevers were immersed in 25 mM BS3 (bis[sulfosuccinimidyl] suberate; Pierce) for 30 min. After washing again with PBS, cantilevers were then immerged in 1 mg/ml poly-L-lysine for 30 min. All steps were done at room temperature. Functionalized

cantilevers were air-dried and kept in 4°C until use. CFSM was performed on the MFP3D-BIO atomic force microscope (AFM, Asylum Research) to measure the adhesive interactions with films maintained at pH 9 overnight and immerged in pH 7 immediately before tested. Force curves were generated with a 2 μm/s approach velocity, 1 nN surface trigger force, 3 second dwell time between tip indentation and retraction, and a 32 × 32 scan resolution over 2 × 2 and 20 × 20 μm scan areas (resolutions of 62.5 and 625 nm, respectively). Typical force curves for interactions without (top) and with adhesion (bottom) are shown in Supplemental Figure C.2b. Area fraction and domain surface areas were determined using ImageJ software from a thresholding scheme described below.

4.2.3 X-ray Photoelectron Spectroscopy (XPS)

Surface analysis was carried out with a Kratos Ultra DLD X-ray photoelectron spectrometer. A monochromated Al Kα X-ray source at a power of 150 W was used. The spot size was 300 μm by 700 μm. The pressure in the main ultra-high vacuum chamber was maintained below 1 x 10^{-8} mbar for all samples. As the polymers analyzed here are electrical insulators, charge neutralization was required to prevent positive charge build up on the substrate's surface; an electron flood gun was focused onto the sample to compensate for the positive charging effect. High-resolution spectra of the elemental core level C 1s were also completed to assess surface carbon. The parameters used were a binding energy range of 275 to 300 *eV,* a pass energy of 20 *eV* and a step interval of 0.1 *eV.* All data collected was then analyzed using CasaXPS software peaks were again fitted by removing unwanted background using CasaXPS software. Asymmetry of the peaks was fixed at zero and the position of each peak was fixed relative to the hydrocarbon

peak. After initial rough automatic peak fitting, the carbonyl peak was then moved slightly to obtain a good fit of the C 1s line scan. Subsequent carbon functional group peaks were then calculated from the total of the C 1s peak to give the carbon environment composition.

4.2.4 Contact Angle Measurements

Scaffold hydrophobicity was ascertained by determining the water contact angle with the substrate using a Ramé-Hart contact angle goniometer. 2 - 4 μL droplets of neutral (pH 7) and acidic (pH 2.2) deionized water (pH 7) were used. Measurements were made in triplicate for each sample.

4.2.5 Statistical Analysis

All values are shown as averages ± their standard deviation. The analysis of variance (ANOVA) was performed as indicated between the 5 combinations of PS-PAA/PS-PEO foams with 3 replications of each combination.

4.3 Results and Discussion

4.3.1 Surface chemistry modification of films

High-resolution x-ray photoelectron spectra (XPS) C 1s spectra were made for single copolymer foams, i.e. PEO100 and PAA100. For PEO100, the C-O signal, detected at 285.0 *eV*, overlaps with hydrocarbon C-C and C-H bonds, making identification difficult (Figure 4.1b, top). For PAA100 however, data confirms the COOH

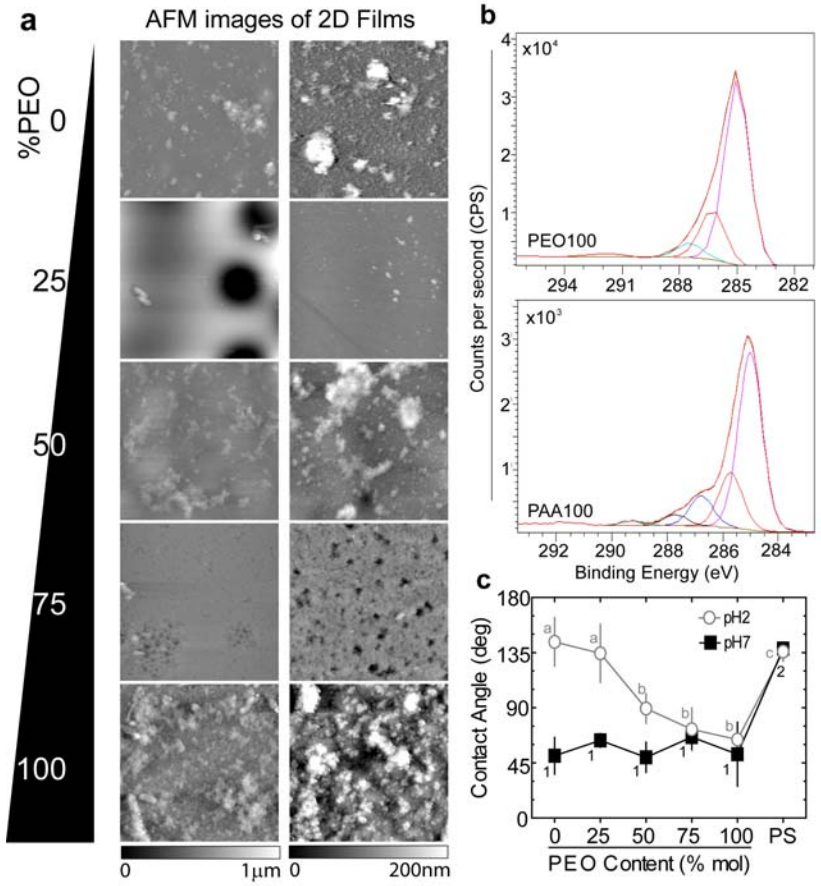

Figure 4.1: Morphologies of Porous Foams and Films. a) AFM topographs of films from 20 x 20 (left) and 2 x 2 μm scans (right). Image colormap ranges are 0 – 1 μm and 0 – 200 nm. b) X-ray photoelectron spectra of foams containing only polystyrene-b-poly(ethylene oxide) or polystyrene-b-poly(acrylic acid) copolymers, i.e. PEO100 and PAA100, respectively. c) Average contact angles of pH 2 (open circles) and pH 7 (closed squares) deionized water on 3D foams as a function of the molar ratio of polystyrene-b-poly(ethylene oxide). Mean comparisons of one group versus all samples have the same symbol, e.g. 1, 2, a, b and c. 1p <0.05 from pure polystyrene foams. 2p <0.05 from all other foams at pH 7. ap <0.05 from other mixed composition foams but not polystyrene. bp <0.05 from other copolymer-containing and pure polystyrene foams. cp <0.05 from mixed composition foams PEO50 through PEO100.

group's presence with a distinctive shoulder at 287 *eV* and a smaller peak appearing at higher energy 289 *eV* corresponding to the α carbon (C-COOH) and C=O double bonds, respectively (Figure 4.2b, bottom). To further confirm bulk surface composition, contact angle measurements were employed to investigate composition-dependent changes in macroscopic foam wettability, which can be tuned by pH. At pH 7, contact angles for all block copolymer compositions are significantly lower than the polystyrene/divinyl-benzene only film, e.g. SPAN80. Since polyacrylic acid has a pKa of about 4, its side groups make it hydrophilic and hydrophobic in pH above and below its pKa, respectively. As shown in Figure 4.1c at pH 2, high PAA-containing foams have a more hydrophobic surface than high PEO-containing foams and are similar in hydrophobicity to polystyrene.

4.3.2 Surface topology characterization of BCP 2D films

Homogenous surface chemistry does not mimic the natural adhesive heterogeneity of matrix [18] and might result in less inductive matrix for stem cells. As such, we investigated to what extent mixtures of cell adhesive PAA [19] and cell inert PEO [20] block copolymer could undergo interface-confined phase separation in foam morphologies versus the surface domains we have previously observed in amphiphilic polymersomes [13,21]. While bulk metrics identify composition (Figure 4.1), they cannot identify copolymer phase segregation, and fluorescent detection is complicated by spatial resolution limitations [13]. Chemical force spectroscopy mapping (CFSM) uses a functionalized AFM probe (Supplemental Figure C.2a) to monitor adhesion forces between the probe and film (Supplemental Figure C.2b). Poly-L-lysine (PLL)-

functionalized probes mapped adhesive interactions with films of different diblock copolymer composition at 62.5 nm lateral resolution. Though films were maintained at pH 9 to deprotonate PAA and increase its PLL adhesion, PEO100 films appeared to be substantially more adhesive than PAA100 (Supplemental Figure C.3), perhaps due to counter ion screening of the PAA-PLL electrostatic interaction. This may be plausible since negative charges can be screened by free salt typical in quasi-neutral brushes [22] and indicating that PAA chains may have a dense brush configuration [23]. Regardless, differential probe interactions allow us to map the different domains. By defining adhesion as any value above one standard deviation below the PEO100 film's average adhesion, more than 84% of PEO sights could be identified. Conversely, this threshold correctly identifies nearly all of the PAA100 film's surface (Supplemental Figure C.3, shaded box) and is illustrated again as the grey shaded area in Figure 4.2b. Using this threshold, CFSM maps and adhesive force histograms were generated for 2 × 2 (Figure 4.2a, right) and 20 × 20 μm scan sizes (Supplemental Figure C.4) for the indicated copolymer compositions to show PEO- (white) and PAA-containing (black) regions. For both scan sizes, PEO area fraction reflected the same increasing trend as in bulk, namely higher PEO content yields a higher adhesive area fraction (Figure 4.2c). Domain surface area, defined as a cluster of 4 identical and contiguous observations, were measured from adhesion maps and found to vary from 0.06 to 3.78 μm^2 for PEO (opened squares) and 2.04 to 0.02 μm^2 for PAA (solid circles) as PEO mole fraction increased. ANOVA analysis clearly indicated that low (PAA100 and PEO25) and high (PEO75 and PEO100) PEO mole fraction behaved similarly, reflecting domains of either PEO or PAA, respectively. The force maps suggest typical bimodal (PEO75, PEO25) and spinodal

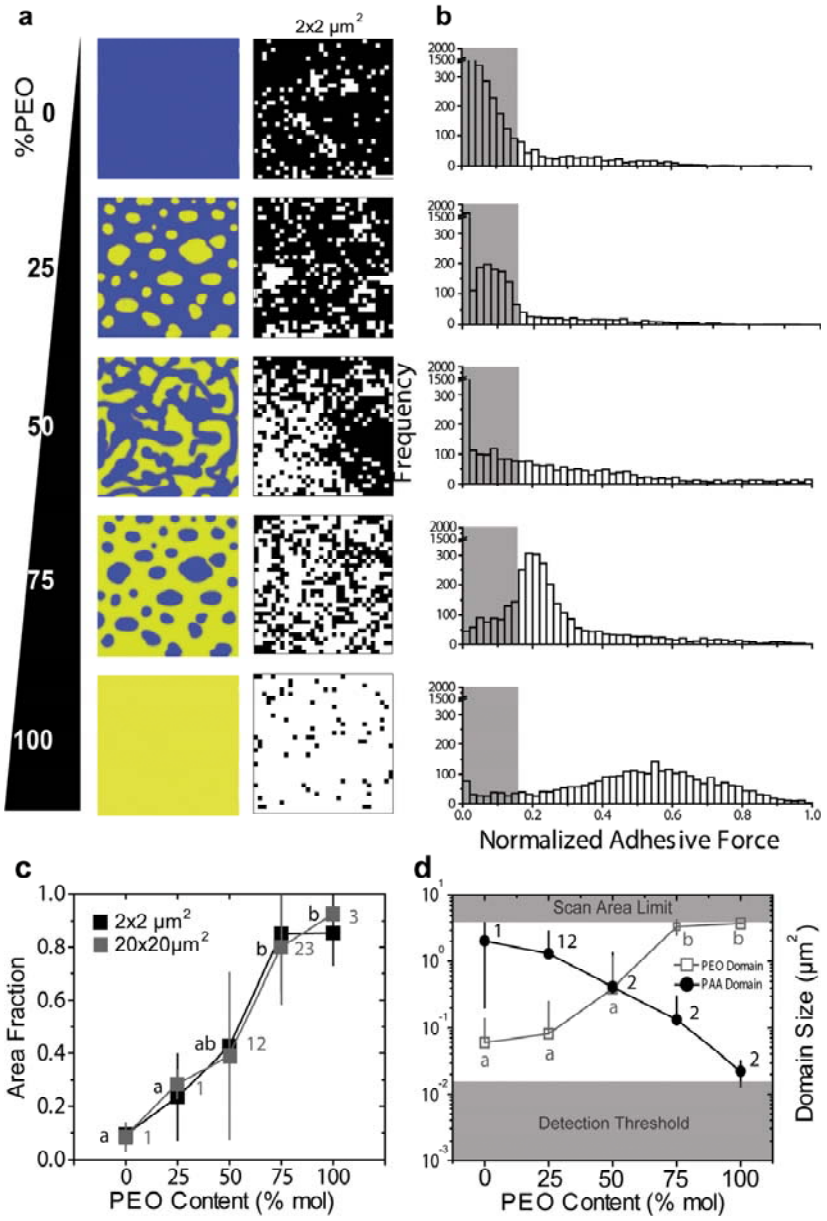

Figure 4.2: Film Characterization by Chemical Force Spectroscopy Mapping. a) Ideal (left) and experimental (right) adhesion images of the distribution of PS-PAA (blue and black regions, respectively) and PS-PEO (yellow and white regions, respectively) shown for a 2 x 2 μm scan area with a resolution of 32 x 32 points. b) Normalized adhesive force distribution as a function of the molar ratio of PS-PEO for all samples. The shaded regions correspond to the threshold for PAA determined in Supplemental Fig. 3. c) Average PS-PEO area fraction as a function of the PS-PEO mole percent. d) Average domain surface area of PS-PAA (closed circles) and PS-PEO (open circles). Scan limit indicates the maximum area of the scan and the detection limit is the area of four adjacent measurements. Mean comparisons of one group versus all samples have the same symbol, e.g. 1, 2, a, and b with $p < 0.05$ versus all data not in the group.

(PEO50) decomposition patterns as represented by the schematic (Figure 4.2a, left). In addition to domain surface area, inter-domain spacing was also determined between all domains within a given image, e.g. Supplemental Figure C.5a showing PAA domain spacing in PEO75 films; when examining PEO domains, minimum spacing was greatest when the PEO mole fraction was lowest (Supplemental Figure C.5b). Thus with increasing PEO composition, domain spacing decreases while size increases (Supplemental Figure C.5c).

4.4 Conclusion

The films of PS-PEO/PS-PAA diblock copolymer surfactants have been characterized. The topographs show no difference in range of 200 nm, meanwhile surface chemistry is different according to % PEO content. XPS technique reveals the existence of PEO and PAA, moreover the contact angles are distinct at pH 2. CFSM shows trend of area fractions and nanodomain of PEO and PAA corresponding to PEO content. The chemical nanodomains are down to subcellular scale (magnitude of 10 μm^2). This would control cell adhesion and differentiation which will be intensively investigated in chapter 5.

4.5 Acknowledgement

In chapter 4 and 5, the manuscript has been submitted. The dissertation author is the co-primary auther with Priyalakshmi Viswanathan and thanks co-authers Kamolchanok Ngamkham and Dr. Giuseppe Battaglia. The author also thanks Dr.

Gwendolen Reilly (University of Sheffield) for fruitful discussions, Dr. Nicholas Geisse (Asylum Research; Santa Barbara, CA) for technical support, and Dr. Adrian Boatwright (University of Nottingham) for XPS assistance. This work was supported by grants from the National Institutes of Health (1DP02OD006460 to Dr. Adam J. Engler), Human Frontiers Science Program (RGY0064/2010 to Dr. Adam J. Engler and Dr. Guiseppe Battaglia), and the Engineering and Physical Sciences Research Council (EP/F019750/1). Pre-doctoral fellowship support was also provided by the Royal Thai Government Science and Technology (to Somyot Chirasatitsin).

4.6 References

1 Vemuri, M.C. et al. (2011) Mesenchymal stem cell assays and applications. *Methods Mol Biol* 698, 3-8

2 Ayala, R. et al. (2011) Engineering the cell-material interface for controlling stem cell adhesion, migration, and differentiation. *Biomaterials* 32 (15), 3700-3711

3 Flaim, C.J. et al. (2005) An extracellular matrix microarray for probing cellular differentiation. *Nat Methods* 2 (2), 119-125

4 Lehnert, D. et al. (2004) Cell behaviour on micropatterned substrata: limits of extracellular matrix geometry for spreading and adhesion. *J Cell Sci* 117 (Pt 1), 41-52

5 Bernard, A. et al. (2000) Microcontact Printing of Proteins. *Advanced Materials* 12 (14), 1067-1070

6 Spatz, J.P. et al. (2007) Molecular Engineering of Cellular Environments: Cell Adhesion to Nano-Digital Surfaces. In *Methods in Cell Biology* (Vol. Volume 83), pp. 89-111, Academic Press

7 Blawas, A.S. and Reichert, W.M. (1998) Protein patterning. *Biomaterials* 19 (7-9), 595-609

8 Sorribas, H. et al. (2002) Photolithographic generation of protein micropatterns for neuron culture applications. *Biomaterials* 23 (3), 893-900

9 Discher, B.M. et al. (1999) Polymersomes: Tough Vesicles Made from Diblock Copolymers. *Science* 284 (5417), 1143-1146

10 Smart, T. et al. (2008) Block copolymer nanostructures. *Nano Today* 3 (3â€“4), 38-46

11 LoPresti, C. et al. (2009) Polymersomes: nature inspired nanometer sized compartments. *J. Mater. Chem.* 19 (22), 3576-7166

12 Christian, D. et al. (2009) Spotted vesicles, striped micelles and Janus assemblies induced by ligand binding. *Nature materials* 8 (10), 843-852

13 LoPresti, C. et al. (2011) Controlling polymersome surface topology at the nanoscale by membrane confined polymer/polymer phase separation. *ACS Nano* 5 (3), 1775-1784

14 Feldman, K. et al. (1998) Toward a force spectroscopy of polymer surfaces. *Langmuir* 14 (2), 372-750

15 Yuan, C. et al. (2000) Energy landscape of streptavidin-biotin complexes measured by atomic force microscopy. *Biochemistry* 39 (33), 10219-10242

16 Battaglia, G. et al. (2011) Wet nanoscale imaging and testing of polymersomes. *Small* 7 (14), 2010-2015

17 Chirasatitsin, S. and Engler, A.J. (2010) Detecting cell-adhesive sites in extracellular matrix using force spectroscopy mapping. *J Phys Condens Matter* 22 (19), 194102

18 Reilly, G.C. and Engler, A.J. (2010) Intrinsic extracellular matrix properties regulate stem cell differentiation. *J Biomech* 43 (1), 55-62

19 Lee, K.Y. (2001) Hydrogels for Tissue Engineering. *Chemical Reviews* 101 (7), 1869-1880

20 Liu, S.Q. et al. (2009) Synthetic hydrogels for controlled stem cell differentiation. *Soft Matter* 6, 67-81

21 Massignani, M. et al. (2009) Controlling cellular uptake by surface chemistry, size, and surface topology at the nanoscale. *Small* 5 (21), 2424-2432

22 Israels, R. et al. (1994) On the Theory of Grafted Weak Polyacids. *Macromolecules* 27 (11), 3087-3093

23 Ballauf, M. and Borisov, O. (2006) Polyelectrolyte Brushes. *Current opinion in Colloid & Interface Science* 11 (6), 316-323

Chapter 5

Adhesive Nanodomain on Block Copolymer-Based Materials Effects Mesenchymal Stem Cell Fates

Abstract

Understanding human mesenchymal stem cell (hMSC) differentiation in three-dimensional matrices *in vitro* is important for potential stem cell therapies and requires that scaffolds correctly display the same adhesive heterogeneity as native extracellular matrix. Here, we report the synthesis and characterization of porous foams prepared by high internal phase emulsion (HIPE) templating using amphiphilic copolymers that act as surfactant during the HIPE process. We combine different copolymers exploiting oil-water interface confined phase separation to engineer the surface topology of foam pores with nanoscopic domains of cell inert and active chemistries mimicking native matrix.

We further demonstrate the control of protein and hMSC adhesion through specific copolymer domains and how these 'patchy' matrices in turn determine hMSC lineage specification.

5.1 Introduction

Human mesenchymal stem cells (hMSCs) are multipotent cells with the capacity to self-renew as well as differentiate into a limited subset of tissue cells. They serve as an autologous source of cells and play an important therapeutic role, which often requires the aid of a construct or scaffold to repair of damaged or diseased tissue. Key scaffold design aspects must mimic native extracellular matrix (ECM) of the body; they must provide both structural support and intrinsic properties to the cell to influence its behavior [1], e.g. topography [2], stiffness [3], and cell binding [4]. These cues show exquisite micro- and nano-scopic organization *in vivo* [4], and in the absence of traditional growth factor cocktails, their spatiotemporal presentation alone can regulate cellular behavior, e.g. adhesion, proliferation, differentiation, and apoptosis [5]. However much of our understanding of stem cell differentiation relies on *in vitro*, two-dimensional studies which could elicit fundamentally different behaviors than physiologically relevant three-dimensional environments [6]. These studies suggest the need for rationally designed biomaterials that present cues in a way that reflects ECM's complexity.

Surface chemistry engineering has dominated recent biomaterials design and shown how specific surface functionalities are cell adhesive, e.g. carboxyl, amine, or hydroxide groups [7]. The topological arrangement of such chemistries has an equally

important effect; the order of nanoscale surface roughness can either maintain hMSC phenotype [8] or direct differentiation [9] depending on its spacing and size. Clustering of these sites into a more mimetic and well-spaced arrangement can alter cell adhesion and spreading [10] but only when sites are adequately spaced to generate forces and further recruit focal adhesion proteins [11]. While these efforts highlight how nano-scale topological properties influence cells, most of these studies have been limited to two-dimensional systems. Three-dimensional scaffolds often present uniform surface chemistry via surface immobilization or direct crosslinking of a binding motif to the scaffold, yielding either homogeneous or protein polymer hydrogels [1]. Often however, these materials have very little control over their surface topology; their topology and the surface motifs they present can also be substantially different from native ECM [4].

Herein we propose the synthesis of a new class of three-dimensional matrices using a 'bottom-up' approach to better mimic the adhesive heterogeneity of matrix and thus direct hMSC differentiation *in vitro*. We propose the combination of high internal phase emulsion (HIPE) templating with interface confined block copolymer self-assembly to engineer 3D porous nano-functionalized materials as scaffolds for cell culture [12,13]. To date, the most utilized HIPE systems are surfactant-stabilized water-in-oil emulsions, where the oil phase consists of polymerizable monomers [14] or block copolymers to polymerize nanostructured materials [15,16] or control cell adhesion [17-19]. Herein, we employ macromolecular surfactants consisting of amphiphilic block copolymers polystyrene-b-poly(ethylene oxide) (PS-PEO) and/or polystyrene-b-poly(acrylic acid) (PS-PAA), which we have previously demonstrated in vesicles undergo interface confined phase separation [20,21] (Fig. 1a), to establish cell adhesive

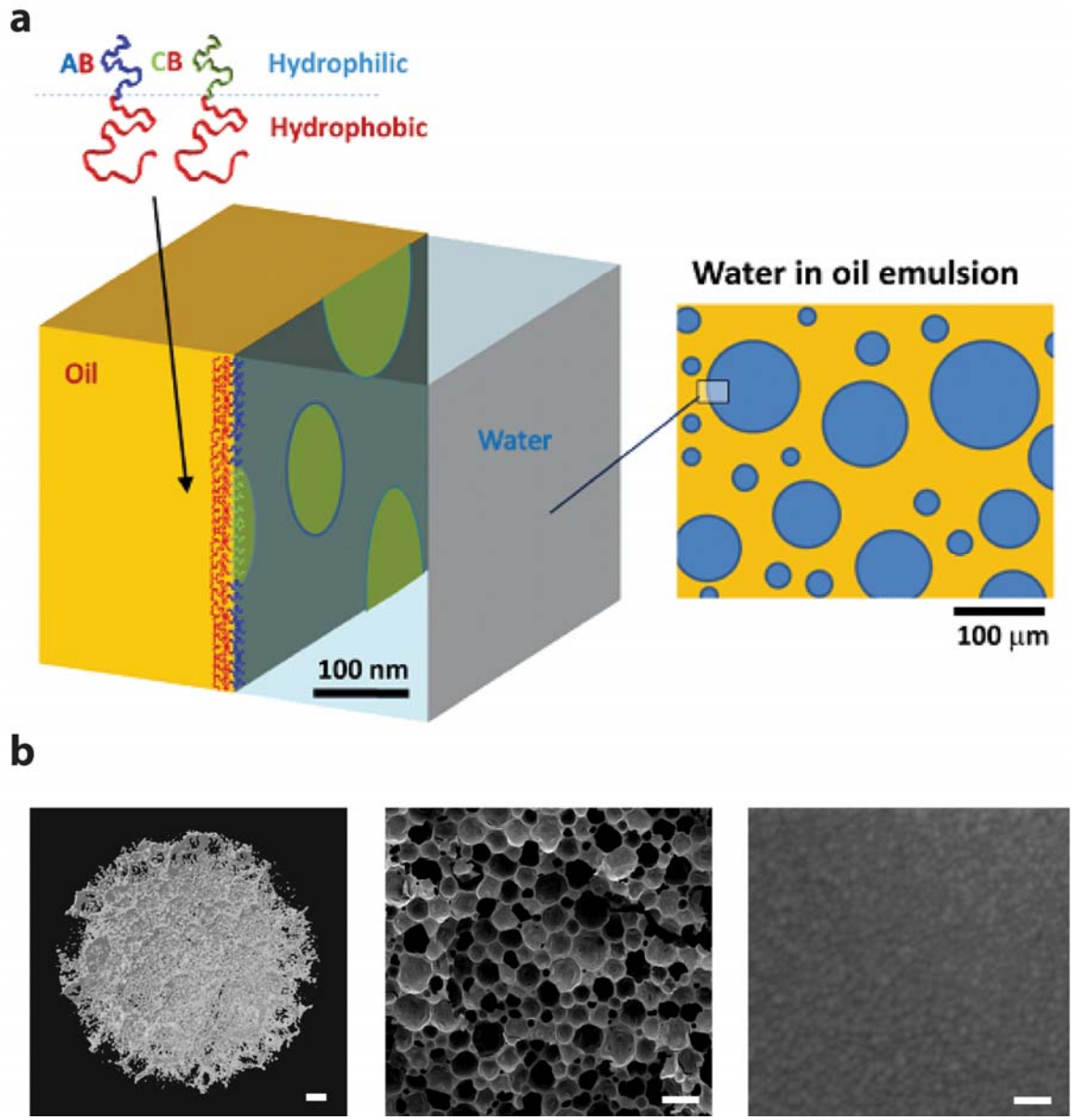

Figure 5.1: HIPE Polymerization Scheme. a) Schematic of high internal phase emulsion templating to form surface cell adhesive and inert domains through amphiphilic block copolymer phase separation at the oil-water interface. b) Macro- and micro-porosity of 3D foams shown by X-ray micro-computational tomography (left) and scanning electron micrographs of the foam (center) and its surface structure (right).

or non-adhesive domains in a scaffold predominantly comprised of PS unlike previous attempts. Due to the high affinity of the polystyrene block with the matrix, subsequent polymerization of the oil phase will ensure anchorage of the copolymers in the scaffold and thereby introduce surface functionality in a 3D foam (Fig. 1b). Stem cells grown on these foams differentiate in a cell source and lineage-dependent manner, indicating the complexity of adhesive heterogeneity as a cue for stem cell differentiation.

5.2 Materials and Methods

5.2.1 Preparation of HIPE matrices

The monomer divinylbenzene (DVB) (80% mixed with m- and *p*-ethyl styrene, Sigma Aldrich) was passed through a basic alumina column (Fluka, Brockmann activity I) to remove the inhibitor; *p*-tert butlycatechol. Potassium persulfate (Sigma Aldrich), polystyrene-b-poly(ethylene oxide) (PS-PEO, Mw= 22500-27500 g/mol, polydispersity index, PDI = 1.1-1.3, Sigma Aldrich), Poly(Styrene)-b-poly(acrylic acid) (PS-PAA, Mw= 8100-8500 g/mol, PDI=1.1-1.3, Sigma Aldrich)) and Span 80 (Sorbitan monooleate, Sigma Aldrich) were all used as received. The monomer: surfactant ratio was maintained at $2.5x10^4$:1 for PS-PAA and PS-PEO. PS-PAA was first dissolved in tetrahydrofuran (10 µl/mg) before solubilizing in the monomer. Emulsions with copolymer mixtures at the indicated molar ratios were prepared (Table 4.1). The aqueous phase, consisting of 0.1 wt/wt % potassium persulfate initiator adjusted to pH 10 with 1M NaOH, was added drop wise to the oil phase (DVB and surfactant) using a peristaltic pump at a rate of 10 ml/min. Once the aqueous phase was added, the resulting emulsion was stirred for 5

minutes to homogenize. The emulsion was polymerized at 60 °C for 24 hours. The resulting foam was then extracted in a soxhlet for 48 hours using a 50/50 v/v% of deionized water / isopropanol.

5.2.2 Protein adsorption and detection on films

Cylindrical foams of ~12 mm in diameter and ~4 mm thick were placed in a 24-well tissue culture plate and submerged in the culture media. After 2 hrs in culture media, foams were rinsed with PBS 3 times. Absorbed protein was dissociated with mRIPA buffer (1% Triton-X, 1% sodium deoxycholate, 0.1% SDS, 10% glycerol, 0.5 mM $MgCl_2$, 150 mM NaCl, 50 mM HEPES pH 7.5) plus the protease inhibitor phenylmethanesulfonylfluoride overnight. Protein concentration within the lysates was measured by the bicinchoninic acid (BCA) assay (Pierce).

Micro- and nano-scale protein clustering was visualized by immunofluorescence and CFSM. 100 μg/ml rat plasma fibronectin in PBS was incubated with film samples for 2 hours at 37°C and washed with PBS. For those samples observed by confocal microscopy, films were incubated with the R457 fibronectin antibody [22,23] in 2% BSA in PBS (1:500) for an hour at 37°C. After rinsing with PBS, samples were incubated with an Alexa Fluor® 647-conjugated secondary antibody in 2% BSA in PBS (1:1000) for an hour at 37°C. A spinning disc confocal fluorescent microscope (BD CARV II, BD Bioscience) and 60X water-immersion objective was used for image acquisition. For those samples observed by CFSM, the R457 fibronectin antibody was bound to an AFM tip using the same chemistry as PLL. All CFSM parameters were described as the same as the previous paragraph. The scan area was set to 2 × 2 μm with 62.5 nm resolution.

The specific interaction between the antibody and fibronectin was identified from the rupture force-loading rate graph, providing the threshold as 300 pN, which we have previously established for fibronectin [24]. Again, area fraction and domain surface areas were determined using ImageJ software.

5.2.3 Cell Culture

Human embryonic stem-mesoderm progenitor (hES-MP) cells (Cellartis, UK) were cultured in basal alpha modified-modified eagle's medium (Gibco, UK) supplemented with 10% FBS, 1% penicillin/streptomycin and 0.25% fungizone and maintained at 37 C and 5% CO_2. Media was replenished every 2-3 days and passaged at 70-80% confluency. Human bone marrow derived- mesenchymal stem cells (hBMSC) (Lonza) were cultured in growth media (20% fetal bovine serum, 79% Dulbecco's Minimum Eagle's Media, and 1% Penicillin-Streptomycin. Passages between 5-10 were used for all experiments and all cell sources.

5.2.4 MTS assay

Cell viability was examined by the MTS assay on both the hES-MP cells and hBMSC cultured on scaffolds for 7 days. Experiments were carried out in triplicate. Growth media was removed and treated with 600 μl of MTS/PMS solution (Promega, UK) in culture medium at the final concentration of 333 μg/ml and 25 μM respectively were added to each well. Cells were then incubated for 3 hours at 37^{o}C to let the substrate react with the dehydrogenase enzyme present in mitochondria. 100 μl of the resulting solution was transferred to flat-bottomed 96-well plates in duplicate and the absorbance

was measured at 490 nm. Number of viable cells on the scaffolds was calculated from a calibration curve using cell densities ranging from 0 to $2.5x10^4$ cells. Student's t-test was performed to check for statistical differences in viability across the different surface chemistries.

5.2.5 DAPI and Texas Red Phalloidin Staining

hES-MP and hBMSCs cells were cultured on the foams for 7 days. Scaffolds were washed with PBS, fixed in 3.7% paraformaldehyde for 30 min, washed with PBS twice before 0.2% Triton-X100 was added to each scaffold for 15 minutes. Scaffolds were washed with PBS twice and then incubated in Texas Red- or Rhodamine-labeled phalloidin and 4',6-diamidino-2-phenylindole (DAPI) in PBS (Invitrogen) at room temperature for 1 hour before washing again in PBS. Scaffolds were mounted and visualized under either an inverted Zeiss LSM 510 META confocal laser-scanning or BD CARV II spinning disc confocal fluorescent microscope using 10x objective lenses, respectively. Microscopy was performed in a sequential multiple channel fluorescence scanning mode. The polystyrene-based foams were auto-fluorescent at 488 nm in the green channel. Image analysis was performed with NIH ImageJ software.

5.2.6 Vinculin Expression

hBMSCs were lysated by mRIPA buffer and their proteins separated electrophoretically. After transferring the proteins onto a nitrocellulose membrane, the membrane was blocked using a 2% BSA solution in PBS and subsequently incubated with a primary antibody for vinculin (1:1000, Abcam) followed by an HRP-conjugated

secondary antibody (Biorad). Protein signal was detected via chemiluminescence on X-ray film.

5.2.7 Gene expression

Total RNA was isolated from 7 day hES-MP and hBMSC culture using Trizol® reagent (Introvigen). Reverse transcription was applied using 2-5 μg total RNA to obtain cDNA for real time-quantitative PCR. A customized Low density Taqman array (Applied Biosystems; for genes, see Supplemental Tables D1, D2) was used to detect gene expression analyzed by the relative quantification $2^{-\Delta\Delta CT}$ method [25]. Gene expression was expressed as a fold change of the cells cultured in each foam versus those undifferentiated cells maintained on tissue culture plastic plates.

5.3 Results

5.3.1 Surface chemistry modification of foams

HIPEs were produced using combinations of PS-PEO and PS-PAA reported in Table 1. Note that foams will be referred to by their PEO content, e.g. 25% PEO will be PEO25, except for pure PS-PAA, which will be referred to as PAA100. As shown in Fig. 1, emulsion templating allows foam porosity to be controlled by droplet interaction. Scanning electron microscopy (SEM) confirmed that all foams contain microscopic porosity regardless of polymer composition (Figure 5.2a, left). While void distribution is polydisperse, no significant differences in void diameters were observed amongst mixed formulations. Similarly higher resolution SEM images showed that foam composition

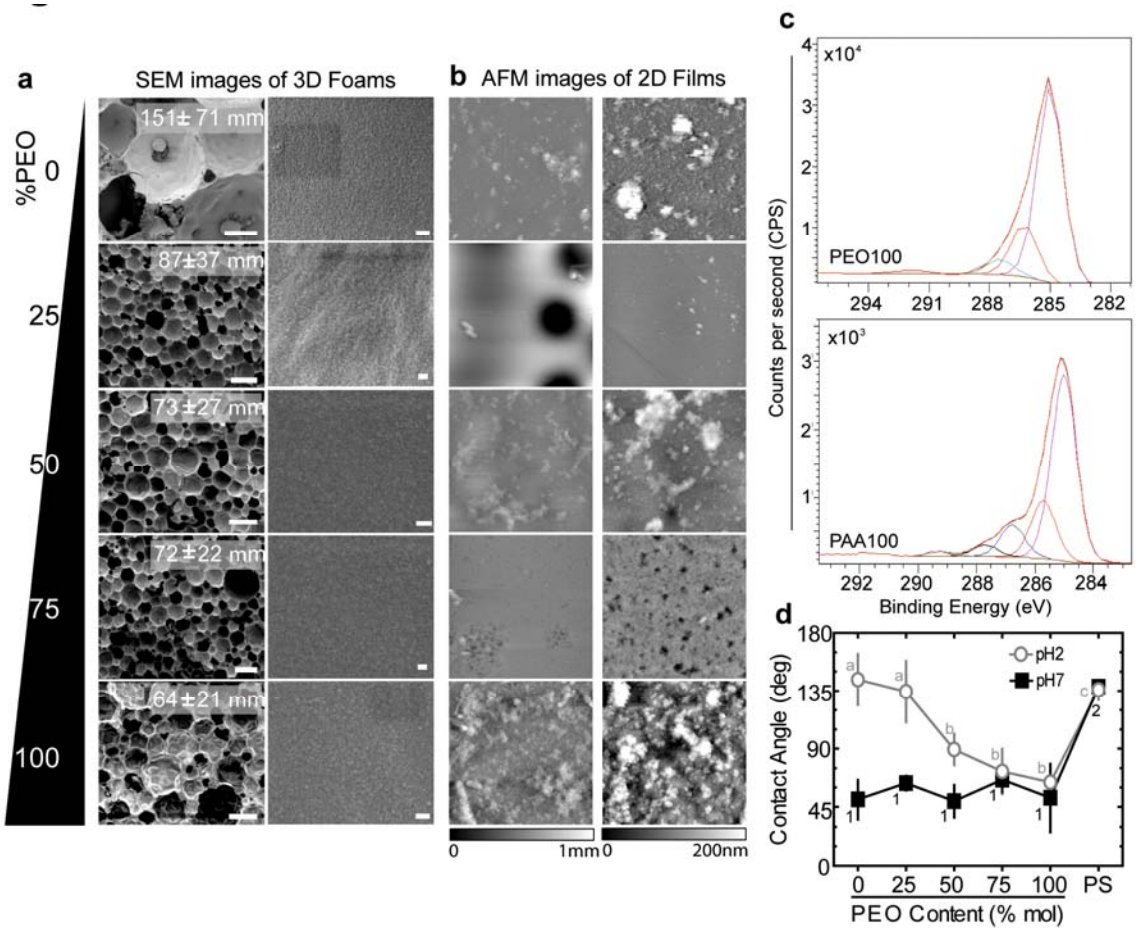

Figure 5.2: Morphologies of Porous Foams and Films. a) Scanning electron micrographs of the HIPE foams showing microscale void diameters (mean ± SD; left) and higher magnification images to illustrate surface roughness (right). Scale bars are 100 μm (left) and 100 nm (right). b) AFM topographs of films from 20 x 20 (left) and 2 x 2 μm scans (right). Image colormap ranges are 0 – 1 μm and 0 – 200 nm. c) X-ray photoelectron spectra of foams containing only polystyrene-b-poly(ethylene oxide) or polystyrene-b-poly(acrylic acid) copolymers, i.e. PEO100 and PAA100, respectively. d) Average contact angles of pH 2 (open circles) and pH 7 (closed squares) deionized water on 3D foams as a function of the molar ratio of polystyrene-b-poly(ethylene oxide). Mean comparisons of one group versus all samples have the same symbol, e.g. 1, 2, a, b and c. 1p < 0.05 from pure polystyrene foams. 2p < 0.05 from all other foams at pH 7. ap < 0.05 from other mixed composition foams but not polystyrene. bp < 0.05 from other copolymer-containing and pure polystyrene foams. cp < 0.05 from mixed composition foams PEO50 through PEO100.

had no qualitative effect on void surface roughness (Figure 5.2a, right; Supplementary Figure D.1a), allowing any biological response to be compared across the different matrices without bias. For quantitative comparisons of surface morphology, film analogues were synthesized and, when interrogated by atomic force microscopy (AFM), mixtures were found to structurally resemble the foam surface topography regardless of scan size (Figure 5.2b); maximal height variation was sub-micron for all compositions, though average surface roughness for single copolymer substrates was slightly higher (Supplemental Figure C.1a). However, roughness differences between formulations are less than those previously described to influence differentiation [2].

5.3.1 Surface chemistry and topology effects on hMSC responses

Having characterized its surface chemistry and topology from chapter 4, how specific surface structures associate with biological function was investigated next. Adhesion and viability was analyzed for two separate sources of hMSCs: human embryonic stem cell derived mesoderm progenitors (hES-MP) and primary human bone marrow derived mesenchymal cells (hBMSC), both which differentiate towards the adipogenic, myogenic and osteogenic lineages [26,27]. hES-MP and hBMSC viability was measured after a period of 7 days (Figure 5.3b). It is important to note that hES-MP viability differences were minimal, indicating little if any scaffold toxicity (Supplemental Figure D.1), and thus cell adhesion differences occurred as a response to the surface chemistry. hES-MP and hMSC adhesion and spreading were poor on PEO100 foams (Figure 5.3a), which is not surprising given PEO's non-fouling and biologically inert properties [28]. Interestingly, poor cell adhesion was also seen on 'sticky' PAA100

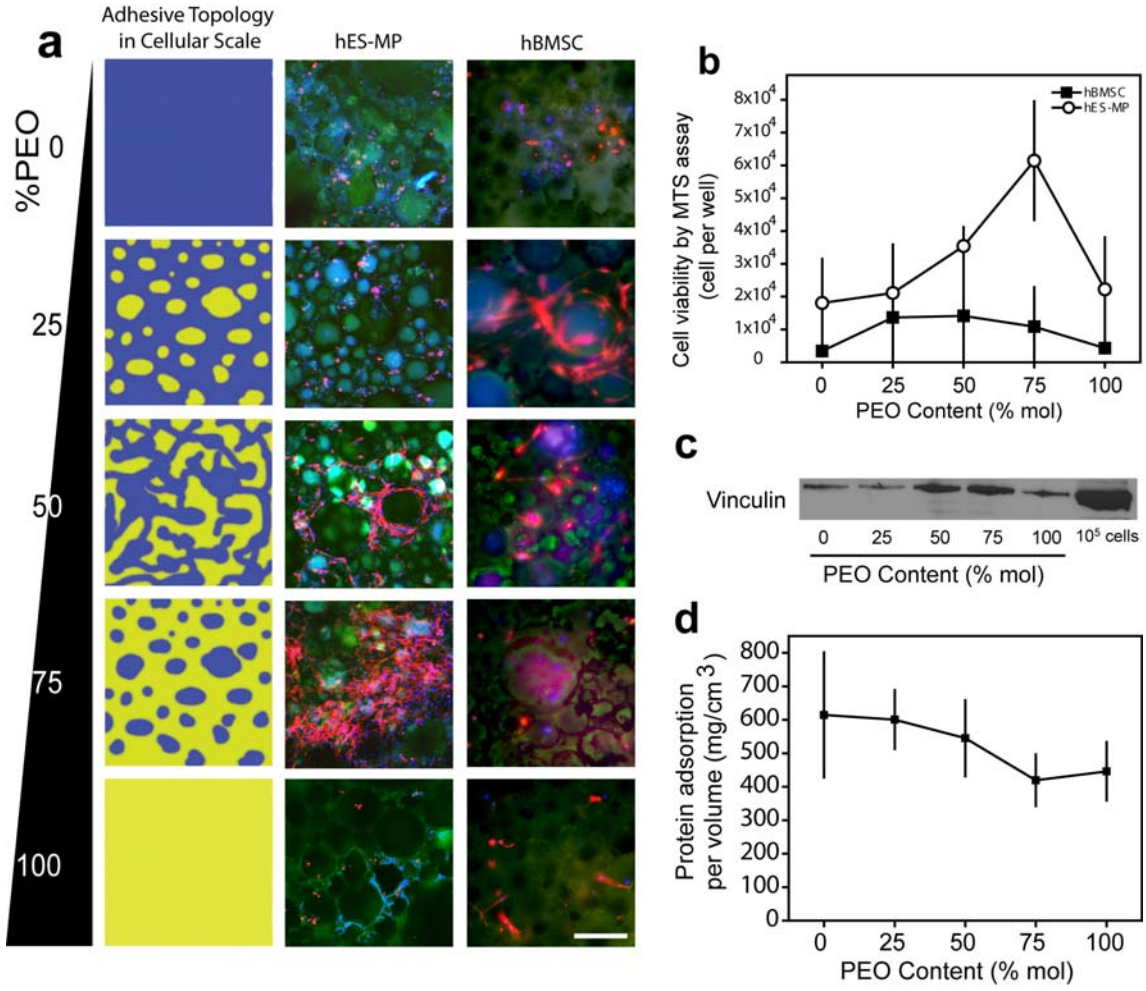

Figure 5.3: Cell viability and protein adsorption on HIPE scaffolds. a) Ideal phase separations of PS-PAA (blue regions) and PS-PEO (yellow regions) are shown as a function of PS-PEO content. Images of nuclear (blue) and filamentous actin (red) staining of hES-MPs (middle) and hBMSCs (right) cultured for 7 days on the foams show varying cell attachment and spreading with changing PS-PEO molar ratio. Note that polystyrene within the scaffolds auto-fluoresces in the green color channel. b) Average cell number examined by an MTS assay on hES-MP (open circles) and hBMSCs (closed rectangles) cultured for 7 days on the 3D foams and plotted versus PS-PEO molar percent. c) Western blot of vinculin from hBMSCs on foams shown as a function of PS-PEO molar ratio as well as hBMSCs cultured on tissue culture plastic as a control. d) Average total protein adsorption per foam volume.

foams, where the highest cell viability and adhesion would be expected. Instead, cell spreading was highest for hES-MPs on PEO75 foams. hBMSCs, on the other hand, preferred foams with copolymer mixtures but not any one specific formulation (Fig 5.3b). However, immunoblotting for the focal adhesion protein vinculin in hBMSCs revealed higher expression for cells bound to 'patchy' compositions, i.e. PEO50 and PEO75 foams (Figure 5.3c). Together these data would indicate that while hES-MPs adhere in a composition-dependent matter, those hBMSCs that bind to the foams are well attached.

We next sought to ask "why cells preferentially adhered to certain surface patterns over others?" The answer may rest with which PEO/PAA mixture most closely mimics the natural adhesive heterogeneity of extracellular matrix, providing the appropriate spatial distribution of cell binding and cell inert domains [4]. First, protein adsorption from serum-containing media was measured, but no statistical difference was found in the quantity of serum proteins adsorbed for any foam composition (Figure 5.3d). While total protein adsorption may not determine how 'adhesive' a specific copolymer composition is to cells, how such proteins might cluster due to specific surface chemistry may correlate with cell adhesion and ultimately behaviour. In fact when fibronectin binding to films of PEO75 and PEO25 was examined by confocal microscopy (Figure 5.4a) and CFSM (Figure 5.4b), fibronectin clustering was found to be surface chemistry-dependant (white regions, Figure 5.4b); the changes in fibronectin's distribution on the surface (Figure 5.4c) was found to correspond with area fraction changes previously seen with PAA, where protein adsorption should occur due to its opposing charge. Fibronectin bound to PEO75 substrates aggregated into 0.13 μm^2 domains spaced at least 0.52 μm apart (Figure 5.4d), reflecting the smaller adhesive domains of PAA on PEO75

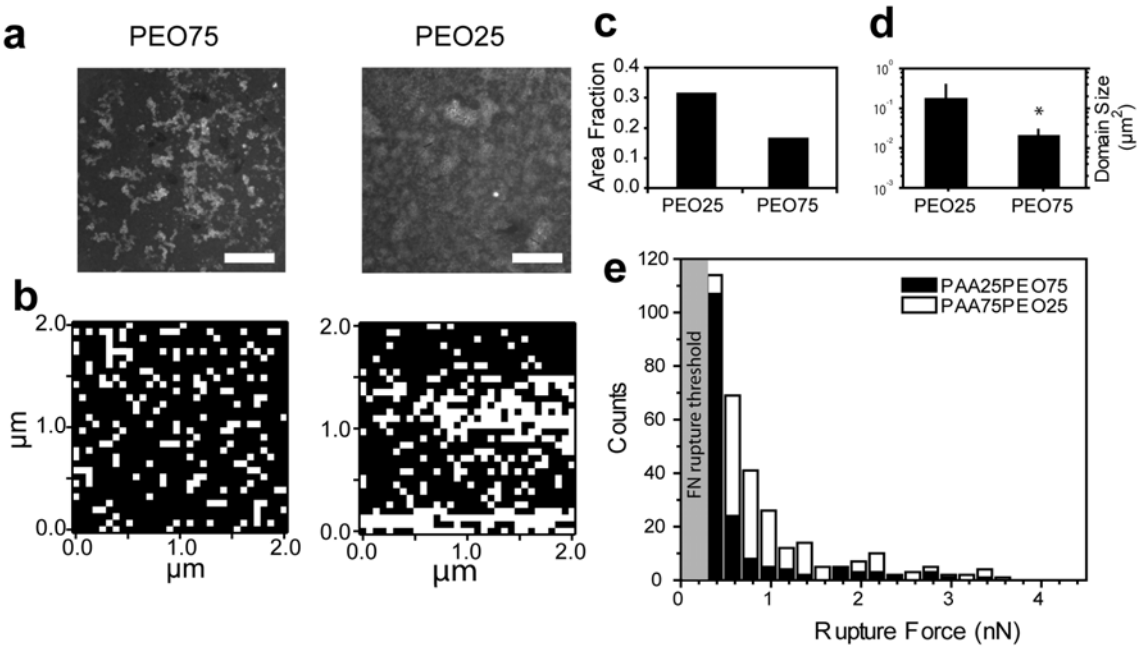

Figure 5.4: Protein adsorption in cellular scale. e) Immunofluorescent staining of fibronectin adsorbed on PEO75 (left) and PEO25 (right) films. Brighter regions represent immobilized fibronectin on the surface. f) Fibronectin adsorption on PEO75 (left) and PEO25 (right) films detected by CFSM over a 2 x 2 μm scan size. White regions represent immobilized fibronectin on the surface. g) Area fraction of fibronectin adsorption evaluated from CFSM images for foams of indicated PS-PEO content. h) Average fibronectin domain size determined from CFSM images corresponding to the indicated PS-PEO content. *$p<0.01$. i) Rupture force distribution of the fibronectin-antibody interaction ($F_{threshold}$ =300 pN; grey shaded region) from fibronectin immobilized on PEO25 (open bar) and PEO75 (closed bar) films.

substrate's surface. On the other hand, larger adhesive domains spaced much closer together in PEO25 approached the scan size limit (Figure 5.4d) and equated to 50% more rupture events on PEO25 than PEO75 (Figure 5.4e), together implying a more uniform protein coating. Thus it would appear that preferential cell adhesion is likely due to protein surface clustering.

5.3.2 Surface chemistry and topology effects on hMSC fate

To better understand how copolymer composition could influence hES-MP and hBMSC fate, cells were seeded onto foams for 7 days and characterized for their expression of specific lineage markers for known mesenchymal phenotypes in the absence of soluble induction factors [3,29]. Little difference was observed in genes specific for the mesenchymal compartment for either cell source (Figure 5.5, MSC; Supplemental Tables D1, D2). For hBMSCs, no discernable differentiation trend was observed for more contractile lineages, e.g. myogenic and osteogenic differentiation (Figure 5.5, Myo and Osteo). However, hBMSC adipogenic genes globally were upregulated in a domain-dependent matter; highest adipogenic expression occurred on PEO50 to PEO100 foams (Figure 5.5, Adipo). hBMSCs at these compositions do not spread well (Figure 5.3a) but remain adherent (Figure 5.3b), consistent with previous reports of adipogenesis in poorly spread, less contractile hBMSCs [29]. Volcano plots indicating statistically different and highly changing hBMSC genes versus undifferentiated cells, i.e. $p < 0.1$ and a greater than 100% change in expression (Supplemental Figure D.2, bottom; Supplemental Tables D4, D6), show that most genes meeting these criteria are contractile genes that decrease in expression, again consistent

Figure 5.5: Gene expression of hES-MPs and hBMSCs cultured on foams for 7 days. Heat maps of hES-MPs (a) and hBMSCs (d) were separated by genotypic expression of mesenchymal, adipogenic, myogenic and osteogenic expressions (from top to bottom). Colour bar represents down- (green) and up-regulation (red) relative to undifferentiated cells from the same source. Columns within each heat map represent cell responses on scaffold of 0 - 100 mole percent of PEO (left to right). Heat map rows represent individual genes, which are listed at right. The average log base-2 fold change for hES-MPs (b) and hBMSCs (c) are also shown as a function of the mole percent of PEO for genes of each lineage.

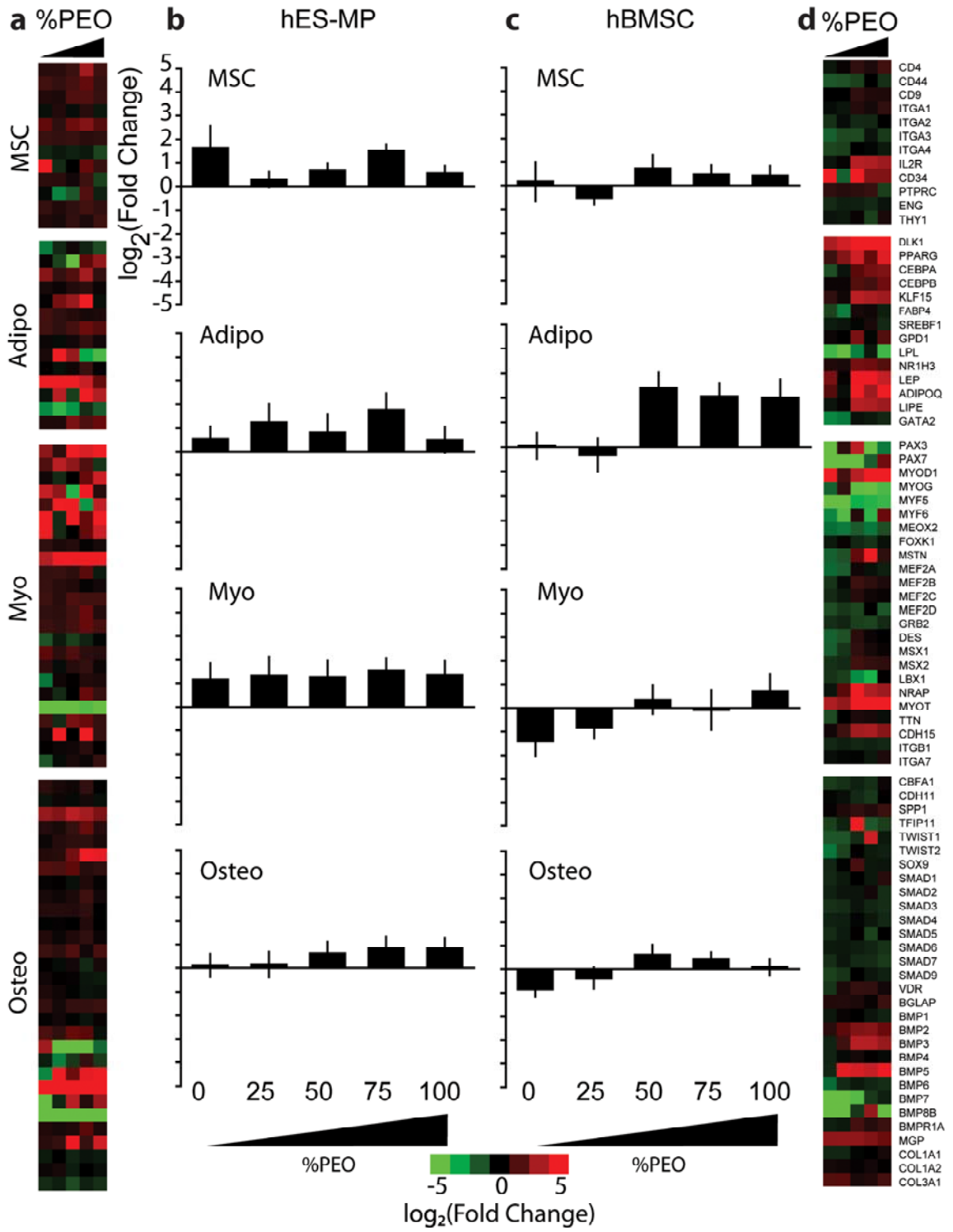
a %PEO
b hES-MP
c hBMSC
d %PEO
MSC
Adipo
Myo
Osteo
log2(Fold Change)
5
4
3
2
1
0
-1
-2
-3
-4
-5
0
25
50
75
100
%PEO
%PEO
-5
0
5
log2(Fold Change)
CD4
CD44
CD9
ITGA1
ITGA2
ITGA3
ITGA4
IL2R
CD34
PTPRC
ENG
THY1
DLK1
PPARG
CEBPA
CEBPB
KLF15
FABP4
SREBF1
GPD1
LPL
NR1H3
LEP
ADIPOQ
LIPE
GATA2
PAX3
PAX7
MYOD1
MYOG
MYF5
MYF6
MEOX2
FOXK1
MSTN
MEF2A
MEF2B
MEF2C
MEF2D
GRB2
DES
MSX1
MSX2
LBX1
NRAP
MYOT
TTN
CDH15
ITGB1
ITGA7
CBFA1
CDH11
SPP1
TFIP11
TWIST1
TWIST2
SOX9
SMAD1
SMAD2
SMAD3
SMAD4
SMAD5
SMAD6
SMAD7
SMAD9
VDR
BGLAP
BMP1
BMP2
BMP3
BMP4
BMP5
BMP6
BMP7
BMP8B
BMPR1A
MGP
COL1A1
COL1A2
COL3A1

with a composition-dependent preference for less contractile adipocytes. hES-MPs had divergent behavior from hBMSCs in that they were well spread (Figure 5.3a) and showed their greatest change with myogenesis, albeit in a domain-independent manner (Figure 5.5, Myo). Interestingly enough, osteogenic genes were also upregulated but in a domain-dependent manner (Figure 5.5, Osteo). Volcano plots indicated that genes in hES-MPs that were highly significantly different from undifferentiated and also highly upregulated were clustered in the myogenic and osteogenic lineages. Few adipogenic genes exhibited the same pattern (Supplemental Figure D.2, top; Supplemental Tables D3, D5), consistent with a lack of global adipogenic differentiation (Figure 5.5, Adipo).

5.4 Discussions

Together these data generate 3D matrices using a strategy that exploits macromolecular self-assembly and creates chemically and topologically defined surfaces that illustrate how scaffold patterns can control protein adsorption and thus cell adhesion in a way that better reflects natural differences in matrix properties. Other systems, which employ spatially patterned ligands in 2D [17-19,30], have shown differential cell adhesion, spreading, and migration, but here using interface-confined phase separation of adhesive domains in a 3D scaffold, we show that such control ultimately affects stem cell differentiation in a way that appears cell source-dependent.

5.4.1 HIPE template as a scaffold template

A HIPE template provides highly tunable physical and chemical characteristics suitable for cell growth and proliferation, e.g. pore size, surface roughness, surface

chemistry, etc. Scaffold pore size for rigid scaffolds typically ranges from 100 to 600 μm to maintain adequate cell infiltration [31,32]; natural biomaterials such as collagen gels sustain excellent cell adhesion and proliferation despite pore sizes of less than 100 μm [33]. Depending on emulsion parameters, HIPE scaffolds here provided pore sizes between 40 and 120 μm while maintaining sufficient adhesion and infiltration. With porosity much closer to natural matrices, this suggests that as was observed in 2D [18,30], adhesive domains may in fact encourage migration into the scaffold despite lower pore interconnectivity. HIPE templates–especially when composed of a mixture of copolymers as they were here–have surfaces with a roughness ranging between 10 and 70 nm. Previous reports using roughened surfaces from e-beam lithography show that substrates with features in excess of 100 nm promote cell adhesion [34] and differentiation [35]. Roughness most likely induces integrin clustering to some degree with those substrates. However scaffold surface roughness was less than 100 nm and relatively composition-independent, indicating that it is not likely to differentially influence stem cell fate. Clustering induced by other HIPE properties, e.g. adhesive domains, may account for the cell and focal adhesion assembly differences observed between the two cell sources here, and this could ultimately affect differentiation.

Most scaffolds with homogeneous surface chemistry do not recapitulate the heterogeneous adhesivity of natural matrix [4]. More recently, spatially controlled surface chemistries have been used to better understand how adhesion formation and even differentiation are affected by heterogeneously distributed adhesions in 2D. RGD peptides spaced at small intervals (< 50 nm) favor mature adhesions [18,30], spread cells [19], and osteogenesis [17], whereas larger intervals (> 50 nm) appear to favor an

adipogenic fate [17] resulting from dynamic adhesions in less spread cells [30]. Given that the link between cell spreading, shape, and fate is due to differences in membrane tension [36,37], differentiation control by heterogeneous adhesion sites in 2D would appear to have mechanical origins. Scaffold adhesive spots detected by CFSM here were 10-fold larger than the largest domains previously reported, and thus they may support fundamentally different types of adhesions. However despite this size difference, which may simply be due to detection methods [18,38], hBMSC adipogenesis also correlated with greater adhesive site spacing, i.e. cells were more adipogenic on scaffolds containing well-spaced PS-PAA domains. Interestingly, hES-MPs exhibited opposing behavior, with osteogenesis favored on the same scaffolds. On the other hand, micron-sized pillars arrays also provide discrete adhesion sites to cells [39], but cell behavior remains largely unchanged versus continuous surfaces [40]. However, focal adhesion assembly between these substrates is also qualitatively similar; thus differences observed here with HIPE scaffolds containing well-spaced PS-PAA domains versus conventional substrates are most likely the result of adhesive domains reflecting a length scale more representative of heterogeneously adhesive matrix [4,5].

5.4.2 Differential stem cell differentiation in response to nano-domains

hBMSC differentiation depends on Rho-ROCK-induced contractility [3,36,37] but ultimately relies on sufficient cell adhesion in order to pull against the matrix [36]. The disparate adhesive behavior and ultimately differentiation responses of hBMSCs and hES-MPs observed here provides additional evidence that cell source, even between cells of the same lineage, i.e. mesenchymal stem cells and their progenitors, respectively, can

influence how cells respond to stimuli. For example, hBMSCs and human adipose-derived stem cells (hASCs), which share a common background ($CD34^{-}CD45^{-}CD90^{+}CD105^{+}$) [27,41], respond differently to matrix stiffness as hASCs undergo near-complete differentiation while hBMSCs remain differentiated but somewhat 'plastic [41].' Though methylation states for adult stem cells and their progenitors remain similar [42], using difference cell sources for the same lineage here may have contributed to difference epigenetic signatures [43] and thus differential responses to adhesive nano-domains.

Underlying these observations, however, was composition-independent upregulation of myogenic signals in hES-MPs. While this may further emphasize stem cell source differences, it more likely highlights the influence of other scaffold parameters, e.g. stiffness. However, copolymer composition does not influence scaffold stiffness, and such properties likely cause the composition-independent differentiation noted here. Changing stiffness by divinyl benzene crosslinking should modulate stiffness which would enable one to induce other lineages in a stiffness-dependent fashion [3].

5.5 Conclusion

Together these data show a simple and cost effective method to generate three-dimensional matrices using a strategy that exploits macromolecular self-assembly. This process results in chemically and topologically defined surfaces that control hMSC adhesion and differentiation. The work described here illustrates how topological patterns in a scaffold can control protein adsorption and thus cell adhesion in a way that better

reflects the natural differences in matrix properties. While the work describes adsorbed protein on an electrostatically charged foam, the results suggest that chemistries with tailored presentation of specific cell recognition peptides, e.g. RGD, could more directly regulate cell-matrix interactions and mimic matrix even better than these PEO/PAA foams. This work also uses a rigid polystyrene backbone, but as shown with hydrogels, controlling mechanical properties is critically important [3]; changing the oil phase monomers to viscoelastic ethylhexyl acrylate or methacrylate [44] or to biodegradable polycaprolactone [45] and poly(lactic acid) [46], all of which have been previously used in the HIPE process, could further make these foams more clinically translatable. Finally, these investigations occurred over one week and were sufficient for cell differentiation, but current HIPE scaffolds may lack sufficient interconnectivity to support cell growth over longer time periods relevant for tissue engineering and regenerative medicine. Regardless of potential modifications, these data show that with careful choice of block copolymer mixtures, HIPE scaffolds can provide a three-dimensional matrix that presents a cue, adhesive heterogeneity, which can direct stem cell differentiation in the absence of specific growth factors.

5.6 Acknowledgement

In chapter 4 and 5, the manuscript has been submitted. The dissertation author is the co-primary author with Priyalakshmi Viswanathan and thanks co-authors Kamolchanok Ngamkham and Dr. Giuseppe Battaglia. The author also thanks Dr. Gwendolen Reilly (University of Sheffield) for fruitful discussions, Dr. Nicholas Geisse

(Asylum Research; Santa Barbara, CA) for technical support, and Dr. Adrian Boatwright (University of Nottingham) for XPS assistance. This work was supported by grants from the National Institutes of Health (1DP02OD006460 to Dr. Adam J. Engler), Human Frontiers Science Program (RGY0064/2010 to Dr. Adam J. Engler and Dr. Guiseppe Battaglia), and the Engineering and Physical Sciences Research Council (EP/F019750/1). Pre-doctoral fellowship support was also provided by the Royal Thai Government Science and Technology (to Somyot Chirasatitsin).

5.7 References

1 Lutolf, M.P. and Hubbell, J.A. (2005) Synthetic biomaterials as instructive extracellular microenvironments for morphogenesis in tissue engineering. *Nature biotechnology* 23 (1), 47-55

2 Dalby, M.J. et al. (2007) The control of human mesenchymal cell differentiation using nanoscale symmetry and disorder. *Nat Mater* 6 (12), 997-1003

3 Engler, A.J. et al. (2006) Matrix elasticity directs stem cell lineage specification. *Cell* 126 (4), 677-689

4 Reilly, G.C. and Engler, A.J. (2010) Intrinsic extracellular matrix properties regulate stem cell differentiation. *J Biomech* 43 (1), 55-62

5 Hay, E.D. (1991) *Cell biology of extracellular matrix*, Plenum Press

6 Cukierman, E. et al. (2001) Taking cell-matrix adhesions to the third dimension. *Science* 294 (5547), 1708-1712.

7 Curran, J.M. et al. (2006) The guidance of human mesenchymal stem cell differentiation in vitro by controlled modifications to the cell substrate. *Biomaterials* 27 (27), 4783-4793

8 McMurray, R.J. et al. (2011) Nanoscale surfaces for the long-term maintenance of mesenchymal stem cell phenotype and multipotency. *Nature materials* 10 (8), 637-644

9 Dalby, M.J. et al. (2007) The control of human mesenchymal cell differentiation using nanoscale symmetry and disorder. *Nature materials* 6 (12), 997-1003

10 Arnold, M. et al. (2004) Activation of integrin function by nanopatterned adhesive interfaces. *Chemphyschem : a European journal of chemical physics and physical chemistry* 5 (3), 383-388

11 Galbraith, C.G. et al. (2002) The relationship between force and focal complex development. *J Cell Biol* 159 (4), 695-705

12 Bokhari, M. et al. (2007) Novel cell culture device enabling three-dimensional cell growth and improved cell function. *Biochemical and biophysical research communications* 354 (4), 1095-1100

13 Bokhari, M. et al. (2007) Emulsion-templated porous polymers as scaffolds for three-dimensional cell culture: effect of synthesis parameters on scaffold formation and homogeneity. *Journal of Materials Chemistry* 17, 4088-4094

14 Carnachan, R. et al. (2006) Tailoring the morphology of emulsion-templated porous polymers. *Soft Matter* 2, 608-616

15 Hamley, I.W. (2003) Nanostructure fabrication using block copolymers. *Nanotechnology* 14 (10), R39

16 Smart, T. et al. (2008) Block copolymer nanostructures. *Nano Today* 3 (3-4), 38-46

17 Frith, J.E. et al. (2012) Lateral spacing of adhesion peptides influences human mesenchymal stem cell behaviour. *J Cell Sci*

18 George, P.A. et al. (2009) Self-assembling polystyrene-block-poly(ethylene oxide) copolymer surface coatings: Resistance to protein and cell adhesion. *Biomaterials* 30 (13), 2449-2456

19 George, P.A. et al. (2010) Hierarchical scaffolds via combined macro- and micro-phase separation. *Biomaterials* 31 (4), 641-647

20 Battaglia, G. et al. (2011) Wet nanoscale imaging and testing of polymersomes. *Small* 7 (14), 2010-2015

21 LoPresti, C. et al. (2011) Controlling polymersome surface topology at the nanoscale by membrane confined polymer/polymer phase separation. *Acs Nano* 5 (3), 1775-1784

22 Aguirre, K.M. et al. (1994) Fibronectin self-association is mediated by complementary sites within the amino-terminal one-third of the molecule. *Journal of Biological Chemistry* 269 (45), 27863-27868

23 Sechler, J.L. et al. (2001) A novel fibronectin binding site required for fibronectin fibril growth during matrix assembly. *The Journal of Cell Biology* 154 (5), 1081-1088

24 Chirasatitsin, S. and Engler, A.J. (2010) Detecting cell-adhesive sites in extracellular matrix using force spectroscopy mapping. *Journal of Physics: Condensed Matter* 22 (19), 194102

25 Livak, K.J. and Schmittgen, T.D. (2001) Analysis of Relative Gene Expression Data Using Real-Time Quantitative PCR and the 2âˆ’Î”Î”CT Method. *Methods* 25 (4), 402-408

26 Peppo, G.M.D. et al. (2005) Human Embryonic Mesodermal Progenitors Highly Resemble Human Mesenchymal Stem Cells and Display High Potential for Tissue Engineering Applications. *Tissue Engineering: Part A* 16 (7), 2161-2182

27 Pittenger, M.F. et al. (1999) Multilineage potential of adult human mesenchymal stem cells. *Science* 284 (5411), 143-147

28 Liu, S.Q. et al. (2009) Synthetic hydrogels for controlled stem cell differentiation. *Soft Matter* 6, 67-81

29 McBeath, R. et al. (2004) Cell shape, cytoskeletal tension, and RhoA regulate stem cell lineage commitment. *Developmental cell* 6 (4), 483-495

30 Cavalcanti-Adam, E.A. et al. (2007) Cell spreading and focal adhesion dynamics are regulated by spacing of integrin ligands. *Biophys J* 92 (8), 2964-2974

31 Hollister, S.J. (2005) Porous scaffold design for tissue engineering. *Nat Mater* 4 (7), 518-524

32 Karageorgiou, V. and Kaplan, D. (2005) Porosity of 3D biomaterial scaffolds and osteogenesis. *Biomaterials* 26 (27), 5474-5491

33 Nehrer, S. et al. (1997) Matrix collagen type and pore size influence behaviour of seeded canine chondrocytes. *Biomaterials* 18 (11), 769-776

34 Dalby, M.J. et al. (2002) Increasing Fibroblast Response to Materials Using Nanotopography: Morphological and Genetic Measurements of Cell Response to 13-nm-High Polymer Demixed Islands. *Experimental Cell Research* 276 (1), 1-9

35 Dalby, M.J. et al. (2007) The control of human mesenchymal cell differentiation using nanoscale symmetry and disorder. *Nat Mater* 6 (12), 997-1003

36 McBeath, R. et al. (2004) Cell Shape, Cytoskeletal Tension, and RhoA Regulate Stem Cell Lineage Commitment. *Developmental Cell* 6 (4), 483-495

37 Kilian, K.A. et al. (2010) Geometric cues for directing the differentiation of mesenchymal stem cells. *Proc Natl Acad Sci U S A* 107 (11), 4872-4877

38 Chirasatitsin, S. and Engler, A.J. (2010) Detecting cell-adhesive sites in extracellular matrix using force spectroscopy mapping. *Journal of Physics-Condensed Matter* 22 (19), 194102

39 Tan, J.L. et al. (2003) Cells lying on a bed of microneedles: an approach to isolate mechanical force. *Proc Natl Acad Sci U S A* 100 (4), 1484-1489

40 Oliver, T. et al. (1995) Traction forces in locomoting cells. *Cell Motil Cytoskeleton* 31 (3), 225-240

41 Choi, Y.S. et al. (2012) Mechanical derivation of functional myotubes from adipose-derived stem cells. *Biomaterials* 33 (8), 2482-2491

42 Sorensen, A.L. et al. (2010) Promoter DNA methylation patterns of differentiated cells are largely programmed at the progenitor stage. *Mol Biol Cell* 21 (12), 2066-2077

43 Noer, A. et al. (2006) Stable CpG hypomethylation of adipogenic promoters in freshly isolated, cultured, and differentiated mesenchymal stem cells from adipose tissue. *Mol Biol Cell* 17 (8), 3543-3556

44 Cameron, N.C. and D.C.Sherringdon. (1997) Preparation and glass transition temperature of elastomeric polyHIPE materials. *J. Mater. Chem* 7 (11), 2209-2212

45 Lumelsky, Y. and Silverstein, M.S. (2009) Biodegradable Porous Polymers through Emulsion Templating. *Macromolecules* 42 (5), 1627-1633

46 Busby, W. et al. (2002) Tissue engineering matrices by emulsion templating. *Polymer International* 51, 871-881

Chapter 6

Conclusion

Understanding stem cell differentiation will greatly further its use in regenerative applications. An adherent stem cell such as a mesenchymal stem cell (MSC) is one of most promising cell sources for stem cell-based therapy, whether derived from bone marrow, adipose, etc., as it is multipotent [1], adherent and responsive to the properties of its niche [2], and thought to be immune privileged [ref]. Given these requirements and benefits of MSCs versus other stem cell types, a common strategy for regeneration has been to provide MSCs with substrates that are capable of guiding their differentiation but which also support cell adhesion. As shown in Chapter 1, the spatial organization of such adhesion sites is often inappropriately arranged, and the goal of this thesis was to develop techniques and materials to make and characterize materials that could display adhesive heterogeneity. Through model materials, the fidelity of high resolution spatial mapping via atomic force microscopy (AFM) in chapters 2 and 3 and the application of those methods in chapters 4 and 5 to a foam scaffold and stem cells was tested. As a final summary, the accomplishments of the work presented in this thesis, the need for the

improved AFM detection methods used here, e.g. force spectroscopy mapping (FSM), and its application to stem cell biomaterials will be outlined here.

First it is necessary to comment on the technical improvements in imaging required for subsequent chapters of this thesis. By using a typical light microscope, spatial information is limited by the wavelength of light sources. FSM is a solution to overcome the scale limitation down to tens of nanometers, given that its resolution is only limited by the quality of the fabrication methods available, which currently can create nanometer-sized AFM probes. The raw force curve data from FSM includes both approach and retrace curves corresponding to positions of indentation, which enabled two modes of imaging shown in chapters 2 and 3. From an approach curve, a physical property such as elasticity, i.e. the compliance of material resisting to forces, can be obtained from FSM, which referred to in this thesis as mechanical FSM (MFSM), by mapping the elastic modulus of each indentation back to its position within a regular array of positions over an area of interest. While this method can provide a wealth of information for the user, there are certainly some limitations discussed in the chapter but which deserve a mention here. For instance, depth-dependent elastic moduli were not calculated here, but further refinement of the technique and use of linear transform analysis method that has been recently published [3] should help further refine the method implemented in this thesis. This refinement and others should help improve our understanding of cell responses over a range of the stress-strain values relevant to cell mechanics.

Given suitable functionalization, retraction curves from AFM indentation can also be analyzed, and their properties mapped using chemical FSM (CFSM). In chapter 3,

CFSM was made possible by coupling the probe with a fibronectin antibody, and it was used to test the fidelity of the detection method by probing an artificial pattern of a grid of squares of fibronectin made from microcontact printing (μCP). The chemical interaction between protein on the substrate and the ligand-functionalized probe created binding or adhesive forces between the two, which could be directly measured. With the appropriate controls, it was possible to then assess whether each retraction curve contained a bond-breaking event. CFSM therefore provided not just adhesive forces but with spatial information, the data could be rendered and shown in form of a spectrum of adhesive forces over area, even in conditions where loading rate and temperature were varied to probe that bond formation occurred and was measured by this method. With these parameters optimized, the detection accuracy of CFSM of protein-ligand binding can be maximized.

CFSM is also a tool that can be used to examine the adhesivity of diblock copolymer-based materials such as polystyrene-block-poly(ethylene oxide) (PS-PEO) and polystyrene-block-poly(acrylic acid) (PS-PAA) as shown in chapter 4. Probing with PLL-functionalized tips, the results showed that nanodomains with a sub-microscopic interspaced surface chemistry corresponding to %PEO content can be measured; this would not be possible with conventional light microscopy due to length scale and transparency issues. Protein adsorption on the substrate was determined for various length scales such as bulk adsorption by protein lysate and bicinchonicic acid (BCA) assay of whole samples, microscopic-scale characterization by immunofluorescence, and nanoscopic-scale examination by CFSM. The area fractions from immunofluorescence and CFSM had the same trend as the total amount of protein adsorption detected by the

BCA assay according to %PEO content; again however, spatial information cannot be obtained from the BCA assay. The macro- and micro-domain sizes were evaluated by immunofluorescence, but CFSM was able to show the presence of adhesive nanodomains. Comparing these data with nano-domains detected by CFSM on uncoated and coated PEO/PAA films indicated that PAA domains promote protein and thus adhesive site clustering at least to the same degree as observed in native matrix in chapter 1, albeit with different metrics being used.

Finally, PS-PEO and PS-PAA diblock copolymers were used as surfactants in scaffolds made from high internal phase emulsion (HIPE) polymerization (shown in chapter 5). MSCs cultured on the scaffolds of various composition of PEO had different cell adhesion as shown directly by immunofluorescence and indirectly by vinculin and actin expression. Meanwhile different cell sources such as human embryonic stem cell-derived mesenchymal progenitors (hES-MPs) and human bone marrow derived mesenchymal stem cells (hBMSCs) proliferated and differentiated differently. Evaluated by qPCR-microarray, only an adipogenic phenotype was found in hBMSCs, yet hES-MPs displayed a more mixed population with induction of adipogenic, myogenic, and osteogenic genes. While hBMSC adipogenesis was confirmed by immunofluorescence, material limitations lead one to only speculate as to why induction of multiple lineages was observed with hES-MP cells. While other parameters including topography, stiffness, etc. may have induced the response, it is clear that further investigation is warranted for these cells, especially considering that other reports claim only osteogenic differentiation on HIPE scaffolds [4,5]. Yet the differences between the polymerization methods of the work performed here versus previous reports, such as the use of a rigid

polystyrene backbone, may indicate some reason for the difference as mechanical properties is essential for stem cell differentiation [2]. Changing to different monomers could improve material compliance, yet the proper surfactants should also be considered. Moreover scaffold connectivity should also be improved by changing the water-oil phase volume ratio, polymerization temperature, surfactants, and molar ratio of surfactants and monomer.

The surface mechanical and chemical engineering with intensively investigated in subcellular scale in this dissertation has been shown the probability to fabricate biomaterials and regulate mesenchymal stem cell fate. In the aspect of stem cell engineering, this could be a promising future on the therapeutic stem-cells for regenerative medicine.

References

1 Pittenger, M.F. et al. (1999) Multilineage potential of adult human mesenchymal stem cells. *Science* 284 (5411), 143-147

2 Engler, A.J. et al. (2006) Matrix elasticity directs stem cell lineage specification. *Cell* 126 (4), 677-689

3 Kaushik, G. et al. (2011) In Situ Mechanical Analysis of Myofibrillar Perturbation and Aging on Soft, Bilayered Drosophila Myocardium. *Biophysical Journal* 101 (11), 2629-2637

4 Akay, G. et al. (2004) Microcellular polyHIPE polymer supports osteoblast growth and bone formation in vitro. *Biomaterials* 25 (18), 3991-4000

5 Bokhari, M. et al. (2007) Emulsion-templated porous polymers as scaffolds for three dimensional cell culture: effect of synthesis parameters on scaffold formation and homogeneity. *Journal of Materials Chemistry* 17 (38), 4088-4094

Appendix A

Supplemental Information for Chapter 2

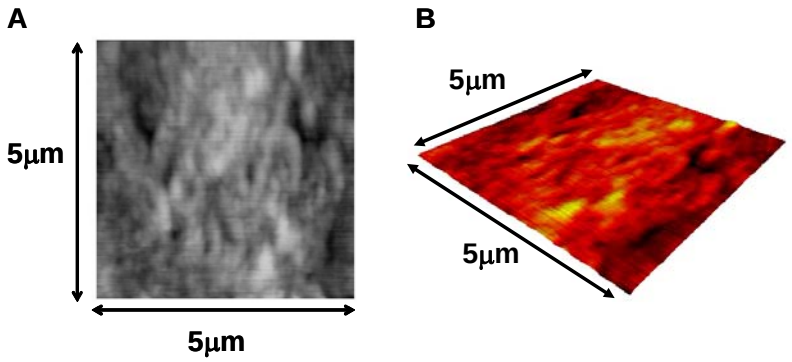

Supplemental Figure A.1: Topographic profile of the surface of Poly (vinyl pyrrolidone) hydrogel using Atomic force microscopy imagining in liquid. A) 2D image and B) 3D image.

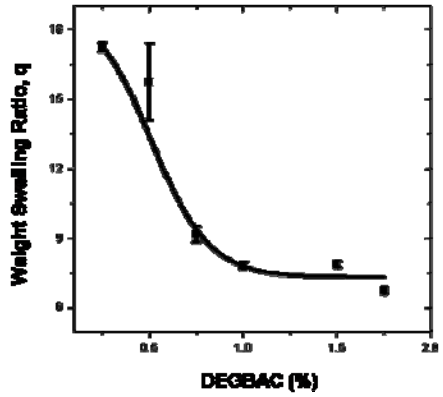

Supplemental Figure A.2: Weight Swelling Ratio (q) of Poly (vinyl pyrrolidinone) hydrogels.

Weigh Swelling Ratio. Samples of poly (vinyl pyrrolidinone) hydrogels (PVP) (0.25, 0.5, 0.75. 1.0, 1.5 and 1.75 %) were dried to a constant weight in a laminar flow hood at room temperature. Pre-weighted dry hydrogel samples (approximately 590mg) were placed in glass vials containing a solution of Phosphate buffer saline (pH=7.4) at 37± 2° C. Swelling ratio was determined gravimetrically, for this purpose samples were removed from the buffer solution and dried superficially at regular intervals of time before being weighted. The weight-swelling ratio (q) for all the samples is equal to swollen weight divided by the dry weight of the polymer sample. [1]

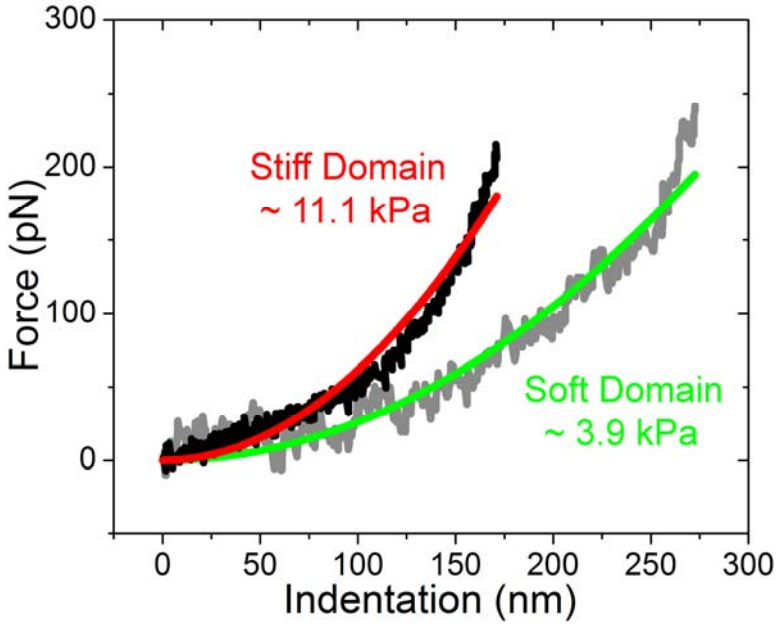

Supplemental Figure A.3: Representative indentations of a 0.5% DEGBAC gels from soft (gray) and stiff regions (black). Hertz model fit[2] was was used to determine the elasticity, either soft (green) or stiff (red), of these regions.

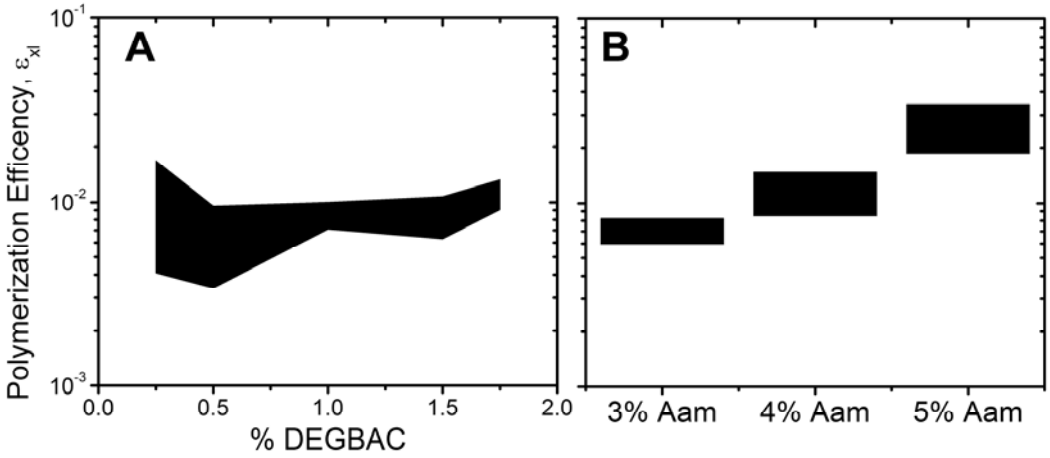

Supplemental Figure A.4: Efficiency of crosslinker polymerization, ε_{xl}, as a function of DEGBAC crosslinker, was determined for PVP hydrogels (A) using rubber elasticity theory.[3] Polymerization efficiency was also determined for PAam hydrogels (B) used in Figure 2.5. Black bars indicate the total range of crosslinking efficiencies measured.

A.1 References

1 Vakkalanka, S.K. and Peppas, N.A. (1996) *Polym. Bull.,* 36 (221)

2 Radmacher, M. et al. (1995) Imaging soft samples with the atomic force microscope: gelatin in water and propanol. *Biophys. J.,* 69 (1), 264-270

3 Flory, P.J. (1953) *Principles of Polymer Chemistry*, Cornell University Press.

Appendix B

Supplemental Information for Chapter 3

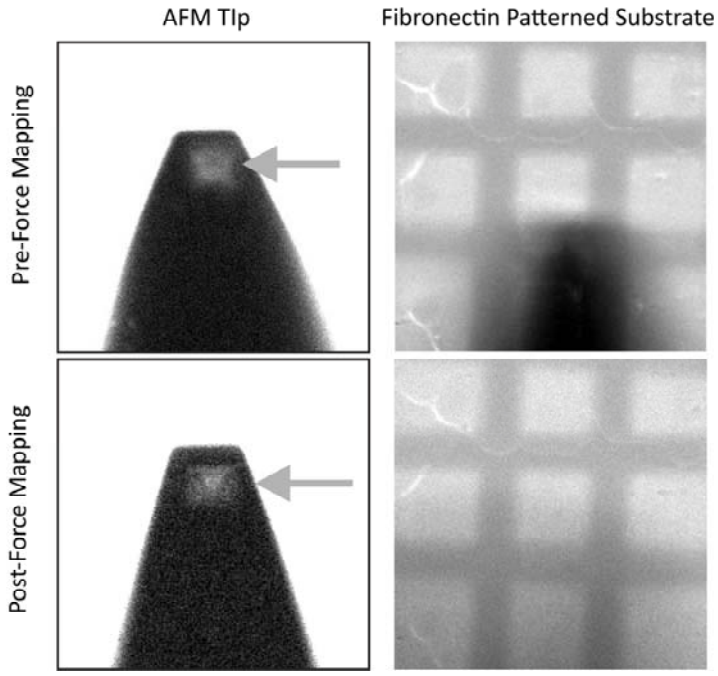

Supplemental Figure B.1: Fluorescent images of the antibody-functionalized AFM tip and fibronectin patterned substrate before and after undergoing force spectroscopy mapping are shown. Note that there is only a marginal change in the fluorescence signal on the tip post-mapping and no change in the fibronectin patterned substrates.

Appendix C

Supplemental Information for Chapter 4

C.1 Additional Materials and Methods

C.1.1 Topographical imaging by AFM

Tapping mode atomic force microscopy (TM-AFM) was applied to determine height images of 2D polymer surfaces. All samples were examined in distilled water at pH 7 at room temperature on MFP3D-BIO atomic force microscope (Asylum Research; Santa Barbara, CA) with acoustic and vibration isolation. A gold-coated, pyramidal AFM tip (TR400PB; Olympus; Center Valley, PA) with a nominal radius of 40 nm, half-angle of 35°, and spring constant of 20pN/nm was then used in TF-AFM to image the surfaces. TM-AFM images were made with a set point to resting amplitude ratio (A/A_0) of 0.5, A_0 ~ 1 V, drive frequency of ~22 kHz for the tapping, scan rate at 0.5 Hz, and a 512×512 image resolution for scan sizes of 2×2 and 20×20 μm^2. Surface roughness was determined by Igor-pro software (Wavemetrics; Portland, OR) following the formula of height root mean squared:

$$RMS = \sqrt{\Sigma y^2 / n} \qquad \text{Equation (C.1)}$$

C.1.2 Chemical Force Spectroscopy Mapping

Functionalized cantilevers were calibrated before indenting samples to account for batch-to-batch variability in tip functionalization. Using 100% PS-PEO (large adhesion forces) and 100% PS-PAA (minimal adhesion forces), force maps of 16×16 resolution over 20×20 μm^2 were performed so that adhesive forces could be internally calibrated to each cantilever. After calibration, the adhesive forces lower than one standard deviation from the average adhesion of the 100% PS-PEO map were set as non-adhesive regions. Those low tip interaction forces also overlapped with the maximum forces measured from the 100% PS-PAA map, and thus we determined this threshold for to be an acceptable definition of adhesion versus non-specific adhesion (see Supplemental Fig. 3). Using this definition, a distribution of the normalized adhesion forces was generated from all images (Fig. 3, top right) and the ratio of adhesive to total area was determined for each image, i.e. the PEO area fraction (Fig. 3, bottom left). A nano-domain, calculated by ImageJ software, was defined as at least 4 adjacent data points higher or lower than the threshold in the case of PEO or PAA domains, respectively (Fig. 3, bottom right).

C.2 Supplemental figures

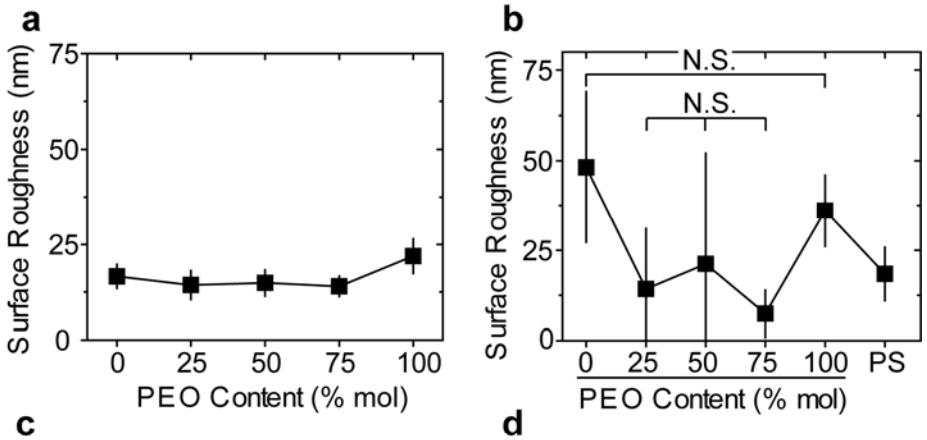

c

PEO100	Binding Energy (eV)	Atomic %
O 1s	532.6	15.93
C 1s	285.0	82.05
Ca 2p	345.0	0.07
Na 1s	1071.6	1.02
Si 2p	153.6	0.94

d

PAA100	Binding Energy (eV)	Atomic %
O 1s	532.6	9.43
C 1s	285.0	88.49
N 1s	402.2	1.12
S 2p		0.89

Supplemental Figure C.1: Surface Characterization. RMS surface roughness on 2 μm x 2 μm area of (a) 3D foams and (b) 2D films. Table of Atomic percentages of XPS of (c) PEO100 and (d) PAA100.

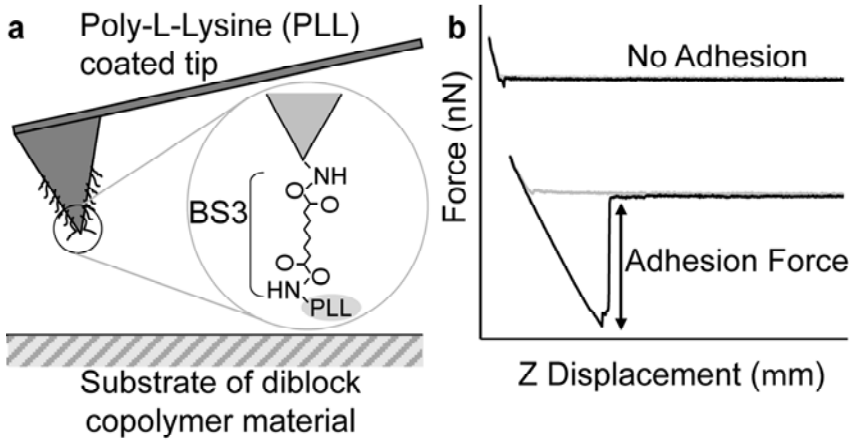

Supplemental Figure C.2: Chemical Force Spectroscopy Mapping (CFSM) (a) Probe of chemical force microscopy mapping which is covalently bond to bis[sulfo-succinimidyl] suberate (BS3) and poly-l-lysine (PLL). (b) Force curves of chemical force microscopy mapping with (bottom) and without (top) interaction between probe and surfaces.

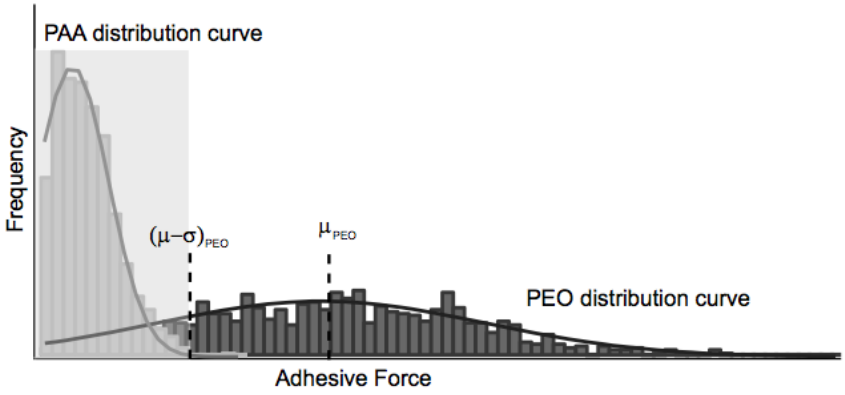

Supplemental Figure C.3: Force Histograms. Adhesive force threshold estimation to distinguish between PAA and PEO by normal distribution curves of PAA100 surface and PEO100 surface

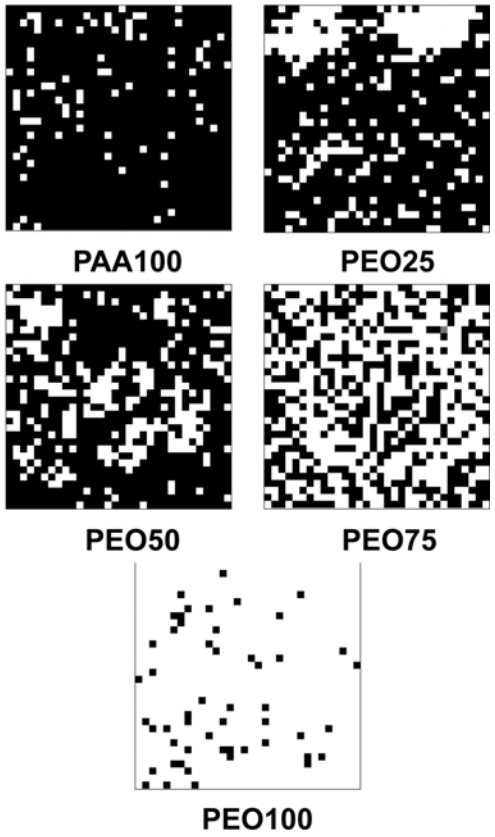

Supplemental Figure C.4: Adhesion maps. Example of chemical force maps of 20 × 20μm^2 corresponding to combination between PAA and PEO.

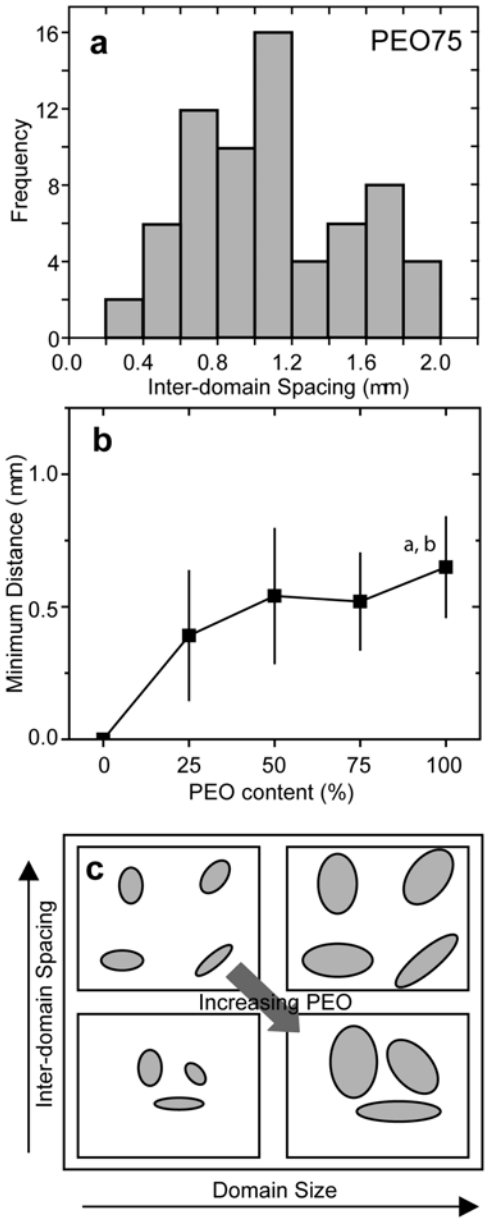

Supplemental Figure C.5: Domain Spacing. (a) The distribution of inter-domain spacing for PAA domains in a sample film. (b) Minimum distance between PEO domains as a function of bulk PEO composition. (c) Schematic relationship between inter-domain spacing and domain size. The dark gray arrow indicates the observed behavior of PEO: with increasing PEO content, PEO domain size increases while inter-domain spacing decreases.

Appendix D

Supplemental Information for Chapter 5

D.1 Preparation of 3D scaffolds for cell culture

For 3D experiments, circular scaffolds off all compositions (1.2 cm in diameter and 0.3-0.5 cm in height) were first sterilized in 70% ethanol overnight and then washed with PBS three times. Scaffolds were then pre-wet prior to seeding at a density of 10^5 cells per scaffold in total volume of 50 μl to allow maximum cell attachment. Cells were then incubated at 37 °C for 1 hour before media (1ml/well) was added. Media was replenished every 2 days. Note that no soluble induction factors were used in any experiments.

D.2 SEM and Image analysis

Scaffold morphologies were characterized by scanning electron microscopy. Fractured segments from various parts of the foam were mounted on an aluminum stub with a sticky carbon pad. Samples were gold coated (approx 15-20 nm) using an Emscope SC 500 A sputter coater unit and viewed with an FEI Inspect F field emission gun scanning electron microscope. Samples were viewed at an accelerating voltage of 5kV and a spot size of 3.0.

Porosities of the scaffolds were measured from SEM micrographs using the image analysis software Image J (NIH Image). A random selection of 100 voids were measured

from several micrographs of the same foam to obtain a more representative measurements. The assumption that the fractures of the segments exactly bisect the voids is made, which means that the measured values are all underestimates of the true value. Therefore a statistical correction is introduced[1]. This was done by evaluating the average of the ratio R/r, where R is the equatorial void diameter and r is the measured diameter on the micrograph (see figure). The statistical factor is calculated using the following formula:

$$h2 = R2 - r2 \qquad \text{Equation (D.1)}$$

Where the probability of the sectioning takes place at a distance given by h, from the centre of the void is the same for all values of h. This means that the average probability h is R/2. By substituting this in the above equation we get R/r = 2(1/3), which is the statistical correction. By multiplying this number to the measured diameters, a more representative value is obtained. Surface roughness of 3D foams was measured by image analysis using Image J.

D.3 Micro-Computational Tomography

To evaluate the porosity of the scaffolds micro CT analysis was performed using SkyScan 1172 high-resolution scanner. Scaffolds with a diameter of 1.4 cm and height of 2-3mm were used. The applied X-Ray voltage was 35kV and no filter was used. The pixel size (resolution) was 1.7µm. A total of 1400 scans were achieved and reconstructed using the SkyScan micro-CT analysis software package. Circular regions of interest (diameter=1.25 mm, height= 0.6 mm) were chosen and 3D models were generated using

the adaptive rendering algorithm available in the SkyScan software which also calculated scaffold open porosity, closed porosity, volume and pore strut thickness.

D.4 Supplemental results

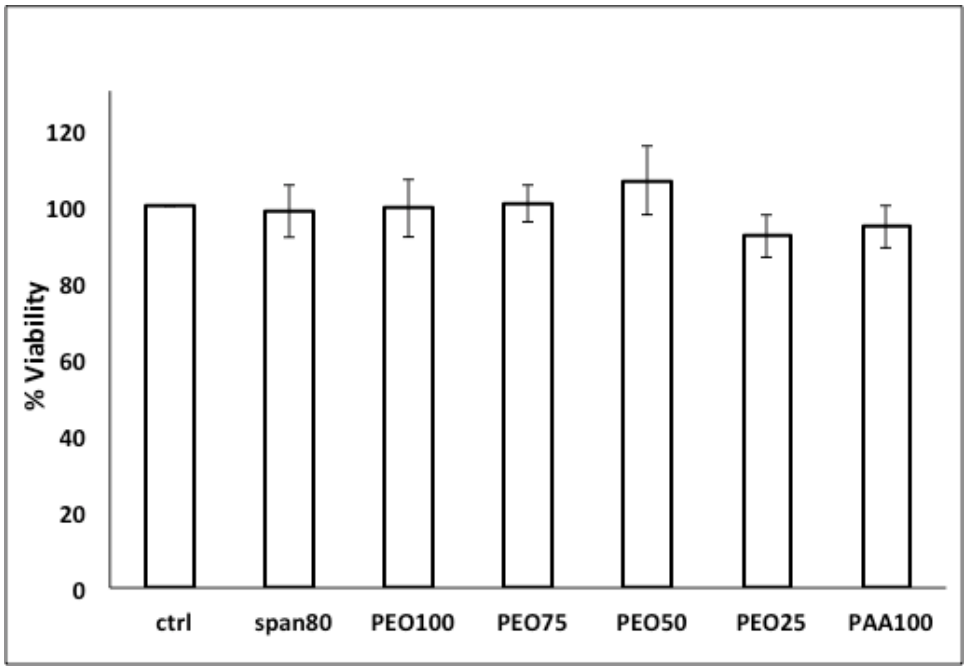

Supplemental Figure D.1: Toxicity testing of scaffolds of copolymer mixtures compared with 2D and Span 80 controls. Scaffolds were soaked in basal medium for 5 days, cells seeded were then treated with this conditioning media as they were plated and an MTT assay was performed 24 hours later to test for toxicity.

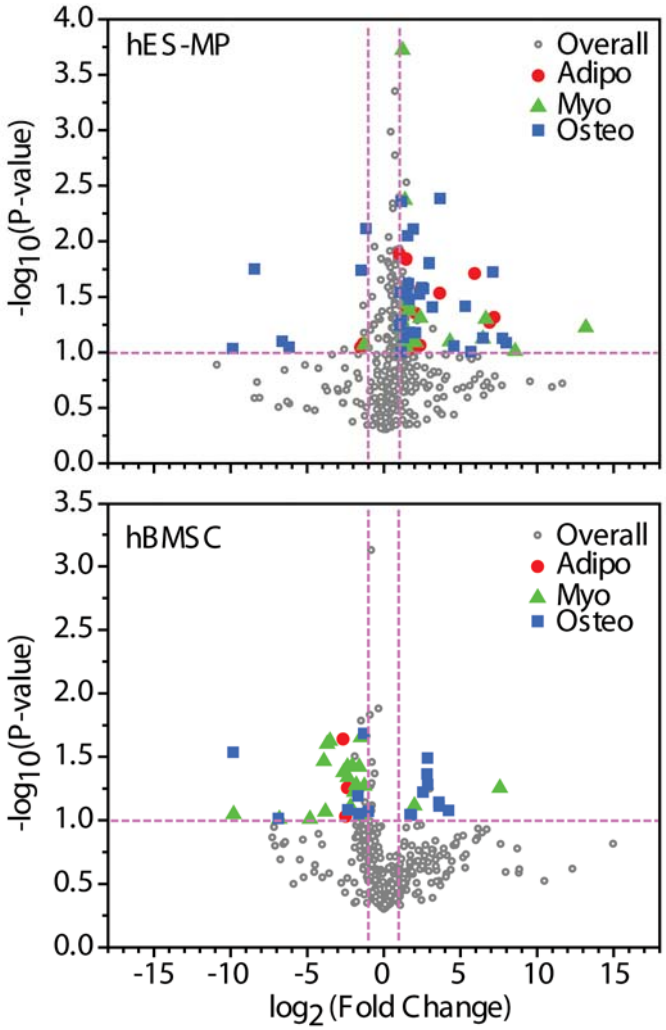

Supplemental Figure D.2: Volcano plots of the base-2 logarithm of fold change comparing with undifferentiated cell cultured on tissue culture plate against negative base-10 logarithm of P-value. The horizontal red dot line represents the significant value at P = 0.1, meanwhile the vertical represents the fold change of 2. High light in red circles, green triangles, and blue rectangles are adipogenic, myogenic, and osteogenic expression of human embryonic stem cell-derived mesenchymal progenitor (top graph) and human bone marrow-derived mesenchymal stem cell (bottom graph).

Supplemental Table D.1: Data of heat map of hES-MP gene expression after 7 days in culture on the indicated foams. All data is displayed as a fold change from undifferentiated cells.

Symbol-GID	Description	PAA100	PEO25	PEO50	PEO75	PEO100	Note
CD4-Hs00181217_m1	CD4 antigen (p55)	1.370116	3.207447	1.288065	0.871861	0.833891	MSC-like
CD44-Hs01075861_m1	CD44 antigen	1.176511	2.001224	1.483954	1.134273	1.43661	MSC-like
CD9-Hs00233521_m1	CD9 antigen (p24)	1.229727	1.684523	1.662585	0.516272	0.686614	MSC-like
ITGA1-Hs00235030_m1	Integrin, alpha 1	-0.34598	0.84502	-0.15684	0.689366	-0.18697	MSC-like
ITGA2-Hs00158127_m1	Integrin, alpha 2 (CD49B, alpha 2 subunit of VLA-2 receptor)	1.748009	2.602612	2.182825	1.009742	1.94884	MSC-like
ITGA3-Hs01076873_m1	Integrin, alpha 3 (antigen CD49C)	0.998752	0.900416	1.244429	1.114809	1.265821	MSC-like
ITGA4-Hs00168433_m1	Integrin, alpha 4 (antigen CD49D)	-1.33921	-0.37502	-0.60694	-0.35844	-0.74294	MSC-like
IL2RA-Hs00907778_m1	Interleukin 2 receptor, alpha (IL2RA)	1.210702	2.089822	0.02299	-0.84001	11.65834	MSC-like
CD34-Hs02576480_m1	CD34 antigen	-1.28782	1.352201	0.323038	0.898934	0.952242	MSC-like
PTPRC-Hs00236304_m1	Protein tyrosine phosphatase, receptor type, C	-0.53591	1.689225	-1.72363	-2.58662	-0.09922	MSC-like
ENG-Hs00923986_m1	Endoglin; CD105	1.074315	1.405897	1.005838	0.625478	1.149467	MSC-like
THY1-Hs00174816_m1	Thy-1 cell surface antigen	1.342088	0.568154	1.085017	0.423678	0.635098	MSC-like
PAX3-Hs00992437_m1	Paired box gene 3	6.127621	4.307693	5.631713	0.983098	2.78054	Myo-like
PAX7-Hs00242962_m1	Paired box gene 7	-1.07343	1.687007	2.817901	3.669572	1.654872	Myo-like
MYOD1-Hs00159528_m1	Myogenic Factor 3 (MYOD1)	4.07241	2.089822	0.02299	-0.84001	0.298948	Myo-like
MYOG-Hs01072232_m1	Myogenic Factor 4 (Myogenin)	0.802932	4.779949	-3.69376	2.824708	3.91242	Myo-like
MYF5-Hs00271574_m1	Myogenic Factor 5	3.806667	-3.00146	7.241888	13.18011	1.483662	Myo-like
MYF6-Hs00231165_m1	Myogenic Factor 6 (herculin)/Mrf4	5.932363	2.089822	8.570708	-0.84001	5.620987	Myo-like
MEOX2-Hs00232248_m1	Mesenchyme homeo box 2 (growth arrest-specific homeo box)	3.978212	2.089822	0.02299	-0.84001	10.9817	Myo-like
FOXK1-Hs01595620_m1	Forkhead box K1 (KIAA0415)/MNF	0.429692	0.142743	0.743707	0.533281	1.036883	Myo-like
MSTN-Hs00976237_m1	Growth differentiation factor 8 (GDF8)/myostatin	6.655553	5.731352	6.52493	6.472233	3.562145	Myo-like
MEF2A-Hs00271535_m1	MADS box transcription enhancer factor 2, polypeptide A	-0.45182	1.829737	0.954687	1.25474	1.1662	Myo-like
LOC729991-MEF2B;MEF2B-Hs01021286_m1	MADS box transcription enhancer factor 2, polypeptide B	0.352557	0.144381	0.684146	0.829969	1.224284	Myo-like
MEF2C-Hs00231149_m1	MADS box transcription enhancer factor 2, polypeptide C	1.435345	1.414376	1.624878	0.842315	1.328415	Myo-like

Supplemental Table D.1: Data of heat map of hES-MP gene expression after 7 days in culture on the indicated foams. All data is displayed as a fold change from undifferentiated cells. (continue)

Symbol-GID	Description	PAA100	PEO25	PEO50	PEO75	PEO100	Note
MEF2D-Hs00232237_m1	MADS box transcription enhancer factor 2, polypeptide D	0.744234	2.122654	1.382121	0.937969	1.0437	Myo-like
GRB2-Hs00157817_m1	Growth factor receptor-bound protein 2	1.517617	2.076399	1.458747	1.00447	1.284202	Myo-like
DES-Hs00157258_m1	Desmin	-0.07962	-0.62614	-1.26241	-0.42643	-1.62812	Myo-like
MSX1-Hs00427183_m1	Msh homeo box homolog 1	0.806522	0.952505	1.657293	0.941516	1.899899	Myo-like
MSX2-Hs00741177_m1	Msh homeo box homolog 2	0.238	1.107536	0.786418	-0.1385	0.93713	Myo-like
LBX1-Hs00198080_m1	Ladybird homeobox homolog 1	0.522552	0.709087	0.072645	0.291362	-2.31762	Myo-like
NRAP-Hs00328987_m1	Nebulin-related anchoring protein	1.210702	2.089822	0.02299	-0.84001	0.298948	Myo-like
MYOT-Hs00199016_m1	Titin immunoglobulin domain protein (myotilin)	-8.27747	-4.494	-8.09781	-6.86087	-8.43879	Myo-like
TTN-Hs00399225_m1	Titin	1.210702	2.089822	2.386893	-0.84001	1.402737	Myo-like
CDH15-Hs00170504_m1	Cadherin 15, M-cadherin (myotubule)	1.210702	6.980902	0.02299	9.540572	0.298948	Myo-like
ITGB1-Hs01127543_m1	Integrin, Beta 1D	0.088255	0.847759	0.314917	0.222432	0.069572	Myo-like
ITGA7-Hs01056475_m1	Integrin, Alpha 7 (Muscle)	1.144128	0.232152	0.45989	-0.12575	-1.65607	Myo-like
RUNX2-Hs01047976_m1	Core Binding Factor Alpha 1	-0.04613	1.116269	0.29063	0.457558	0.965867	Osteo-like
CDH11-Hs00901475_m1	Cadherin 11, type 2, OB-cadherin (osteoblast)	-0.19213	0.391462	-0.10014	0.248083	-0.24644	Osteo-like
SPP1-Hs00959009_m1	Secreted phosphoprotein 1 (osteopontin)	2.486393	3.239134	3.664667	2.603084	2.966988	Osteo-like
TFIP11-Hs00201749_m1	Tuftelin interacting protein 11	0.771565	2.062508	1.155049	0.443461	0.751975	Osteo-like
TWIST1-Hs00361186_m1	Twist homolog 1 (acrocephalosyndactyly 3)	0.510055	0.994984	0.979656	0.740772	0.234266	Osteo-like
TWIST2-Hs00382379_m1	Twist homolog 2	4.580946	6.480531	2.331914	0.824672	0.721357	Osteo-like
SOX9-Hs00165814_m1	SRY (sex determining region Y)-box 9	1.044182	0.796241	1.926098	1.555717	1.698624	Osteo-like
SMAD1-Hs00195432_m1	SMAD, mothers against DPP homolog 1	0.144588	0.631538	-0.1777	0.085283	0.155667	Osteo-like
SMAD2-Hs00183425_m1	SMAD, mothers against DPP homolog 2	0.351553	1.364225	0.513051	0.270203	0.445436	Osteo-like
SMAD3-Hs00232222_m1	SMAD, mothers against DPP homolog 3	-0.03329	0.989969	0.694163	0.744128	0.764377	Osteo-like
SMAD4-Hs00929647_m1	SMAD, mothers against DPP homolog 4	-0.00774	0.701569	-0.00271	0.116345	-0.0424	Osteo-like
SMAD5-Hs00195437_m1	SMAD, mothers against DPP homolog 5	0.204285	1.051782	0.627987	0.227967	0.683526	Osteo-like

Supplemental Table D.1: Data of heat map of hES-MP gene expression after 7 days in culture on the indicated foams. All data is displayed as a fold change from undifferentiated cells. (continue)

Symbol-GID	Description	PAA100	PEO25	PEO50	PEO75	PEO100	Note
SMAD6-Hs00178579_m1	SMAD, mothers against DPP homolog 6	1.523452	0.319158	1.659174	0.949842	1.287539	Osteo-like
SMAD7-Hs00998193_m1	SMAD, mothers against DPP homolog 7	0.411051	-0.781	0.337799	-0.12491	0.078205	Osteo-like
SMAD9-Hs00195441_m1	SMAD, mothers against DPP homolog 9	-0.41438	-0.29953	0.121894	0.072878	0.300673	Osteo-like
VDR-Hs00172113_m1	Vitamin D receptor (1,25-dihydroxyvitamin D3)	-0.18337	-0.245	-0.04795	0.292137	0.574133	Osteo-like
BGLAP;PMF1-BGLAP-Hs00609452_g1	Bone gamma-carboxyglutamate (gla) protein (osteocalcin)	1.291338	1.123254	1.126962	0.393117	1.12273	Osteo-like
BMP1-Hs00241807_m1	Bone morphogenetic protein 1	0.194126	-0.2465	-0.05183	0.339318	0.138458	Osteo-like
BMP2-Hs01055564_m1	Bone morphogenetic protein 2	-0.19121	1.838459	2.071197	1.080267	1.610882	Osteo-like
BMP3-Hs00609638_m1	Bone morphogenetic protein 3	-2.03472	-5.01265	-6.31602	-6.16644	3.178457	Osteo-like
BMP4-Hs00370078_m1	Bone morphogenetic protein 4	-1.16564	1.209286	-1.12888	-2.5328	-0.48264	Osteo-like
BMP5-Hs00234930_m1	Bone morphogenetic protein 5	7.703177	4.572305	2.185741	6.525733	-2.62943	Osteo-like
BMP6-Hs01099594_m1	Bone morphogenetic protein 6	7.738475	7.984426	7.112194	5.675396	5.317488	Osteo-like
BMP7-Hs00233476_m1	Bone morphogenetic protein 7 (osteogenic protein 1)	3.043535	0.802279	3.64567	-0.7133	-6.46586	Osteo-like
BMP8B;BMP8A-Hs00236942_m1	Bone morphogenetic protein 8b (osteogenic protein 2)	-6.16931	-8.43494	-6.62353	-10.8985	-9.8516	Osteo-like
BMPR1A-Hs01034909_g1	Bone morphogenetic protein receptor, type IA	0.597017	1.840109	0.642963	0.430449	0.656216	Osteo-like
MGP-Hs00179899_m1	Matrix Gla protein	4.095873	1.221681	4.963249	1.142971	0.843895	Osteo-like
COL1A1-Hs00164004_m1	Collagen, type I, alpha 1	-0.45081	-0.26598	-0.64372	0.046753	-0.4184	Osteo-like
COL1A2-Hs01028970_m1	Collagen, type I, alpha 2	-0.16931	0.05346	-0.45877	0.393743	0.222525	Osteo-like
COL3A1-Hs00164103_m1	Collagen, type 3, alpha 1	-0.95812	-0.58057	-1.4792	-0.50082	-0.85869	Osteo-like
DLK1-Hs00171584_m1	transmembrane protein containing six epidermal growth factor repeats	-1.51341	-0.63429	0.305733	-0.76796	-2.42517	Preadipocyte
PPARG-Hs01115510_m1	peroxisome proliferator-activated receptor (PPAR)	2.884077	1.902169	-5.13058	-1.32321	0.181024	Early Adipose
CEBPA-Hs00269972_s1	modulates the expression of the gene encoding leptin	1.109925	3.260406	1.697435	1.183068	2.677248	Early Adipose
CEBPB-Hs00270923_s1	modulates the expression of the gene encoding leptin	0.20261	0.930149	0.697707	0.206839	0.421634	Early Adipose

Supplemental Table D.1: Data of heat map of hES-MP gene expression after 7 days in culture on the indicated foams. All data is displayed as a fold change from undifferentiated cells. (continue)

Symbol-GID	Description	PAA100	PEO25	PEO50	PEO75	PEO100	Note
KLF15-Hs00362736_m1	Regulation of gluconeogenesis	-0.18834	5.92683	2.97898	2.368645	0.10195	Early Adipose
FABP4-Hs01086177_m1	fatty acid binding protein found in adipocytes; aP2	0.572557	0.424745	0.732056	1.023433	1.456367	Early Adipose
SREBF1-Hs00231674_m1	sterol regulatory element binding transcription factor 1	1.750349	2.166658	1.48862	1.014325	1.389521	General Adipose
GPD1L-Hs00380515_m1	metabolism gene	0.315069	1.07094	0.324758	-0.1343	0.227317	Mid Adipose
LPL-Hs01012569_m1	lipoprotein lipase, which is expressed in adipose tissue	-4.2548	-3.37568	2.977596	6.277777	0.493999	Mid Adipose
NR1H3-Hs00172885_m1	The liver X receptors, LXRA	0.126815	1.287173	0.285751	-0.19987	0.073988	Late Adipose
LEP-Hs00174877_m1	a protein that is secreted by white adipocytes	2.016579	3.978195	6.897295	7.205626	5.162063	Late Adipose
ADIPOQ-Hs00605917_m1	C1Q and collagen domain containing, transcript variant 1	3.49098	6.730573	-1.24541	3.660935	-0.2521	Late Adipose
LIPE-Hs00193510_m1	hydrolyzes stored triglycerides to fatty acids	-1.77349	-0.89437	-2.96121	-3.8242	-2.68525	Late Adipose
GATA2-Hs00231119_m1	Development and proliferation of hematopoietic cell lineage	2.087541	1.62549	2.431866	0.590451	0.605632	Adipose inhibition

Supplemental Table D.2: Data of heat map of hBMSC gene expression after 7 days in culture on the indicated foams. All data is displayed as a fold change from undifferentiated cells.

Symbol-GID	Description	PAA100	PEO25	PEO50	PEO75	PEO100	Note
CD4-Hs00181217_m1	CD4 antigen (p55)	-0.3581	0.182879	1.075528	0.555306	1.419881	MSC-like
CD44-Hs01075861_m1	CD44 antigen	-1.69894	-1.58436	-1.30946	0.051323	-0.95124	MSC-like
CD9-Hs00233521_m1	CD9 antigen (p24)	0.016082	-0.02829	1.035952	0.627881	0.609183	MSC-like
ITGA1-Hs00235030_m1	Integrin, alpha 1	-0.12986	-0.30247	0.761468	0.354624	1.081878	MSC-like
ITGA2-Hs00158127_m1	Integrin, alpha 2 (CD49B, alpha 2 subunit of VLA-2 receptor)	-0.97742	-0.14779	-0.79073	-0.74177	-0.0253	MSC-like
ITGA3-Hs01076873_m1	Integrin, alpha 3 (antigen CD49C)	-1.87828	-1.40407	-1.45589	-0.25127	-1.16099	MSC-like
ITGA4-Hs00168433_m1	Integrin, alpha 4 (antigen CD49D)	-1.38923	-1.27486	0.042655	-0.08828	-0.41217	MSC-like
IL2RA-Hs00907778_m1	Interleukin 2 receptor, alpha (IL2RA)	-0.27575	0.144836	3.618489	3.446586	3.098924	MSC-like
CD34-Hs02576480_m1	CD34 antigen	8.815919	-1.89793	5.179718	2.597715	2.564563	MSC-like
PTPRC-Hs00236304_m1	Protein tyrosine phosphatase, receptor type, C	1.06202	0.779927	0.96667	1.225246	-1.26658	MSC-like
ENG-Hs00923986_m1	Endoglin; CD105	-0.84575	-0.49383	-0.56146	-0.81664	-0.26133	MSC-like
THY1-Hs00174816_m1	Thy-1 cell surface antigen	-0.24643	-0.37525	0.186892	-1.26197	0.48163	MSC-like
PAX3-Hs00992437_m1	Paired box gene 3	-7.26863	0.943432	3.697392	-6.7455	-2.38201	Myo-like
PAX7-Hs00242962_m1	Paired box gene 7	-6.55432	-5.22413	-5.8827	-1.80029	2.262515	Myo-like
MYOD1-Hs00159528_m1	Myogenic Factor 3 (MYOD1)	7.617104	1.484291	3.618489	7.960193	12.31357	Myo-like
MYOG-Hs01072232_m1	Myogenic Factor 4 (Myogenin)	-1.91457	1.064908	-4.81726	-9.79653	-4.25505	Myo-like
MYF5-Hs00271574_m1	Myogenic Factor 5	-7.16159	-6.80757	-3.51702	-3.70297	-3.90224	Myo-like
MYF6-Hs00231165_m1	Myogenic Factor 6 (herculin)/Mrf4	-2.62201	-4.48743	0.756035	-3.80419	2.140323	Myo-like
MEOX2-Hs00232248_m1	Mesenchyme homeo box 2 (growth arrest-specific homeo box)	-2.17337	-2.38235	-1.79125	-2.34472	-1.56271	Myo-like
FOXK1-Hs01595620_m1	Forkhead box K1 (KIAA0415)/MNF	-0.43145	0.192885	-0.7444	-1.00525	-0.20975	Myo-like
MSTN-Hs00976237_m1	Growth differentiation factor 8 (GDF8)/myostatin	-1.90648	-1.58126	1.99061	8.713626	0.995899	Myo-like
MEF2A-Hs00271535_m1	MADS box transcription enhancer factor 2, polypeptide A	-2.06734	-1.7991	0.304348	-0.20354	-0.53041	Myo-like
LOC729991-MEF2B;MEF2B-Hs01021286_m1	MADS box transcription enhancer factor 2, polypeptide B	-1.06783	-0.1149	1.321734	0.976495	0.553852	Myo-like

Supplemental Table D.2: Data of heat map of hBMSC gene expression after 7 days in culture on the indicated foams. All data is displayed as a fold change from undifferentiated cells. (continue)

Symbol-GID	Description	PAA100	PEO25	PEO50	PEO75	PEO100	Note
MEF2C-Hs00231149_m1	MADS box transcription enhancer factor 2, polypeptide C	-0.83174	-0.34533	0.799489	0.282248	0.194034	Myo-like
MEF2D-Hs00232237_m1	MADS box transcription enhancer factor 2, polypeptide D	-1.52622	-1.09989	-1.36074	0.004251	-1.68927	Myo-like
GRB2-Hs00157817_m1	Growth factor receptor-bound protein 2	-0.93835	-0.65278	-1.26412	-1.35081	-0.83579	Myo-like
DES-Hs00157258_m1	Desmin	-1.91247	-1.59379	0.868937	0.210477	0.039018	Myo-like
MSX1-Hs00427183_m1	Msh homeo box homolog 1	-1.8495	-1.06113	1.061701	0.425811	0.183023	Myo-like
MSX2-Hs00741177_m1	Msh homeo box homolog 2	-0.98131	-0.82331	1.436416	1.124278	0.978967	Myo-like
LBX1-Hs00198080_m1	Ladybird homeobox homolog 1	-1.02027	-1.27384	-2.7652	-3.57012	0.062493	Myo-like
NRAP-Hs00328987_m1	Nebulin-related anchoring protein	-0.27575	1.832231	5.363151	3.446586	3.098924	Myo-like
MYOT-Hs00199016_m1	Titin immunoglobulin domain protein (myotilin)	3.443817	2.889356	6.718237	6.425289	7.572484	Myo-like
TTN-Hs00399225_m1	Titin	-1.4869	0.035057	0.555714	0.396412	-0.16059	Myo-like
CDH15-Hs00170504_m1	Cadherin 15, M-cadherin (myotubule)	0.300888	1.356411	3.209232	3.359377	2.716261	Myo-like
ITGB1-Hs01127543_m1	Integrin, Beta 1D	-0.77739	-0.50795	-0.73643	-0.59436	-0.77324	Myo-like
ITGA7-Hs01056475_m1	Integrin, Alpha 7 (Muscle)	-0.16424	-0.06341	-0.05761	-0.35267	0.557487	Myo-like
RUNX2-Hs01047976_m1	Core Binding Factor Alpha 1	-1.20235	-0.97769	-0.59695	-0.92875	0.247459	Osteo-like
CDH11-Hs00901475_m1	Cadherin 11, type 2, OB-cadherin (osteoblast)	-0.07321	-0.1918	-0.78809	-1.10375	0.002212	Osteo-like
SPP1-Hs00959009_m1	Secreted phosphoprotein 1 (osteopontin)	0.113006	0.61608	1.096847	0.698387	1.29308	Osteo-like
TFIP11-Hs00201749_m1	Tuftelin interacting protein 11	-1.29407	-0.57954	8.844891	-1.70112	-1.26342	Osteo-like
TWIST1-Hs00361186_m1	Twist homolog 1 (acrocephalosyndactyly 3)	-1.67874	-1.63912	-0.84953	4.061803	-0.3916	Osteo-like
TWIST2-Hs00382379_m1	Twist homolog 2	-2.34131	-1.33639	0.091052	-0.41669	-0.56599	Osteo-like
SOX9-Hs00165814_m1	SRY (sex determining region Y)-box 9	-0.70455	-0.04775	1.519516	-0.34628	-0.29204	Osteo-like
SMAD1-Hs00195432_m1	SMAD, mothers against DPP homolog 1	-0.74971	-0.40756	0.017103	-0.34811	0.825451	Osteo-like
SMAD2-Hs00183425_m1	SMAD, mothers against DPP homolog 2	-0.60235	-0.29284	-0.28729	0.337346	-0.91646	Osteo-like
SMAD3-Hs00232222_m1	SMAD, mothers against DPP homolog 3	-0.99928	-0.85093	-0.25278	-0.72234	-0.90156	Osteo-like
SMAD4-Hs00929647_m1	SMAD, mothers against DPP homolog 4	-0.58042	-0.49812	-0.08326	-0.35294	-0.78379	Osteo-like
SMAD5-Hs00195437_m1	SMAD, mothers against DPP homolog 5	-0.8708	-0.45137	0.064817	-1.30945	-0.03714	Osteo-like

Supplemental Table D.2: Data of heat map of hBMSC gene expression after 7 days in culture on the indicated foams. All data is displayed as a fold change from undifferentiated cells. (continue)

Symbol-GID	Description	PAA100	PEO25	PEO50	PEO75	PEO100	Note
SMAD6-Hs00178579_m1	SMAD, mothers against DPP homolog 6	-0.41518	-0.36143	-0.48225	-0.66578	-1.00824	Osteo-like
SMAD7-Hs00998193_m1	SMAD, mothers against DPP homolog 7	-0.89583	-0.30587	-0.81675	-0.85441	-1.16594	Osteo-like
SMAD9-Hs00195441_m1	SMAD, mothers against DPP homolog 9	-1.30113	-1.01052	0.017376	-0.3197	-0.58497	Osteo-like
VDR-Hs00172113_m1	Vitamin D (1,25-dihydroxyvitamin D3) receptor	-1.05648	0.512155	1.148759	1.08401	0.33256	Osteo-like
BGLAP;PMF1-BGLAP-Hs00609452_g1	Bone gamma-carboxyglutamate (gla) protein (osteocalcin)	0.660511	0.690119	0.518204	0.159073	1.316141	Osteo-like
BMP1-Hs00241807_m1	Bone morphogenetic protein 1	-0.37171	0.168888	-0.01335	-0.28265	-0.62788	Osteo-like
BMP2-Hs01055564_m1	Bone morphogenetic protein 2	0.874271	1.898101	2.522018	2.658316	2.132833	Osteo-like
BMP3-Hs00609638_m1	Bone morphogenetic protein 3	-0.64296	1.364455	3.606054	3.590568	3.004939	Osteo-like
BMP4-Hs00370078_m1	Bone morphogenetic protein 4	-0.63516	-0.11391	0.384829	0.094677	-0.10948	Osteo-like
BMP5-Hs00234930_m1	Bone morphogenetic protein 5	-0.73024	4.559972	4.230227	3.9077	4.714086	Osteo-like
BMP6-Hs01099594_m1	Bone morphogenetic protein 6	-2.09536	-0.82504	-0.4035	-0.66992	-0.91043	Osteo-like
BMP7-Hs00233476_m1	Bone morphogenetic protein 7 (osteogenic protein 1)	-6.431	-5.48386	-4.53602	-1.129	-0.51451	Osteo-like
BMP8B;BMP8A-Hs00236942_m1	Bone morphogenetic protein 8b (osteogenic protein 2)	-5.28669	-9.83003	-1.08634	2.934189	-6.87594	Osteo-like
BMPR1A-Hs01034909_g1	Bone morphogenetic protein receptor, type IA	-0.51247	-0.38805	1.485803	0.779492	1.288053	Osteo-like
MGP-Hs00179899_m1	Matrix Gla protein	2.824218	2.868327	2.852794	2.564669	2.17399	Osteo-like
COL1A1-Hs00164004_m1	Collagen, type I, alpha 1	-0.72291	-0.71241	-0.06815	0.034804	0.412804	Osteo-like
COL1A2-Hs01028970_m1	Collagen, type I, alpha 2	0.389823	0.292021	0.13379	0.323597	0.089227	Osteo-like
COL3A1-Hs00164103_m1	Collagen, type 3, alpha 1	1.723558	1.790784	0.502788	0.673538	1.467463	Osteo-like
DLK1-Hs00171584_m1	transmembrane protein containing six epidermal growth factor repeats	3.396376	4.128946	6.106872	6.008695	6.154662	Preadipocyte
PPARG-Hs01115510_m1	peroxisome proliferator-activated receptor (PPAR)	1.345623	2.646429	4.085669	2.082167	4.433485	Early Adipose
CEBPA-Hs00269972_s1	modulates the expression of the gene encoding leptin	-1.53645	-0.26313	1.854715	2.356322	2.519658	Early Adipose
CEBPB-Hs00270923_s1	modulates the expression of the gene encoding leptin	0.215316	0.199095	1.715176	1.460748	2.240238	Early Adipose
KLF15-Hs00362736_m1	Regulation of gluconeogenesis	1.039377	0.28627	3.686426	3.389157	3.158473	Early Adipose

Supplemental Table D.2: Data of heat map of hBMSC gene expression after 7 days in culture on the indicated foams. All data is displayed as a fold change from undifferentiated cells. (continue)

Symbol-GID	Description	PAA100	PEO25	PEO50	PEO75	PEO100	Note
FABP4-Hs01086177_m1	fatty acid binding protein found in adipocytes; aP2	-1.32696	-2.48711	0.428793	0.307353	-0.50909	Early Adipose
SREBF1-Hs00231674_m1	sterol regulatory element binding transcription factor 1	-0.47221	-0.28903	-0.0776	0.484247	-0.80242	General Adipose
GPD1L-Hs00380515_m1	metabolism gene	0.222271	-0.03719	2.439293	-0.07722	1.703643	Mid Adipose
LPL-Hs01012569_m1	lipoprotein lipase, which is expressed in adipose tissue	-4.02479	-7.09314	-2.52305	-0.39607	-4.01667	Mid Adipose
NR1H3-Hs00172885_m1	The liver X receptors, LXRA	0.635253	0.460372	2.367289	2.258199	1.728805	Late Adipose
LEP-Hs00174877_m1	a protein that is secreted by white adipocytes	2.432918	0.153723	4.686981	4.819954	3.910892	Late Adipose
ADIPOQ-Hs00605917_m1	C1Q and collagen domain containing, transcript variant 1	1.766442	-0.16453	5.311997	3.142369	5.187592	Late Adipose
LIPE-Hs00193510_m1	hydrolyzes stored triglycerides to fatty acids	-0.27575	0.144836	3.618489	3.446586	3.098924	Late Adipose
GATA2-Hs00231119_m1	Development and proliferation of hematopoietic cell lineage	-2.65674	-2.37392	-0.19859	-0.37796	-0.73417	Adipose inhibition

Supplemental Table D.3: Significant gene expression of hES-MP after 7 days on each foam grouped by material composition and listed by increasing PEO percentage. Fold change was calculated as a change from undifferentiated cells. P-values were computed for each gene between undifferentiated cells and those cultured on each specific foam composition from triplicate cultures.

Sample	Detector	$\log_2$(Fold Change)	$-\log_{10}$(P-value)
PAA100	CD44	1.4366095	1.307543438
PAA100	ITGA2	1.948839833	1.008702687
PAA100	ITGA3	1.265820833	1.215043462
PAA100	MEF2A	1.166200167	1.290926129
PAA100	MEF2B	1.2242835	3.721489701
PAA100	MEF2C	1.3284145	1.209596635
PAA100	MEF2D	1.043700167	1.026369774
PAA100	MSX1	1.899899167	1.117417621
PAA100	SPP1	2.9669875	1.804377441
PAA100	SOX9	1.698624167	1.182337561
PAA100	SMAD6	1.2875385	1.134273711
PAA100	BGLAP	1.122729833	1.288320838
PAA100	BMP2	1.610882167	1.621803068
PAA100	BMP3	3.178457167	1.409106909
PAA100	BMP6	5.3174875	1.416550525
PAA100	BMP8B	-9.8516035	1.035096739
PAA100	FABP4	1.4563665	1.839356588
PEO25	CD44	1.134272667	1.569715275
PEO25	ITGA3	1.114809	1.613121156
PEO25	PTPRC	-2.586621667	1.028808262
PEO25	MYF5	13.18011267	1.226736176
PEO25	MSTN	6.472233	1.125586802
PEO25	MEF2A	1.254740333	1.154167363
PEO25	SPP1	2.603084333	1.57664235
PEO25	SOX9	1.555717333	2.045561063
PEO25	BMP2	1.080267	1.54148329
PEO25	BMP6	5.675395667	1.007705118
PEO25	PPARG	-1.323205333	1.080011901
PEO25	KLF15	2.368644667	1.064725403
PEO25	SREBF1	1.014325333	1.884200214
PEO25	LEP	7.205625667	1.315838073
PEO25	ADIPOQ	3.660934667	1.534615411
PEO50	CD44	1.4839535	2.529265442
PEO50	CD9	1.662585167	1.645607639

Supplemental Table D.3: Significant gene expression of hES-MP after 7 days on each foam grouped by material composition and listed by increasing PEO percentage. Fold change was calculated as a change from undifferentiated cells. P-values were computed for each gene between undifferentiated cells and those cultured on each specific foam composition from triplicate cultures. (continue)

Sample	Detector	$\log_2$(Fold Change)	$-\log_{10}$(P-value)
PEO50	ITGA2	2.182825167	1.288776806
PEO50	ITGA3	1.244429167	1.728283709
PEO50	ENG	1.0058375	1.856256035
PEO50	THY1	1.085017167	1.851071757
PEO50	MYF6	8.570707833	1.012208215
PEO50	MEF2C	1.6248775	1.437276164
PEO50	MEF2D	1.382121167	2.37014295
PEO50	GRB2	1.458747167	1.049378102
PEO50	DES	-1.2624065	1.068247905
PEO50	MSX1	1.657293167	1.377289433
PEO50	TTN	2.386892833	1.311853587
PEO50	SPP1	3.664666833	2.383501272
PEO50	TFIP11	1.155049167	2.354892867
PEO50	TWIST2	2.331913833	1.526118402
PEO50	SOX9	1.926097833	2.107487381
PEO50	SMAD6	1.6591735	1.479702586
PEO50	BGLAP	1.126962167	1.002812984
PEO50	BMP2	2.0711965	1.178982348
PEO50	BMP6	7.112193833	1.72532184
PEO50	BMP8B	-6.623532833	1.100109809
PEO50	COL3A1	-1.479204167	1.742023257
PEO50	CEBPA	1.697434833	1.03504124
PEO50	SREBF1	1.488619833	1.404231995
PEO50	LEP	6.897294833	1.270421415
PEO50	GATA2	2.4318655	1.578645186
PEO75	CD4	3.207447167	1.214351228
PEO75	PAX3	4.307693167	1.098657343
PEO75	GRB2	2.0763985	1.09129317
PEO75	TWIST2	6.4805305	1.129542469
PEO75	BMP6	7.9844255	1.086522966
PEO75	BMP8B	-8.434944167	1.754147148
PEO75	KLF15	5.9268295	1.713031612
PEO75	GATA2	1.6254895	1.173399208

Supplemental Table D.3: Significant gene expression of hES-MP after 7 days on each foam grouped by material composition and listed by increasing PEO percentage. Fold change was calculated as a change from undifferentiated cells. P-values were computed for each gene between undifferentiated cells and those cultured on each specific foam composition from triplicate cultures. (continue)

Sample	Detector	$\log_2$(Fold Change)	$-\log_{10}$(P-value)
PEO100	CD44	1.176510667	1.66269296
PEO100	CD9	1.229727333	1.266974467
PEO100	ITGA2	1.748009333	1.052503485
PEO100	ITGA4	-1.339206333	1.423176711
PEO100	CD34	-1.287815667	1.177140828
PEO100	ENG	1.074314667	1.418569402
PEO100	THY1	1.342087667	1.251046141
PEO100	MSTN	6.655553	1.304053967
PEO100	MEF2C	1.435344667	1.448546672
PEO100	GRB2	1.517617333	1.519616411
PEO100	ITGA7	1.144128	1.276446775
PEO100	SPP1	2.486393	1.585573713
PEO100	TWIST2	4.580946333	1.056819717
PEO100	SOX9	1.044181667	1.244705266
PEO100	SMAD6	1.523452	1.52062264
PEO100	BMP4	-1.165639667	2.112114297
PEO100	BMP6	7.738475333	1.12833142
PEO100	BMP8B	-6.169314	1.04879365
PEO100	DLK1	-1.513414	1.046645458
PEO100	SREBF1	1.750348667	1.158045395
PEO100	GATA2	2.087541333	1.353223268

Supplemental Table D.4: Significant gene expression of hBMSC after 7 days on each foam grouped by material composition and listed by increasing PEO percentage. Fold change was calculated as a change from undifferentiated cells. P-values were computed for each gene between undifferentiated cells and those cultured on each specific foam composition from triplicate cultures.

Sample	Gene	log_2(Fold Change)	-log(P-value)
PAA100	ITGA3	-1.8782755	1.28152363
PAA100	MYF6	-2.622009833	1.3782515
PAA100	MEOX2	-2.1733725	1.10555101
PAA100	MEF2A	-2.067336833	1.42837779
PAA100	DES	-1.912468167	1.22323988
PAA100	TTN	-1.486895833	1.65428956
PAA100	TWIST1	-1.678737167	1.19175522
PAA100	TWIST2	-2.3413065	1.08206933
PAA100	MGP	2.824218167	1.36568433
PAA100	COL3A1	1.723557833	1.04365725
PAA100	GATA2	-2.656742167	1.64024651
PEO25	MYF5	-6.807566167	1.01038991
PEO25	MEOX2	-2.382349833	1.42261431
PEO25	DES	-1.5937935	1.42013382
PEO25	TWIST1	-1.639119833	1.05189941
PEO25	BMP8B	-9.830029833	1.53682937
PEO25	MGP	2.8683265	1.28240277
PEO25	COL3A1	1.7907835	1.03998676
PEO25	FABP4	-2.487109167	1.03041582
PEO25	GATA2	-2.3739245	1.25487559
PEO50	ITGA3	-1.455893333	1.25212155
PEO50	MYOG	-4.817258333	1.01164546
PEO50	MYF5	-3.517019667	1.62493461
PEO50	MEOX2	-1.791253333	1.27959524
PEO50	MSTN	1.990610333	1.11704672
PEO50	GRB2	-1.264123333	1.27068253
PEO50	BMP3	3.606054	1.11160877
PEO50	BMP5	4.230227333	1.07848468
PEO50	MGP	2.852793667	1.48996365
PEO75	MYOG	-9.796525833	1.04945058
PEO75	MYF5	-3.7029675	1.60126971
PEO75	MYF6	-3.804186833	1.06770941
PEO75	MEOX2	-2.344723833	1.34037885
PEO75	GRB2	-1.350811833	1.03781409
PEO75	SMAD5	-1.309450833	1.68375879
PEO75	BMP3	3.590568167	1.14222932
PEO75	MGP	2.564668833	1.22201433

Supplemental Table D.4: Significant gene expression of hBMSC after 7 days on each foam grouped by material composition and listed by increasing PEO percentage. Fold change was calculated as a change from undifferentiated cells. P-values were computed for each gene between undifferentiated cells and those cultured on each specific foam composition from triplicate cultures. (continue)

Sample	Gene	$\log_2$(Fold Change)	-log(P-value)
PEO100	MYF5	-3.9022395	1.46596046
PEO100	MYOT	7.572483833	1.25627864
PEO100	SMAD6	-1.008235167	1.06982602
PEO100	BMP3	3.0049385	1.25047212
PEO100	BMP8B	-6.875942167	1.01459005

Supplemental Table D.5: Non-significant gene expression of hES-MP after 7 days on each foam grouped by material composition and listed by increasing PEO percentage. Fold change was calculated as a change from undifferentiated cells. P-values were computed for each gene between undifferentiated cells and those cultured on each specific foam composition from triplicate cultures.

Sample	Gene	log_2(Fold Change)	-log(P-value)
PAA100	CD4	0.833891	0.56019
PAA100	ITGA1	-0.18697	0.596999
PAA100	CD9	0.686614	0.977806
PAA100	ITGA4	-0.74294	1.501993
PAA100	IL2R	11.65834	0.72076
PAA100	CD34	0.952242	0.54375
PAA100	PTPRC	-0.09922	0.324934
PAA100	ENG	1.149467	0.99152
PAA100	THY1	0.635098	1.092978
PAA100	PAX3	2.78054	0.702173
PAA100	PAX7	1.654872	0.359519
PAA100	MYOD1	0.298948	0.384326
PAA100	MYOG	3.91242	0.600968
PAA100	MYF5	1.483662	0.347402
PAA100	MYF6	5.620987	0.699576
PAA100	MEOX2	10.9817	0.689841
PAA100	FOXK1	1.036883	0.854469
PAA100	MSTN	3.562145	0.822947
PAA100	GRB2	1.284202	0.794028
PAA100	DES	-1.62812	0.765722
PAA100	MSX2	0.93713	0.848409
PAA100	LBX1	-2.31762	0.715958
PAA100	NRAP	0.298948	0.384326
PAA100	MYOT	-8.43879	0.588055
PAA100	TTN	1.402737	0.646946
PAA100	CDH15	0.298948	0.384326
PAA100	ITGB1	0.069572	0.511293
PAA100	ITGA7	-1.65607	0.98175
PAA100	CBFA1	0.965867	0.780886
PAA100	CDH11	-0.24644	1.297909
PAA100	TFIP11	0.751975	0.834324
PAA100	TWIST1	0.234266	0.724392
PAA100	TWIST2	0.721357	0.650768
PAA100	SMAD1	0.155667	0.442296
PAA100	SMAD2	0.445436	1.595488

Supplemental Table D.5: Non-significant gene expression of hES-MP after 7 days on each foam grouped by material composition and listed by increasing PEO percentage. Fold change was calculated as a change from undifferentiated cells. P-values were computed for each gene between undifferentiated cells and those cultured on each specific foam composition from triplicate cultures. (continue)

Sample	Gene	log_2(Fold Change)	-log(P-value)
PAA100	SMAD3	0.764377	1.069225
PAA100	SMAD4	-0.0424	0.385304
PAA100	SMAD5	0.683526	0.973287
PAA100	SMAD7	0.078205	0.428199
PAA100	SMAD9	0.300673	0.415934
PAA100	VDR	0.574133	0.597551
PAA100	BMP1	0.138458	0.498476
PAA100	BMP4	-0.48264	0.377449
PAA100	BMP5	-2.62943	0.542815
PAA100	BMP7	-6.46586	0.84251
PAA100	BMPR1A	0.656216	0.837909
PAA100	MGP	0.843895	0.474238
PAA100	COL1A1	-0.4184	0.832867
PAA100	COL1A2	0.222525	0.576828
PAA100	COL3A1	-0.85869	1.202895
PAA100	DLK1	-2.42517	0.660644
PAA100	PPARG	0.181024	0.307808
PAA100	CEBPA	2.677248	0.862746
PAA100	CEBPB	0.421634	0.817176
PAA100	KLF15	0.10195	0.333013
PAA100	SREBF1	1.389521	0.945024
PAA100	GPD1	0.227317	0.642828
PAA100	LPL	0.493999	0.327143
PAA100	NR1H3	0.073988	0.363055
PAA100	LEP	5.162063	0.68351
PAA100	ADIPOQ	-0.2521	0.348218
PAA100	LIPE	-2.68525	0.54472
PAA100	GATA2	0.605632	0.494272
PEO25	CD4	0.871861	1.043839
PEO25	ITGA1	0.689366	1.338536
PEO25	CD9	0.516272	1.311751
PEO25	ITGA2	1.009742	0.832361
PEO25	ITGA4	-0.35844	1.127891
PEO25	IL2R	-0.84001	0.731369

Supplemental Table D.5: Non-significant gene expression of hES-MP after 7 days on each foam grouped by material composition and listed by increasing PEO percentage. Fold change was calculated as a change from undifferentiated cells. P-values were computed for each gene between undifferentiated cells and those cultured on each specific foam composition from triplicate cultures. (continue)

Sample	Gene	log_2(Fold Change)	-log(P-value)
PEO25	CD34	0.898934	0.579892
PEO25	ENG	0.625478	1.328467
PEO25	THY1	0.423678	1.561236
PEO25	PAX3	0.983098	0.378375
PEO25	PAX7	3.669572	0.458926
PEO25	MYOD1	-0.84001	0.731369
PEO25	MYOG	2.824708	0.679217
PEO25	MYF6	-0.84001	0.731369
PEO25	MEOX2	-0.84001	0.731369
PEO25	FOXK1	0.533281	1.085383
PEO25	MEF2B	0.829969	1.824522
PEO25	MEF2C	0.842315	1.850764
PEO25	MEF2D	0.937969	1.09062
PEO25	GRB2	1.00447	0.85786
PEO25	DES	-0.42643	0.553649
PEO25	MSX1	0.941516	1.23078
PEO25	MSX2	-0.1385	0.467251
PEO25	LBX1	0.291362	0.595063
PEO25	NRAP	-0.84001	0.731369
PEO25	MYOT	-6.86087	0.507383
PEO25	TTN	-0.84001	0.731369
PEO25	CDH15	9.540572	0.740189
PEO25	ITGB1	0.222432	0.756293
PEO25	ITGA7	-0.12575	0.372448
PEO25	CBFA1	0.457558	2.985653
PEO25	CDH11	0.248083	1.815997
PEO25	TFIP11	0.443461	0.996556
PEO25	TWIST1	0.740772	1.19407
PEO25	TWIST2	0.824672	0.83698
PEO25	SMAD1	0.085283	0.981506
PEO25	SMAD2	0.270203	1.59053
PEO25	SMAD3	0.744128	1.286194
PEO25	SMAD4	0.116345	0.679931
PEO25	SMAD5	0.227967	0.884665

Supplemental Table D.5: Non-significant gene expression of hES-MP after 7 days on each foam grouped by material composition and listed by increasing PEO percentage. Fold change was calculated as a change from undifferentiated cells. P-values were computed for each gene between undifferentiated cells and those cultured on each specific foam composition from triplicate cultures. (continue)

Sample	Gene	log_2(Fold Change)	-log(P-value)
PEO25	SMAD6	0.949842	1.91889
PEO25	SMAD7	-0.12491	0.689743
PEO25	SMAD9	0.072878	0.833049
PEO25	VDR	0.292137	0.577797
PEO25	BGLAP	0.393117	0.771672
PEO25	BMP1	0.339318	1.795353
PEO25	BMP3	-6.16644	0.53803
PEO25	BMP4	-2.5328	0.860695
PEO25	BMP5	6.525733	0.613505
PEO25	BMP7	-0.7133	0.343275
PEO25	BMP8B	-10.8985	0.889646
PEO25	BMPR1A	0.430449	1.767304
PEO25	MGP	1.142971	0.468695
PEO25	COL1A1	0.046753	0.467261
PEO25	COL1A2	0.393743	1.037264
PEO25	COL3A1	-0.50082	0.919565
PEO25	DLK1	-0.76796	0.576987
PEO25	CEBPA	1.183068	0.855128
PEO25	CEBPB	0.206839	1.140496
PEO25	FABP4	1.023433	0.783693
PEO25	GPD1	-0.1343	0.520459
PEO25	LPL	6.277777	0.805977
PEO25	NR1H3	-0.19987	0.748088
PEO25	LIPE	-3.8242	0.689036
PEO25	GATA2	0.590451	0.805216
PEO50	CD4	1.288065	0.789179
PEO50	ITGA1	-0.15684	0.389531
PEO50	ITGA4	-0.60694	1.949835
PEO50	IL2R	0.02299	0.315465
PEO50	CD34	0.323038	0.383781
PEO50	PTPRC	-1.72363	0.814043
PEO50	18s		
PEO50	PAX3	5.631713	0.95397
PEO50	PAX7	2.817901	0.396401

Supplemental Table D.5: Non-significant gene expression of hES-MP after 7 days on each foam grouped by material composition and listed by increasing PEO percentage. Fold change was calculated as a change from undifferentiated cells. P-values were computed for each gene between undifferentiated cells and those cultured on each specific foam composition from triplicate cultures. (continue)

Sample	Gene	log_2(Fold Change)	-log(P-value)
PEO50	MYOD1	0.02299	0.315465
PEO50	MYOG	-3.69376	0.655011
PEO50	MYF5	7.241888	0.786365
PEO50	MEOX2	0.02299	0.315465
PEO50	FOXK1	0.743707	0.955182
PEO50	MSTN	6.52493	0.69753
PEO50	MEF2A	0.954687	1.010857
PEO50	MEF2B	0.684146	1.105588
PEO50	MSX2	0.786418	0.957328
PEO50	LBX1	0.072645	0.36207
PEO50	NRAP	0.02299	0.315465
PEO50	MYOT	-8.09781	0.591494
PEO50	CDH15	0.02299	0.315465
PEO50	ITGB1	0.314917	0.93693
PEO50	ITGA7	0.45989	0.610072
PEO50	CBFA1	0.29063	0.579836
PEO50	CDH11	-0.10014	1.3717
PEO50	TWIST1	0.979656	2.348017
PEO50	SMAD1	-0.1777	1.841045
PEO50	SMAD2	0.513051	1.223528
PEO50	SMAD3	0.694163	1.455309
PEO50	SMAD4	-0.00271	0.307004
PEO50	SMAD5	0.627987	1.081983
PEO50	SMAD7	0.337799	0.661724
PEO50	SMAD9	0.121894	0.367507
PEO50	VDR	-0.04795	0.328327
PEO50	BMP1	-0.05183	0.342686
PEO50	BMP3	-6.31602	0.558212
PEO50	BMP4	-1.12888	0.50489
PEO50	BMP5	2.185741	0.353361
PEO50	BMP7	3.64567	0.685545
PEO50	BMPR1A	0.642963	1.226201
PEO50	MGP	4.963249	0.953509
PEO50	COL1A1	-0.64372	1.254904

Supplemental Table D.5: Non-significant gene expression of hES-MP after 7 days on each foam grouped by material composition and listed by increasing PEO percentage. Fold change was calculated as a change from undifferentiated cells. P-values were computed for each gene between undifferentiated cells and those cultured on each specific foam composition from triplicate cultures. (continue)

Sample	Gene	log_2(Fold Change)	-log(P-value)
PEO50	COL1A2	-0.45877	0.903999
PEO50	DLK1	0.305733	0.470358
PEO50	PPARG	-5.13058	0.887252
PEO50	CEBPB	0.697707	0.802679
PEO50	KLF15	2.97898	0.976182
PEO50	FABP4	0.732056	0.571476
PEO50	GPD1	0.324758	0.717779
PEO50	LPL	2.977596	0.702883
PEO50	NR1H3	0.285751	0.625068
PEO50	ADIPOQ	-1.24541	0.427525
PEO50	LIPE	-2.96121	0.649556
PEO75	CD44	2.001224	0.957376
PEO75	ITGA1	0.84502	0.764125
PEO75	CD9	1.684523	0.867042
PEO75	ITGA2	2.602612	0.73057
PEO75	ITGA3	0.900416	1.259719
PEO75	ITGA4	-0.37502	1.317978
PEO75	IL2R	2.089822	0.679279
PEO75	CD34	1.352201	0.73083
PEO75	PTPRC	1.689225	0.46231
PEO75	ENG	1.405897	0.922458
PEO75	THY1	0.568154	1.701189
PEO75	PAX7	1.687007	0.353166
PEO75	MYOD1	2.089822	0.679279
PEO75	MYOG	4.779949	0.665716
PEO75	MYF5	-3.00146	0.669988
PEO75	MYF6	2.089822	0.679279
PEO75	MEOX2	2.089822	0.679279
PEO75	FOXK1	0.142743	0.365708
PEO75	MSTN	5.731352	0.93811
PEO75	MEF2A	1.829737	0.64341
PEO75	MEF2B	0.144381	0.445515
PEO75	MEF2C	1.414376	0.695133
PEO75	MEF2D	2.122654	0.710029

Supplemental Table D.5: Non-significant gene expression of hES-MP after 7 days on each foam grouped by material composition and listed by increasing PEO percentage. Fold change was calculated as a change from undifferentiated cells. P-values were computed for each gene between undifferentiated cells and those cultured on each specific foam composition from triplicate cultures. (continue)

Sample	Gene	log_2(Fold Change)	-log(P-value)
PEO75	DES	-0.62614	1.251718
PEO75	MSX1	0.952505	0.759535
PEO75	MSX2	1.107536	0.525976
PEO75	LBX1	0.709087	1.429359
PEO75	NRAP	2.089822	0.679279
PEO75	MYOT	-4.494	0.478461
PEO75	TTN	2.089822	0.679279
PEO75	CDH15	6.980902	0.676707
PEO75	ITGB1	0.847759	0.961006
PEO75	ITGA7	0.232152	0.439416
PEO75	CBFA1	1.116269	0.702249
PEO75	CDH11	0.391462	0.808456
PEO75	SPP1	3.239134	0.816574
PEO75	TFIP11	2.062508	0.781522
PEO75	TWIST1	0.994984	1.148876
PEO75	SOX9	0.796241	1.633957
PEO75	SMAD1	0.631538	0.959076
PEO75	SMAD2	1.364225	0.75577
PEO75	SMAD3	0.989969	0.747221
PEO75	SMAD4	0.701569	0.824521
PEO75	SMAD5	1.051782	0.838272
PEO75	SMAD6	0.319158	0.471825
PEO75	SMAD7	-0.781	0.554698
PEO75	SMAD9	-0.29953	0.456347
PEO75	VDR	-0.245	0.410207
PEO75	BGLAP	1.123254	0.660117
PEO75	BMP1	-0.2465	0.417375
PEO75	BMP2	1.838459	0.817535
PEO75	BMP3	-5.01265	0.495574
PEO75	BMP4	1.209286	0.469539
PEO75	BMP5	4.572305	0.438353
PEO75	BMP7	0.802279	0.383863
PEO75	BMPR1A	1.840109	0.744446
PEO75	MGP	1.221681	0.390048

Supplemental Table D.5: Non-significant gene expression of hES-MP after 7 days on each foam grouped by material composition and listed by increasing PEO percentage. Fold change was calculated as a change from undifferentiated cells. P-values were computed for each gene between undifferentiated cells and those cultured on each specific foam composition from triplicate cultures. (continue)

Sample	Gene	log_2(Fold Change)	-log(P-value)
PEO75	COL1A1	-0.26598	0.459374
PEO75	COL1A2	0.05346	0.32583
PEO75	COL3A1	-0.58057	0.588652
PEO75	DLK1	-0.63429	0.414138
PEO75	PPARG	1.902169	0.431454
PEO75	CEBPA	3.260406	0.827986
PEO75	CEBPB	0.930149	0.673349
PEO75	FABP4	0.424745	0.453197
PEO75	SREBF1	2.166658	0.87794
PEO75	GPD1	1.07094	0.833764
PEO75	LPL	-3.37568	0.979455
PEO75	NR1H3	1.287173	0.640781
PEO75	LEP	3.978195	0.983742
PEO75	ADIPOQ	6.730573	0.732371
PEO75	LIPE	-0.89437	0.652451
PEO100	CD4	1.370116	0.756285
PEO100	ITGA1	-0.34598	0.55906
PEO100	ITGA3	0.998752	2.394753
PEO100	IL2R	1.210702	0.981945
PEO100	PTPRC	-0.53591	0.405808
PEO100	PAX3	6.127621	0.962124
PEO100	PAX7	-1.07343	0.345964
PEO100	MYOD1	4.07241	0.977558
PEO100	MYOG	0.802932	0.344737
PEO100	MYF5	3.806667	0.441186
PEO100	MYF6	5.932363	0.756505
PEO100	MEOX2	3.978212	0.757598
PEO100	FOXK1	0.429692	1.680422
PEO100	MEF2A	-0.45182	0.485854
PEO100	MEF2B	0.352557	0.525981
PEO100	MEF2D	0.744234	0.740492
PEO100	DES	-0.07962	0.342829
PEO100	MSX1	0.806522	1.114461
PEO100	MSX2	0.238	0.43344

Supplemental Table D.5: Non-significant gene expression of hES-MP after 7 days on each foam grouped by material composition and listed by increasing PEO percentage. Fold change was calculated as a change from undifferentiated cells. P-values were computed for each gene between undifferentiated cells and those cultured on each specific foam composition from triplicate cultures. (continue)

Sample	Gene	log_2(Fold Change)	-log(P-value)
PEO100	LBX1	0.522552	1.622484
PEO100	NRAP	1.210702	0.981945
PEO100	MYOT	-8.27747	0.732846
PEO100	TTN	1.210702	0.981945
PEO100	CDH15	1.210702	0.981945
PEO100	ITGB1	0.088255	0.49215
PEO100	CBFA1	-0.04613	0.462086
PEO100	CDH11	-0.19213	1.655917
PEO100	TFIP11	0.771565	1.790276
PEO100	TWIST1	0.510055	1.511759
PEO100	SMAD1	0.144588	0.44844
PEO100	SMAD2	0.351553	1.008139
PEO100	SMAD3	-0.03329	0.480252
PEO100	SMAD4	-0.00774	0.325843
PEO100	SMAD5	0.204285	0.734232
PEO100	SMAD7	0.411051	1.909378
PEO100	SMAD9	-0.41438	0.797263
PEO100	VDR	-0.18337	0.380349
PEO100	BGLAP	1.291338	0.881465
PEO100	BMP1	0.194126	1.116722
PEO100	BMP2	-0.19121	0.325783
PEO100	BMP3	-2.03472	0.375724
PEO100	BMP5	7.703177	0.701647
PEO100	BMP7	3.043535	0.799823
PEO100	BMPR1A	0.597017	0.985523
PEO100	MGP	4.095873	0.786124
PEO100	COL1A1	-0.45081	0.979023
PEO100	COL1A2	-0.16931	0.553459
PEO100	COL3A1	-0.95812	1.04123
PEO100	PPARG	2.884077	0.536932
PEO100	CEBPA	1.109925	0.910057
PEO100	CEBPB	0.20261	0.503924
PEO100	KLF15	-0.18834	0.315086
PEO100	FABP4	0.572557	0.593758

Supplemental Table D.5: Non-significant gene expression of hES-MP after 7 days on each foam grouped by material composition and listed by increasing PEO percentage. Fold change was calculated as a change from undifferentiated cells. P-values were computed for each gene between undifferentiated cells and those cultured on each specific foam composition from triplicate cultures. (continue)

Sample	Gene	$\log_2$(Fold Change)	-log(P-value)
PEO100	GPD1	0.315069	0.602728
PEO100	LPL	-4.2548	0.858015
PEO100	NR1H3	0.126815	0.411545
PEO100	LEP	2.016579	0.428001
PEO100	ADIPOQ	3.49098	0.486457
PEO100	LIPE	-1.77349	0.555169

Supplemental Table D.6: Non-significant gene expression of hBMSC after 7 days on each foam grouped by material composition and listed by increasing PEO percentage. Fold change was calculated as a change from undifferentiated cells. P-values were computed for each gene between undifferentiated cells and those cultured on each specific foam composition from triplicate cultures.

Sample	Detector	$\log_2$(Fold Change)	-log(P-value)
PAA100	CD4	-0.3581	0.434854
PAA100	CD44	-1.69894	0.896238
PAA100	ITGA1	-0.12986	0.364551
PAA100	CD9	0.016082	0.305534
PAA100	ITGA2	-0.97742	0.66054
PAA100	ITGA4	-1.38923	0.827747
PAA100	IL2R	-0.27575	0.3379
PAA100	CD34	8.815919	0.587467
PAA100	PTPRC	1.06202	0.402688
PAA100	ENG	-0.84575	0.915465
PAA100	THY1	-0.24643	0.476972
PAA100	PAX3	-7.26863	0.866165
PAA100	PAX7	-6.55432	0.813287
PAA100	MYOD1	7.617104	0.814613
PAA100	MYOG	-1.91457	0.350651
PAA100	MYF5	-7.16159	0.947018
PAA100	FOXK1	-0.43145	0.896727
PAA100	MSTN	-1.90648	0.508657
PAA100	MEF2B	-1.06783	0.900139
PAA100	MEF2C	-0.83174	0.579322
PAA100	MEF2D	-1.52622	0.70396
PAA100	GRB2	-0.93835	0.67863
PAA100	MSX1	-1.8495	0.862997
PAA100	MSX2	-0.98131	0.595629
PAA100	LBX1	-1.02027	0.523139
PAA100	NRAP	-0.27575	0.3379
PAA100	MYOT	3.443817	0.607088
PAA100	CDH15	0.300888	0.484627
PAA100	ITGB1	-0.77739	1.117864
PAA100	ITGA7	-0.16424	0.952533
PAA100	CBFA1	-1.20235	0.826206
PAA100	CDH11	-0.07321	0.361407
PAA100	SPP1	0.113006	0.323863
PAA100	TFIP11	-1.29407	0.729522
PAA100	SOX9	-0.70455	0.522738
PAA100	SMAD1	-0.74971	0.548537
PAA100	SMAD2	-0.60235	0.868787
PAA100	SMAD3	-0.99928	1.264373
PAA100	SMAD4	-0.58042	0.800439
PAA100	SMAD5	-0.8708	0.99005
PAA100	SMAD6	-0.41518	0.435507

Supplemental Table D.6: Non-significant gene expression of hBMSC after 7 days on each foam grouped by material composition and listed by increasing PEO percentage. Fold change was calculated as a change from undifferentiated cells. P-values were computed for each gene between undifferentiated cells and those cultured on each specific foam composition from triplicate cultures. (continue)

Sample	Detector	$\log_2$(Fold Change)	-log(P-value)
PAA100	SMAD7	-0.89583	0.946736
PAA100	SMAD9	-1.30113	0.922897
PAA100	VDR	-1.05648	0.716146
PAA100	BGLAP	0.660511	0.578916
PAA100	BMP1	-0.37171	0.587421
PAA100	BMP2	0.874271	0.455381
PAA100	BMP3	-0.64296	0.396628
PAA100	BMP4	-0.63516	0.975014
PAA100	BMP5	-0.73024	0.382361
PAA100	BMP6	-2.09536	0.669748
PAA100	BMP7	-6.431	0.829476
PAA100	BMP8B	-5.28669	0.8475
PAA100	BMPR1A	-0.51247	0.615942
PAA100	COL1A1	-0.72291	0.537025
PAA100	COL1A2	0.389823	0.71504
PAA100	DLK1	3.396376	0.639155
PAA100	PPARG	1.345623	0.823285
PAA100	CEBPA	-1.53645	0.762699
PAA100	CEBPB	0.215316	0.37577
PAA100	KLF15	1.039377	0.580436
PAA100	FABP4	-1.32696	0.63456
PAA100	SREBF1	-0.47221	0.447144
PAA100	GPD1	0.222271	0.380349
PAA100	LPL	-4.02479	0.80999
PAA100	NR1H3	0.635253	0.603426
PAA100	LEP	2.432918	0.963672
PAA100	ADIPOQ	1.766442	0.671901
PAA100	LIPE	-0.27575	0.3379
PEO25	CD4	0.182879	0.372121
PEO25	CD44	-1.58436	0.921423
PEO25	ITGA1	-0.30247	0.942922
PEO25	CD9	-0.02829	0.311615
PEO25	ITGA2	-0.14779	0.332144
PEO25	ITGA3	-1.40407	0.936801
PEO25	ITGA4	-1.27486	0.8824
PEO25	IL2R	0.144836	0.31677
PEO25	CD34	-1.89793	0.786864
PEO25	PTPRC	0.779927	0.393199
PEO25	ENG	-0.49383	0.531909
PEO25	THY1	-0.37525	0.785778

Supplemental Table D.6: Non-significant gene expression of hBMSC after 7 days on each foam grouped by material composition and listed by increasing PEO percentage. Fold change was calculated as a change from undifferentiated cells. P-values were computed for each gene between undifferentiated cells and those cultured on each specific foam composition from triplicate cultures. (continue)

Sample	Detector	$\log_2$(Fold Change)	-log(P-value)
PEO25	PAX3	0.943432	0.355192
PEO25	PAX7	-5.22413	0.551628
PEO25	MYOD1	1.484291	0.452472
PEO25	MYOG	1.064908	0.332048
PEO25	MYF6	-4.48743	0.648176
PEO25	FOXK1	0.192885	0.423723
PEO25	MSTN	-1.58126	0.431132
PEO25	MEF2A	-1.7991	0.961744
PEO25	MEF2B	-0.1149	0.34701
PEO25	MEF2C	-0.34533	0.401706
PEO25	MEF2D	-1.09989	0.552946
PEO25	GRB2	-0.65278	0.526998
PEO25	MSX1	-1.06113	0.570027
PEO25	MSX2	-0.82331	0.532162
PEO25	LBX1	-1.27384	0.981633
PEO25	NRAP	1.832231	0.801327
PEO25	MYOT	2.889356	0.670147
PEO25	TTN	0.035057	0.317949
PEO25	CDH15	1.356411	0.829647
PEO25	ITGB1	-0.50795	0.744097
PEO25	ITGA7	-0.06341	0.580601
PEO25	CBFA1	-0.97769	0.703876
PEO25	CDH11	-0.1918	0.61128
PEO25	SPP1	0.61608	0.416976
PEO25	TFIP11	-0.57954	0.446348
PEO25	TWIST2	-1.33639	0.615239
PEO25	SOX9	-0.04775	0.311055
PEO25	SMAD1	-0.40756	0.430301
PEO25	SMAD2	-0.29284	0.601717
PEO25	SMAD3	-0.85093	1.276495
PEO25	SMAD4	-0.49812	0.7253
PEO25	SMAD5	-0.45137	0.525183
PEO25	SMAD6	-0.36143	0.420619
PEO25	SMAD7	-0.30587	0.460983
PEO25	SMAD9	-1.01052	0.69156
PEO25	VDR	0.512155	0.506261
PEO25	BGLAP	0.690119	0.631614
PEO25	BMP1	0.168888	0.410018
PEO25	BMP2	1.898101	0.577785
PEO25	BMP3	1.364455	0.587283

Supplemental Table D.6: Non-significant gene expression of hBMSC after 7 days on each foam grouped by material composition and listed by increasing PEO percentage. Fold change was calculated as a change from undifferentiated cells. P-values were computed for each gene between undifferentiated cells and those cultured on each specific foam composition from triplicate cultures. (continue)

Sample	Detector	$\log_2$(Fold Change)	-log(P-value)
PEO25	BMP4	-0.11391	0.352064
PEO25	BMP5	4.559972	0.803408
PEO25	BMP6	-0.82504	0.405257
PEO25	BMP7	-5.48386	0.689648
PEO25	BMPR1A	-0.38805	0.512511
PEO25	COL1A1	-0.71241	0.540997
PEO25	COL1A2	0.292021	0.61415
PEO25	DLK1	4.128946	0.724151
PEO25	PPARG	2.646429	0.689386
PEO25	CEBPA	-0.26313	0.380792
PEO25	CEBPB	0.199095	0.374537
PEO25	KLF15	0.28627	0.379976
PEO25	SREBF1	-0.28903	0.373961
PEO25	GPD1	-0.03719	0.319625
PEO25	LPL	-7.09314	0.800553
PEO25	NR1H3	0.460372	0.519414
PEO25	LEP	0.153723	0.346072
PEO25	ADIPOQ	-0.16453	0.318328
PEO25	LIPE	0.144836	0.31677
PEO50	CD4	1.075528	0.578159
PEO50	CD44	-1.30946	0.92889
PEO50	ITGA1	0.761468	0.627374
PEO50	CD9	1.035952	0.538441
PEO50	ITGA2	-0.79073	0.648237
PEO50	ITGA4	0.042655	0.308967
PEO50	IL2R	3.618489	0.522372
PEO50	CD34	5.179718	0.708903
PEO50	PTPRC	0.96667	0.400086
PEO50	ENG	-0.56146	0.836273
PEO50	THY1	0.186892	0.389474
PEO50	PAX3	3.697392	0.487671
PEO50	PAX7	-5.8827	0.499614
PEO50	MYOD1	3.618489	0.522372
PEO50	MYF6	0.756035	0.384704
PEO50	FOXK1	-0.7444	0.685985
PEO50	MEF2A	0.304348	0.360485
PEO50	MEF2B	1.321734	0.573156
PEO50	MEF2C	0.799489	0.483362
PEO50	MEF2D	-1.36074	0.789277
PEO50	DES	0.868937	0.457753

Supplemental Table D.6: Non-significant gene expression of hBMSC after 7 days on each foam grouped by material composition and listed by increasing PEO percentage. Fold change was calculated as a change from undifferentiated cells. P-values were computed for each gene between undifferentiated cells and those cultured on each specific foam composition from triplicate cultures. (continue)

Sample	Detector	log_2(Fold Change)	-log(P-value)
PEO50	MSX1	1.061701	0.447714
PEO50	MSX2	1.436416	0.507158
PEO50	LBX1	-2.7652	0.507237
PEO50	NRAP	5.363151	0.731415
PEO50	MYOT	6.718237	0.929901
PEO50	TTN	0.555714	0.505002
PEO50	CDH15	3.209232	0.765168
PEO50	ITGB1	-0.73643	0.751415
PEO50	ITGA7	-0.05761	0.51444
PEO50	CBFA1	-0.59695	0.594196
PEO50	CDH11	-0.78809	0.561626
PEO50	SPP1	1.096847	0.543163
PEO50	TFIP11	8.844891	0.614125
PEO50	TWIST1	-0.84953	0.861259
PEO50	TWIST2	0.091052	0.310872
PEO50	SOX9	1.519516	0.54122
PEO50	SMAD1	0.017103	0.306469
PEO50	SMAD2	-0.28729	0.750768
PEO50	SMAD3	-0.25278	0.440385
PEO50	SMAD4	-0.08326	0.390973
PEO50	SMAD5	0.064817	0.326875
PEO50	SMAD6	-0.48225	0.598781
PEO50	SMAD7	-0.81675	3.127843
PEO50	SMAD9	0.017376	0.305392
PEO50	VDR	1.148759	0.696863
PEO50	BGLAP	0.518204	0.640871
PEO50	BMP1	-0.01335	0.31
PEO50	BMP2	2.522018	0.645674
PEO50	BMP4	0.384829	0.41849
PEO50	BMP6	-0.4035	0.349123
PEO50	BMP7	-4.53602	0.593713
PEO50	BMP8B	-1.08634	0.351152
PEO50	BMPR1A	1.485803	0.597157
PEO50	COL1A1	-0.06815	0.320682
PEO50	COL1A2	0.13379	0.355431
PEO50	COL3A1	0.502788	0.405792
PEO50	DLK1	6.106872	0.862335
PEO50	PPARG	4.085669	0.579863
PEO50	CEBPA	1.854715	0.597236
PEO50	CEBPB	1.715176	0.6494

Supplemental Table D.6: Non-significant gene expression of hBMSC after 7 days on each foam grouped by material composition and listed by increasing PEO percentage. Fold change was calculated as a change from undifferentiated cells. P-values were computed for each gene between undifferentiated cells and those cultured on each specific foam composition from triplicate cultures. (continue)

Sample	Detector	$\log_2$(Fold Change)	-log(P-value)
PEO50	KLF15	3.686426	0.722412
PEO50	FABP4	0.428793	0.343241
PEO50	SREBF1	-0.0776	0.326732
PEO50	GPD1	2.439293	0.649849
PEO50	LPL	-2.52305	0.430934
PEO50	NR1H3	2.367289	0.760956
PEO50	LEP	4.686981	0.805092
PEO50	ADIPOQ	5.311997	0.625861
PEO50	LIPE	3.618489	0.522372
PEO50	GATA2	-0.19859	0.326617
PEO75	CD4	0.555306	0.427447
PEO75	CD44	0.051323	0.30815
PEO75	ITGA1	0.354624	0.467189
PEO75	CD9	0.627881	0.453898
PEO75	ITGA2	-0.74177	0.678869
PEO75	ITGA3	-0.25127	0.346522
PEO75	ITGA4	-0.08828	0.31905
PEO75	IL2R	3.446586	0.519092
PEO75	CD34	2.597715	0.623116
PEO75	PTPRC	1.225246	0.446859
PEO75	ENG	-0.81664	1.075533
PEO75	THY1	-1.26197	0.802119
PEO75	PAX3	-6.7455	0.692444
PEO75	PAX7	-1.80029	0.360232
PEO75	MYOD1	7.960193	0.592291
PEO75	FOXK1	-1.00525	0.742752
PEO75	MSTN	8.713626	0.777828
PEO75	MEF2A	-0.20354	0.340026
PEO75	MEF2B	0.976495	0.500041
PEO75	MEF2C	0.282248	0.35669
PEO75	MEF2D	0.004251	0.301631
PEO75	DES	0.210477	0.331459
PEO75	MSX1	0.425811	0.35606
PEO75	MSX2	1.124278	0.462414
PEO75	LBX1	-3.57012	0.582448
PEO75	NRAP	3.446586	0.519092
PEO75	MYOT	6.425289	0.904101
PEO75	TTN	0.396412	0.477785
PEO75	CDH15	3.359377	0.839503
PEO75	ITGB1	-0.59436	1.368843

Supplemental Table D.6: Non-significant gene expression of hBMSC after 7 days on each foam grouped by material composition and listed by increasing PEO percentage. Fold change was calculated as a change from undifferentiated cells. P-values were computed for each gene between undifferentiated cells and those cultured on each specific foam composition from triplicate cultures. (continue)

Sample	Detector	$\log_2$(Fold Change)	-log(P-value)
PEO75	ITGA7	-0.35267	1.879981
PEO75	CBFA1	-0.92875	0.722984
PEO75	CDH11	-1.10375	0.639569
PEO75	SPP1	0.698387	0.449558
PEO75	TFIP11	-1.70112	0.983943
PEO75	TWIST1	4.061803	0.554862
PEO75	TWIST2	-0.41669	0.346018
PEO75	SOX9	-0.34628	0.386218
PEO75	SMAD1	-0.34811	0.411573
PEO75	SMAD2	0.337346	0.41214
PEO75	SMAD3	-0.72234	0.892393
PEO75	SMAD4	-0.35294	0.78925
PEO75	SMAD6	-0.66578	0.684588
PEO75	SMAD7	-0.85441	1.272819
PEO75	SMAD9	-0.3197	0.39392
PEO75	VDR	1.08401	0.605997
PEO75	BGLAP	0.159073	0.385598
PEO75	BMP1	-0.28265	0.487948
PEO75	BMP2	2.658316	0.721618
PEO75	BMP4	0.094677	0.331864
PEO75	BMP5	3.9077	0.741407
PEO75	BMP6	-0.66992	0.383571
PEO75	BMP7	-1.129	0.961948
PEO75	BMP8B	2.934189	0.600871
PEO75	BMPR1A	0.779492	0.492098
PEO75	COL1A1	0.034804	0.310471
PEO75	COL1A2	0.323597	0.626884
PEO75	COL3A1	0.673538	0.471112
PEO75	DLK1	6.008695	0.843098
PEO75	PPARG	2.082167	0.417449
PEO75	CEBPA	2.356322	0.615017
PEO75	CEBPB	1.460748	0.585237
PEO75	KLF15	3.389157	0.69098
PEO75	FABP4	0.307353	0.333419
PEO75	SREBF1	0.484247	0.398592
PEO75	GPD1	-0.07722	0.379804
PEO75	LPL	-0.39607	0.349016
PEO75	NR1H3	2.258199	0.764069
PEO75	LEP	4.819954	0.866891
PEO75	ADIPOQ	3.142369	0.769298

Supplemental Table D.6: Non-significant gene expression of hBMSC after 7 days on each foam grouped by material composition and listed by increasing PEO percentage. Fold change was calculated as a change from undifferentiated cells. P-values were computed for each gene between undifferentiated cells and those cultured on each specific foam composition from triplicate cultures. (continue)

Sample	Detector	log_2(Fold Change)	-log(P-value)
PEO75	LIPE	3.446586	0.519092
PEO75	GATA2	-0.37796	0.352762
PEO100	CD4	1.419881	0.57557
PEO100	CD44	-0.95124	0.660831
PEO100	ITGA1	1.081878	0.591413
PEO100	CD9	0.609183	0.494868
PEO100	ITGA2	-0.0253	0.305732
PEO100	ITGA3	-1.16099	0.724939
PEO100	ITGA4	-0.41217	0.422983
PEO100	IL2R	3.098924	0.507898
PEO100	CD34	2.564563	0.675131
PEO100	PTPRC	-1.26658	0.41639
PEO100	ENG	-0.26133	0.457152
PEO100	THY1	0.48163	0.479895
PEO100	PAX3	-2.38201	0.54426
PEO100	PAX7	2.262515	0.43316
PEO100	MYOD1	12.31357	0.618982
PEO100	MYOG	-4.25505	0.892465
PEO100	MYF6	2.140323	0.507812
PEO100	MEOX2	-1.56271	0.799485
PEO100	FOXK1	-0.20975	0.703064
PEO100	MSTN	0.995899	0.618666
PEO100	MEF2A	-0.53041	0.446771
PEO100	MEF2B	0.553852	0.441996
PEO100	MEF2C	0.194034	0.356281
PEO100	MEF2D	-1.68927	0.869883
PEO100	GRB2	-0.83579	0.663897
PEO100	DES	0.039018	0.30852
PEO100	MSX1	0.183023	0.328544
PEO100	MSX2	0.978967	0.470079
PEO100	LBX1	0.062493	0.312035
PEO100	NRAP	3.098924	0.507898
PEO100	TTN	-0.16059	0.40434
PEO100	CDH15	2.716261	0.805774
PEO100	ITGB1	-0.77324	1.459313
PEO100	ITGA7	0.557487	0.498073
PEO100	CBFA1	0.247459	0.359988
PEO100	CDH11	0.002212	0.302737
PEO100	SPP1	1.29308	0.504525
PEO100	TFIP11	-1.26342	0.881116

Supplemental Table D.6: Non-significant gene expression of hBMSC after 7 days on each foam grouped by material composition and listed by increasing PEO percentage. Fold change was calculated as a change from undifferentiated cells. P-values were computed for each gene between undifferentiated cells and those cultured on each specific foam composition from triplicate cultures. (continue)

Sample	Detector	$\log_2$(Fold Change)	-log(P-value)
PEO100	TWIST1	-0.3916	0.565459
PEO100	TWIST2	-0.56599	0.378142
PEO100	SOX9	-0.29204	0.41158
PEO100	SMAD1	0.825451	0.468021
PEO100	SMAD2	-0.91646	1.102326
PEO100	SMAD3	-0.90156	1.829805
PEO100	SMAD4	-0.78379	1.292797
PEO100	SMAD5	-0.03714	0.315514
PEO100	SMAD7	-1.16594	0.974439
PEO100	SMAD9	-0.58497	0.574248
PEO100	VDR	0.33256	0.464633
PEO100	BGLAP	1.316141	0.796656
PEO100	BMP1	-0.62788	0.601983
PEO100	BMP2	2.132833	0.676455
PEO100	BMP4	-0.10948	0.367188
PEO100	BMP5	4.714086	0.822642
PEO100	BMP6	-0.91043	0.436476
PEO100	BMP7	-0.51451	0.398712
PEO100	BMPR1A	1.288053	0.549885
PEO100	MGP	2.17399	0.954101
PEO100	COL1A1	0.412804	0.406052
PEO100	COL1A2	0.089227	0.338564
PEO100	COL3A1	1.467463	0.94307
PEO100	DLK1	6.154662	0.93587
PEO100	PPARG	4.433485	0.678982
PEO100	CEBPA	2.519658	0.639986
PEO100	CEBPB	2.240238	0.68126
PEO100	KLF15	3.158473	0.73891
PEO100	FABP4	-0.50909	0.359451
PEO100	SREBF1	-0.80242	0.594264
PEO100	GPD1	1.703643	0.669783
PEO100	LPL	-4.01667	0.551161
PEO100	NR1H3	1.728805	0.725767
PEO100	LEP	3.910892	0.778022
PEO100	ADIPOQ	5.187592	0.878596
PEO100	LIPE	3.098924	0.507898
PEO100	GATA2	-0.73417	0.431768